UNIVERSIDAD TÉCNICA FEDERICO SANTA MARÍA

DEPARTAMENTO DE INGENIERIA CIVIL MÉCANICA

VALPARAISO – CHILE



“Estimación de la eficiencia de deposición en depósitos bimetálicos con Cold Spray”

JAVIER IGNACIO ABATE ZEPEDA

MEMORIA DE TITULACIÓN PARA OPTAR AL TÍTULO DE INGENIERO CIVIL MECÁNICO.

PROFESOR GUÍA : MARTIN CISTERNAS FERNANDEZ

PROFESOR CORREFERENTE : KAREM EVA TELLO ARAYA D.

NOVIEMBRE – 2025

CONSTANCIA DE VALIDACIÓN Y CONFIDENCIALIDAD DE MONOGRAFÍA A REPOSITORIO ACADÉMICO

1.- IDENTIFICACIÓN DEL TRABAJO ACADÉMICO

Tipo de monografía (marcar una opción): x Memoria o trabajo de título ☐ Tesis de Postgrado

Título del trabajo: **Estimación de la eficiencia de deposición en depósitos bimetálicos con Cold Spray**

Nombre del candidato(a): **Javier Ignacio Abate Zepeda**

Carrera / Grado: **Ingeniería Civil Mecánica**

Campus: Casa Central **Departamento:** Ingeniería Mecánica

2.- VALIDACIÓN DEL PROFESOR GUÍA/DIRECTOR DE TESIS

Yo, Martín Matías Cisternas Fernández, en mi calidad de profesor(a) guía/director(a) del trabajo académico mencionado anteriormente **DEJO CONSTANCIA** que:

- He revisado esta versión del documento y corresponde a la versión final aprobada del trabajo.
- El trabajo cumple con los requisitos académicos y de formato establecidos por la institución.

3.- EVALUACIÓN DE CONFIDENCIALIDAD POR PROPIEDAD INDUSTRIAL (marcar una opción)

x El trabajo **NO contiene** información que amerite confidencialidad y puede ser publicado de inmediato en repositorio con acceso abierto.

☐ El trabajo **CONTIENE** información con potenciales implicancias de propiedad industrial o intelectual y requiere un periodo de confidencialidad (**embargo**) por **(marcar una opción)**:

☐ 6 meses ☐ 12 meses ☐ 2 años ☐ 3 años ☐ 5 años ☐ 10 años

Fundamentación de la necesidad de confidencialidad (obligatorio si se solicita embargo):

4.- FIRMAS

Profesor(a) guía o director(a) de memoria o tesis:

Fecha: 04 de Diciembre de 2025 **Firma:** 

Estudiante o Candidato(a):

Fecha: 05 de Diciembre de 2025 **Firma:** 

Este formulario debe ser insertado como página 2 de la memoria o tesis, completado y firmado por estudiante y profesor(a) antes de la entrega en portal PRISMA de Biblioteca USM.



POLITECNICO
MILANO 1863

SCUOLA DI INGEGNERIA INDUSTRIALE
E DELL'INFORMAZIONE

Estimating deposition efficiency in cold spray bimetal deposits

Tesi di Laurea Magistrale in
Mechanical Engineering - Ingegneria Meccanica

Author: **Javier Ignacio Abate Zepeda**

Student ID: 219729
Advisor: Prof. Sara Bagherifard
Co-advisors: Kiran Tulasagiri Raddi, Asghar Heydari Astaraee
Academic Year: 2024-25

POLITECNICO
MILANO 1863

SCUOLA DI INGEGNERIA INDUSTRIALE
E DELL'INFORMAZIONE

Resumen Ejecutivo de Tesis

Estimating deposition efficiency in cold spray bimetal deposits

Trabajo de titulo para obtar a grado de Ingeniero Civil Mecánico

Autor: Javier Ignacio Abate Zepeda

Advisor: Prof. Sara Bagherifard

Co-advisor: Kiran Tulasagiri Raddi, Asghar Heydari Astaraee

Año Academico: 2025

1. Introducción

El objetivo de esta investigación es desarrollar un modelo predictivo para estimar la eficiencia de deposición (DE) y la composición de un depósito bimetálico producido mediante un proceso de "Coldspray" (CS).
Durante esta tesis se llevó a cabo una investigación sobre un depósito bimetálico, en la cual se utilizaron polvos de aluminio (Al) puro y hierro (Fe) puro como material de alimentación para obtener los depósitos.
El mecanismo de unión del proceso CS es complejo. Debido a esto, obtener la composición efectiva del recubrimiento, particularmente en recubrimientos bimetálicos, no es una tarea trivial, ya que la interacción entre diferentes polvos y sustratos incrementa la complejidad del modelado. Como resultado, a lo largo del tiempo, varios investigadores han realizado estudios dirigidos a desarrollar modelos predictivos que permitan comprender mejor el comportamiento de la formación del recubrimiento, prediciendo las DEs en el proceso y sus composiciones.
En esta tesis, se ha desarrollado un modelo en el cual un enfoque probabilístico, combinado con simulaciones numéricas de impacto, permite comprender las interacciones mencionadas y modelar la composición del recubrimiento.

2. Proceso de Cold spray

El proceso CS es un proceso de manufactura de deposición en estado sólido en el cual partículas de tamaño micrométrico, que pueden ser materiales metálicos o no metálicos, se depositan sobre un sustrato. Las partículas son aceleradas hasta velocidades supersónicas, logradas al impulsarlas con un gas a alta presión, como nitrógeno, helio o aire, con presiones de hasta 8.5 MPa y temperaturas que pueden alcanzar los 1000 ^{o}C. El principio de funcionamiento de este proceso de manufactura es particularmente ventajoso porque las partículas no alcanzan altas temperaturas, lo que permite no solo preservar sus propiedades térmicas, sino también utilizar una amplia gama de materiales [1].
En comparación con las tecnologías de proyección térmica, CS opera a temperaturas considerablemente más bajas, lo cual resulta beneficioso porque ayuda a evitar problemas como la formación de intermetálicos, el crecimiento de grano y la oxidación. Además, trabajar a temperaturas tan bajas previene la presencia de tensiones residuales, que en los procesos de proyección térmica surgen debido al rápido enfriamiento en la interfaz sustrato-recubrimiento. Otra ventaja de CS es que, dado que las partículas no se funden durante el proceso, estas impactan el sustrato

y generan un efecto de "peening", induciendo tensiones residuales compresivas. CS es particularmente útil para materiales sensibles al calor, en los que preservar la integridad del sustrato es fundamental [1].
La unión en CS se logra principalmente debido a dos tipos de enlaces: el enlace mecánico y el enlace metalúrgico. El tipo de unión predominante depende no solo de los materiales que interactúan, sino también de los parámetros de operación, que pueden eventualmente modificar la velocidad de impacto de las partículas y la temperatura. Además, los impactos a alta velocidad eliminan la capa de óxido superficial tanto de la partícula como del sustrato, permitiendo el contacto íntimo de átomos metálicos vírgenes. Asimismo, la generación de inestabilidad e corte adiabatico (ASI) desempeña un papel crucial en el mecanismo de unión, al generar deformaciones plásticas intensas en la interfaz que permiten la formación de enlaces metalúrgicos y mecánicos [1, 2].

3. Modelos predictivos de eficiencia de deposición

A lo largo del tiempo se han desarrollado diferentes modelos predictivos de DE, debido a que comprender la DE en un proceso CS es, especialmente para recubrimientos bimetálicos, de gran interés por su importancia en la optimización del proceso. Predecir adecuadamente la DE y, por lo tanto, la composición de los recubrimientos antes de la proyección permite contar con mayor información y, en consecuencia, reducir el desperdicio, determinar los materiales de alimentación y el espesor óptimos, asegurando recubrimientos de alta calidad con propiedades óptimas. Sin embargo, esta no es una tarea sencilla, ya que ocurren diversas interacciones. Las interacciones entre los polvos, así como la interacción entre el polvo y el sustrato, son relevantes al momento de comprender y modelar la DE y la composición de los recubrimientos.
Para los recubrimientos bimetálicos, es de suma importancia elegir adecuadamente los materiales que se van a proyectar, ya que el desempeño de este proceso estará condicionado por factores como la dureza, las propiedades térmicas y el tamaño de partícula, los cuales influyen en el comportamiento durante el proceso CS. De esta manera, la elección de materiales no solo afectará el resultado del recubrimiento en términos de las propiedades alcanzadas, sino también en la eficiencia con la que los materiales se depositan. A. Sova et al. [3] determinaron que una elección adecuada de los materiales y sus polvos de alimentación puede conducir a una mayor DE, incluso en comparación con la DE individual.
Entre los modelos predictivos desarrollados, los más recientes son el Semi-Empirical Probability Model (SEP) y el FEM-assisted DE predictive model. Estos dos modelos permiten obtener la DE y la composición de un recubrimiento bimetálico. El modelo SEP describe la importancia de la interacción entre polvos metálicos blandos y duros, y cómo la combinación de ambos mejora el desempeño del proceso CS. Este modelo aborda el desafío de obtener la DE y la composición del recubrimiento bimetálico incorporando interacciones basadas en probabilidad mediante pruebas experimentales, de donde surge el concepto de probabilidad de adhesión. Esta probabilidad contempla la interacción entre diferentes polvos [3].
El FEM-assisted DE predictive model, desarrollado por A. Ardeshiri Lordejani et al. [4], incluyó con el fin de refinar la predicción el efecto de la deformación de las partículas, las interacciones con el sustrato y un concepto de capa en evolución. La deformación de las partículas se evaluó introduciendo simulaciones de impacto de partículas por elementos finitos (FE), modelando la interacción de una partícula de un material dado al contactar con diferentes superficies. Además, la interacción polvo-sustrato fue incorporada en el modelo basado en probabilidad, lo que permitió comprender mejor el efecto del sustrato sobre el recubrimiento. Finalmente, el proceso iterativo aplicado para calcular la DE y la composición a lo largo del espesor permite comprender no solo el estado estacionario, sino también el transitorio.
Estos modelos, particularmente el enfoque asistido por FEM, representan avances significativos en la predicción de la DE y la composición de recubrimientos. Permiten una comprensión más profunda de la dinámica compleja de los recubrimientos multicomponente y posibilitan un mejor control sobre el proceso CS, mejorando el desempeño final del recubrimiento y reduciendo el desperdicio de material. Las mejoras desar-

rolladas para este modelo existente serán detalladas en la Subsección 4.1.

4. Pruebas experimentales y desarrollo del modelo

Durante esta investigación se desarrolló un modelo predictivo de DE. Para aplicar adecuadamente este modelo, se realizaron simulaciones por elementos finitos (FE) y se adquirieron algunos datos de manera experimental. Posteriormente, se llevaron a cabo pruebas experimentales para validar el modelo. En esta sección se explicará el modelo, junto con la configuración de las simulaciones FE y las pruebas experimentales.

4.1. Modelo predictivo de DE asistido por FEM mejorado

El modelo predictivo de DE asistido por FEM mejorado se desarrolló como una mejora del FEM-assisted DE predictive model desarrollado por A. Ardeshiri Lordejani et al. [4]. Este consiste en un proceso iterativo que calcula, capa por capa, la composición del recubrimiento y la DE. Esto se realiza considerando las probabilidades de adhesión entre los diferentes polvos y la interacción polvo-sustrato, las cuales se obtendrán experimentalmente mediante pruebas de probabilidad de adhesión. Además, este modelo utilizará simulaciones de impacto por elementos finitos (FE) para determinar cómo se deforman las partículas al impactar sobre diferentes superficies.

Como se muestra en la Figura 1, el modelo considerará iterativamente un tamaño de partícula diferente en cada iteración, seleccionándolos de acuerdo con la distribución de probabilidad de los polvos suministrados. Durante esta investigación se considerarán tres tamaños de partícula diferentes para cada polvo, aunque el modelo puede adaptarse a un mayor número de tamaños de partículas.

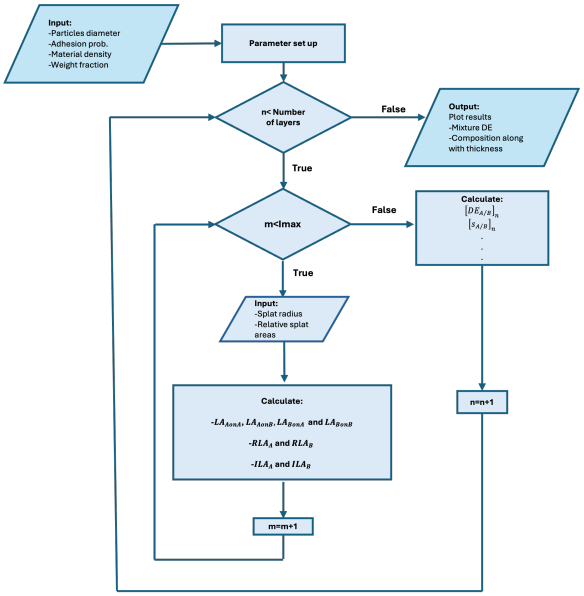


Figure 1: Diagrama de flujo usado para la predicción de la composición del revestimiento

Como entrada para el modelo, se requerirán las probabilidades de adhesión de los materiales. En el caso de un recubrimiento bimetálico como el estudiado aquí, se van a utilizar dos materiales, que se denotarán como A y B. Se requerirán las siguientes probabilidades de adhesión:

- p_{A-A}: probabilidad de adhesión de A sobre A (DE de A sobre A)
- p_{A-B}: probabilidad de adhesión de A sobre B (DE de A sobre B)
- p_{B-A}: probabilidad de adhesión de B sobre A (DE de B sobre A)
- p_{B-B}: probabilidad de adhesión de B sobre B (DE de B sobre B)
- p_{A-S}: probabilidad de adhesión de A sobre el sustrato (DE de A sobre sustrato)
- p_{B-S}: probabilidad de adhesión de B sobre el sustrato (DE de B sobre sustrato)

Luego, como se muestra en la Figura 1, los cálculos de cada capa tienen en cuenta el efecto de la capa anterior, requiriendo un proceso iterativo para determinar la composición de cada nueva capa. Durante cada iteración, se calculan tres parámetros relacionados con el área: el Área de Capa Ideal (ILA), que representa la cantidad teórica de polvo necesaria para una cobertura completa; el Área de Capa (LA), el área efectivamente cubierta, que depende de las probabilidades de adhesión; y el Área de Capa Restante (RLA), la porción no cubierta. Este proceso se repite hasta alcanzar la cobertura completa (es

decir, RLA = 0).
Para simplificar, la nomenclatura a seguir durante el proceso iterativo se definirá como $[(valor)_m]_n$, donde m es el número de iteración y n el número de capa.
La Ecuación (1) corresponde a la ecuación generalizada que permite obtener la RLA del material A para la iteración m en la capa 2. Esta ecuación considera el LA de la iteración anterior, *m-1*, tanto para el LA del material A depositado sobre A ($[(LA_{AonA})\, m-1]\, 2$) como para el material B depositado sobre A ($[(LA_{BonA})\, m-1]\, 2$), así como el área relativa del material A depositado en la capa 1 ($[s_A]_1$).

$$[(RLA_A)_m]_2 = [s_A]_1 - \left\{[(LA_{AonA})_{m-1}]_2 - [(LA_{BonA})_{m-1}]_2\right\} \quad (1)$$

La Ecuación (2) corresponde a la ecuación para el LA del material A sobre el material A en la iteración m de la segunda capa. Esta ecuación requiere la concentración numérica de partículas de polvo y la probabilidad de adhesión, que en este caso es la probabilidad de que el material A se adhiera sobre A. Además, se requiere la RLA del material A para todas las iteraciones anteriores, como se indica en la sumatoria. Finalmente, se necesita un parámetro llamado área relativa de splat, que para este caso corresponde al área relativa de splat de una partícula de material A sobre A ($SA_{A-A}(D_j)$). Este parámetro depende de los resultados de las simulaciones de impacto por FE y también es función del diámetro de la partícula.

$$[(LA_{AonA})_m]_2 = c_A p_{A-A} \left\{\sum_{i=1}^{m} [(RLA_A)_i]_2\right\} SA_{A-A}(D_j) \quad (2)$$

La Ecuación (3) define el Área de Capa Ideal (ILA) del material A sobre A para la iteración m en la segunda capa. Esta incorpora la concentración numérica de partículas de polvo, las áreas relativas de splat para las interacciones del material A tanto sobre A como sobre B, así como las áreas relativas de capa (RLA) de iteraciones anteriores. Las áreas de splat, que dependen del diámetro de la partícula, se derivan de las simulaciones de impacto por FE.

$$[(ILA_A)_m]_2 = c_A \left\{\sum_{i=1}^{m} [(RLA_A)_i]_2\, SA_{A-A}(D_j) + [(RLA_B)_i]_2\, SA_{A-B}(D_j)\right\} \quad (3)$$

4.2. Simulaciones de impacto con FE

Es necesario realizar simulaciones de impacto por FE, ya que el radio de splat es un requisito para el modelo desarrollado, permitiendo el cálculo de diferentes parámetros como LA, ILA y RLA, tal como se explicó en la subsección anterior. Para realizar las simulaciones se utilizó el método Euleriano-Lagrangiano Acoplado (CEL, Coupled Eulerian-Lagrangian). Este método fue preferido debido a su excelente desempeño en la modelación de deformaciones plásticas elevadas. Se utilizó un modelo 3D para todas las simulaciones de impacto, como se muestra en la Figura 2. Solo se modeló un cuarto de la partícula y del sustrato, aplicando las simetrías correspondientes. La partícula se modeló como un cuarto de esfera y el sustrato como un cuarto de cilindro. Para el método CEL, era necesario definir un componente vacío para establecer el dominio Euleriano en la simulación. En la mayoría de las simulaciones de impacto, la partícula formaba parte del dominio Euleriano y el sustrato del dominio Lagrangiano. Sin embargo, se hizo una excepción en los casos donde la partícula era mucho más dura que el sustrato, lo que resultaba en casi ninguna deformación. En estos casos, la partícula se asignó al dominio Lagrangiano y el sustrato al dominio Euleriano.

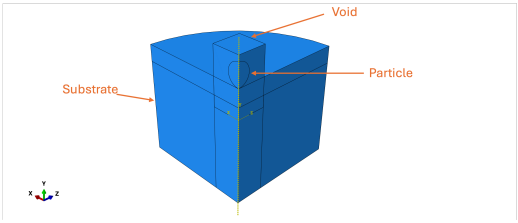


Figure 2: Assembly utilizado para el caso en el que la partícula experimenta deformaciones plásticas mayores.

4.3. Proceso de Cold spray

Las pruebas experimentales se realizaron en el Politecnico di Milano utilizando un robot ABB IRB4600 (40 kg) (Figura 3) y un sistema de Coldspray Impact Innovations ISS 5/11 (Impact Innovations Inc., Alemania) equipado con una boquilla SiC Out-1 convergente-divergente (relación de expansión: 5.6) (Figura 3).



Figure 3: Pistola de spray montada en el brazo robotico

4.3.1 Prueba de wipe

La prueba de wipe evalúa cualitativamente el comportamiento de las partículas al impactar sobre un sustrato. Para estas pruebas se utilizó nitrógeno como gas del proceso a 50 bar y 450 ºC, empleando como sustratos una aleación de aluminio (Al6032) y hierro puro. Después de la proyección, las muestras fueron seccionadas transversalmente, embebidas en resina conductiva y pulidas hasta 1 µm, seguidas de un tratamiento con solución UPS para obtener la mejor superficie posible para el análisis microscópico. El análisis se realizó utilizando un Microscopio Electrónico de Barrido Zeiss EVO 50 (Carl Zeiss Microscopy GmbH, Alemania).

4.3.2 Prueba de probabilidad de adhesión

Las pruebas de probabilidad de adhesión consistieron en proyectar dos materiales diferentes sobre diversas superficies de impacto, incluyendo sustratos y materiales previamente depositados. Estas pruebas tuvieron como objetivo calcular las eficiencias de deposición, proporcionando información sobre las interacciones entre materiales para su incorporación en el modelo predictivo de DE. Para aplicar el modelo a un sustrato determinado, se requieren seis probabilidades de adhesión. En este estudio, se realizaron ocho pruebas experimentales para tener en cuenta los dos sustratos diferentes analizados. La Figura 4 ilustra la disposición de estas pruebas, mostrando las ocho muestras examinadas.

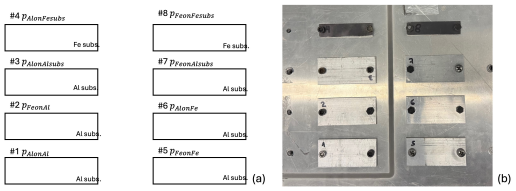


Figure 4: (a) Disposición de las pruebas experimentales y (b) muestras antes del proceso de proyección.

4.3.3 Depositos de capa delgada

En depósitos de capa delgada, la pistola de proyección genera recubrimientos de espesor considerable, lo que permite el análisis de la composición del recubrimiento y la determinación de la DE. Para estas pruebas se utilizó nitrógeno como gas del proceso a 50 bar y 450 ºC. Los sustratos fueron una aleación de aluminio (Al6032) y hierro puro. Se produjeron seis muestras utilizando tres polvos de alimentación diferentes, con dos sustratos por cada polvo. Después de las pruebas, las muestras fueron cortadas, embebidas en resina conductiva y pulidas hasta 1, μm, seguidas de un tratamiento con solución UPS para el análisis microscópico. El microscopio utilizado fue un Microscopio Electrónico de Barrido Zeiss EVO 50 (Carl Zeiss Microscopy GmbH, Alemania), y los resultados fueron procesados con el software ImageJ, versión 1.53A, como se muestra en la Figura 5.

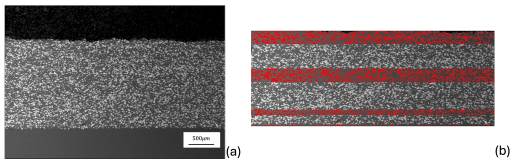


Figure 5: (a) Imagen obtenida con el microscopio SEM de un recubrimiento con un polvo de alimentación de 50% Al y 50% Fe sobre un sustrato de aluminio, y (b) análisis de composición realizado utilizando el software ImageJ.

5. Resultados y discusión

5.1. Prueba de wipe y simulaciones de impacto

Con respecto a las simulaciones de impacto de partículas, se realizaron dieciocho simulaciones. El objetivo de estas simulaciones fue obtener el radio de splat, necesario para calcular las áreas relativas de splat y, en consecuencia, los demás parámetros requeridos para determinar la composición y la DE del recubrimiento en cada capa. Las dieciocho simulaciones de impacto consideraron el impacto de partículas de aluminio e hierro de tres tamaños diferentes sobre dos sustratos distintos: la aleación de aluminio Al6082 y el sustrato de hierro puro. Estos resultados fueron posteriormente contrastados con las pruebas de wipe. Los resultados de las pruebas de wipe permiten comprender cómo se comportan las partículas de un material dado al impactar sobre superficies del mismo u otro material y, por lo tanto, compararlos cualitativamente con las simulaciones de impacto por FE.
En la Figura 6 se puede observar el contraste entre los resultados obtenidos experimentalmente a la derecha y las simulaciones de impacto por FE. Se puede apreciar que, en la interacción entre una partícula de aluminio y una superficie de aluminio, tanto la superficie como la partícula sufren deformaciones plásticas notables.

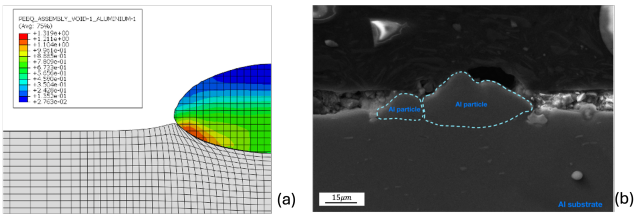


Figure 6: (a) Simulación de impacto por FE de polvo de Al sobre Al, y (b) partículas de aluminio depositadas sobre un sustrato de aluminio.

En la Figura 7 se puede observar una situación diferente. Aquí, el sustrato es mucho más duro en comparación con la partícula, lo que provoca una deformación plástica significativa en la partícula, mientras que el sustrato permanece prácticamente sin deformarse.

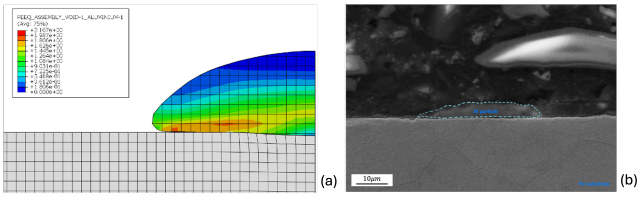


Figure 7: (a) Simulación de impacto por FE de Al sobre Fe, y (b) partículas de aluminio depositadas sobre un sustrato de hierro.

En la Figura 8 se puede observar un comportamiento completamente opuesto: aquí, la partícula de hierro es mucho más dura en comparación con el sustrato de aluminio y, por lo tanto, apenas se deforma, penetrando profundamente en el sustrato.

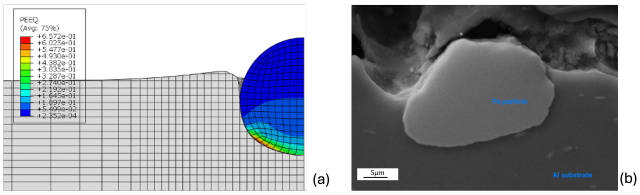


Figure 8: (a) Simulación de impacto por FE de Fe sobre Al, y (b) partículas de hierro depositadas sobre un sustrato de aluminio.

5.2. Análisis de la composición del recubrimiento

Los depósitos de capa delgada se realizaron para las combinaciones de polvos de alimentación y sustratos seleccionadas para esta investigación.
En la Figura 9 se muestra una comparación entre los datos experimentales y los resultados del modelo predictivo para un polvo de alimentación de 25% Al - 75% Fe. Los datos experimentales presentan una fase transitoria cerca del sustrato, donde la composición de aluminio alcanza un máximo de 69.35% antes de disminuir hasta un rango en estado estacionario de 57.23% a 49.89% a un espesor de 45, μm.
Para el modelo predictivo, el contenido inicial de aluminio es de 61.77%, disminuyendo hasta un rango en estado estacionario de 55.01% a 51.95% a un espesor de 38, μm.

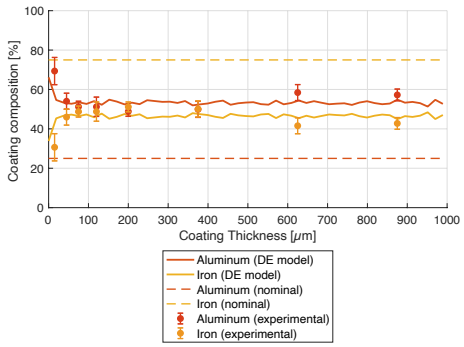


Figure 9: Comparación entre el modelo predictivo de DE y la composición determinada experimentalmente para un polvo de alimentación de 25% Al y 75% Fe sobre un sustrato de aleación de aluminio.

La Figura 10 compara los resultados experimentales y del modelo predictivo para un polvo de alimentación de 50% Al - 50% Fe sobre un sustrato de aluminio. En los datos experimentales, el contenido de aluminio comienza en 85.79% durante la fase transitoria y disminuye hasta un rango en estado estacionario de 73.84% a 74.89% a un espesor de 45, μm.
Para el modelo predictivo, la fase transitoria comienza en 86.17% y se estabiliza a 16.98, μm, con valores de aluminio que oscilan entre 80.25% y 77.50%.

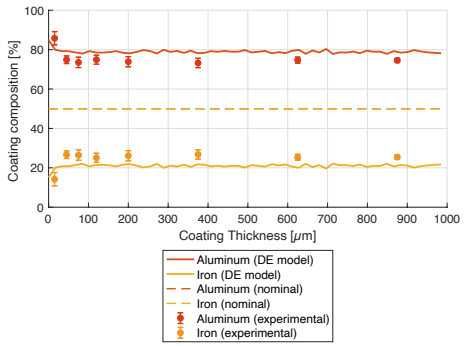


Figure 10: Comparación entre el modelo predictivo de DE y la composición determinada experimentalmente para un polvo de alimentación de 50% Al y 50% Fe sobre un sustrato de aleación de aluminio.

Para un polvo de alimentación de 50% Al–50% Fe sobre un sustrato de hierro, la Figura 11 muestra que el modelo predictivo sobreestima ligeramente el porcentaje de aluminio.

En los datos experimentales, el aluminio comienza en 67.65% y se estabiliza entre 68.18% y 69.81%, con una diferencia mínima entre la fase transitoria y el estado estacionario.
Para el modelo predictivo, la fase transitoria comienza en 73.05%, alcanzando el estado estacionario a 33 μm, con valores de aluminio que oscilan entre 81.19% y 77.65%.

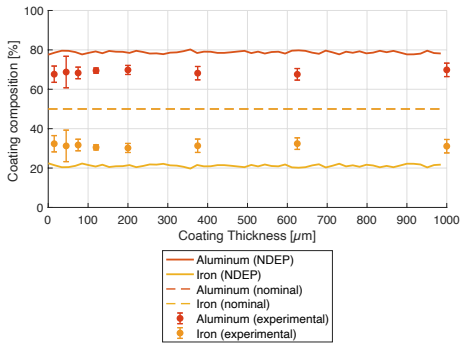


Figure 11: Comparación entre el modelo predictivo de DE y la composición determinada experimentalmente para un polvo de alimentación de 50% Al y 50% Fe sobre un sustrato de hierro puro.

6. Conclusiones

En este trabajo de tesis se desarrolló un modelo para predecir la composición de un recubrimiento bimetálico producido mediante un proceso CS. Los materiales utilizados para producir los recubrimientos fueron polvo de aluminio puro y polvo de hierro puro. Estos se depositaron utilizando tres polvos de alimentación diferentes: 25% Al–75% Fe, 50% Al–50% Fe y 75% Al–25% Fe, sobre dos tipos de sustratos distintos: un sustrato de aleación de aluminio (Al6082) y un sustrato de hierro puro ARMCO. El modelo predictivo desarrollado consideró los modelos predictivos existentes y los mejoró al incorporar la distribución de probabilidad del polvo bimetálico, simulando así un comportamiento más cercano al experimental. Este modelo utilizó tanto simulaciones numéricas como datos experimentales como entradas para predecir con precisión la composición para diferentes polvos de alimentación y materiales. Para la DE predicha, esta aumenta a medida que incrementa la fracción en peso de aluminio, alcanzando su valor máximo al 75% de aluminio.
Para los datos numéricos, se realizaron simu-

laciones de impacto utilizando el método CEL debido a su rendimiento en la modelación de grandes deformaciones plásticas. Los resultados obtenidos fueron corroborados con imágenes de pruebas de *wipe* experimentales. El modelo desarrollado predice con éxito la composición del recubrimiento y considera la interacción entre los polvos y el sustrato, permitiendo un análisis más completo del comportamiento tanto en la fase transitoria como en el estado estacionario. Sin embargo, las imprecisiones aumentaron a medida que crecía el porcentaje de polvo de aluminio, posiblemente debido a la suposición de una morfología de partícula esférica, lo que pudo haber afectado tanto los cálculos de probabilidad de adhesión como las simulaciones de impacto. A pesar de esto, el modelo demuestra un potencial significativo para la optimización de procesos de recubrimientos bimetálicos, con posibles mejoras al considerar propiedades adicionales de los materiales.

References

[1] Victor Kenneth Champagne, Ozan Cagatay Ozdemir, and Aaron Nardi, editors. *Practical Cold Spray*. Springer International Publishing, Cham, 2021. ISBN 978-3-030-70055-3 978-3-030-70056-0. doi: 10.1007/978-3-030-70056-0.

[2] S. M. Hassani-Gangaraj, A. Moridi, and M. Guagliano. Critical review of corrosion protection by cold spray coatings. 31(11): 803–815. ISSN 0267-0844, 1743-2944. doi: 10.1179/1743294415Y.0000000018.

[3] A. Sova, R. Maestracci, M. Jeandin, Ph. Bertrand, and I. Smurov. Kinetics of composite coating formation process in cold spray: Modelling and experimental validation. *Surface and Coatings Technology*, 318: 309–314, May 2017. ISSN 02578972. doi: 10.1016/j.surfcoat.2016.06.084.

[4] Amir Ardeshiri Lordejani, Luca Vitali, Mario Guagliano, and Sara Bagherifard. Estimating deposition efficiency and chemical composition variation along thickness for cold spraying of composite feedstocks. *Surface and Coatings Technology*, 436:128239, April 2022. ISSN 02578972. doi: 10.1016/j.surfcoat.2022.128239.

Abstract

The Cold Spray (CS) process is a promising solid-state deposition technology that enables the deposition of various materials, both metallic and non-metallic powders, without causing their melting because of its low working temperature. This characteristic makes CS particularly useful for applications where preserving the material's properties is critical. This research focuses on developing a predictive model for the deposition efficiency (DE) and composition of bimetallic coatings made from pure aluminum and pure iron powders. The model is built by integrating numerical simulations and experimental data, followed by experimental validation.

Over time, several researchers have proposed different DE predictive models for CS coatings. In this thesis, an enhanced DE predictive model has been developed, combining information obtained through Finite Element (FE) particle impact simulations and experimental tests, along with the powder probability distribution, which allows for a more accurate understanding of the coating formation. Different simulation methods were explored to develop a precise representation of particle-substrate interactions. Additionally, experimental tests were conducted, including adhesion probability tests to determine the DE of the materials studied and to understand how they interact with each other, wipe tests to qualitatively validate the impact simulations, and thin layer tests to assess the model's accuracy by measuring the coating's composition across the thickness and thus validating the predictive model. The results from these tests provide valuable insights into the relationship between process parameters and coating performance, allowing for improved prediction of DE and composition in bimetallic CS coatings.

This research aims to optimize CS parameters for bi-metallic deposits, enabling their use in various applications such as lightweight design, wear resistance enhancement, corrosion protection, and improved fatigue resistance through strategic material selection.

Keywords: Cold Spray, Deposition Efficiency, Bimetallic Coatings, FEM Simulation, Predictive Modeling

Abstract in lingua italiana

Il processo di Cold Spray (CS) è una tecnologia di rivestimento allo stato solido che consente la deposizione di materiali metallici e non metallici senza fusione, grazie alla sua bassa temperatura di lavorazione. Questa caratteristica lo rende particolarmente utile per applicazioni in cui è essenziale preservare le proprietà del materiale. Questa ricerca si concentra sullo sviluppo di un modello predittivo per l'efficienza di deposizione (DE) e la composizione dei rivestimenti bimetallici realizzati con polveri di alluminio e ferro puro. Il modello integra simulazioni numeriche e dati sperimentali, seguiti da una validazione sperimentale.

Nel tempo, diversi modelli predittivi di DE sono stati proposti per il Cold Spray. In questa tesi, è stato sviluppato un modello avanzato che combina simulazioni mediante Elementi Finiti (FE) di impatto di particelle e test sperimentali, includendo la distribuzione di probabilità delle polveri per una migliore comprensione della formazione del rivestimento. Sono stati condotti test di probabilità di adesione, wipe tests per validare qualitativamente le simulazioni e test su strati sottili per valutare l'accuratezza del modello, confrontando la composizione sperimentale con quella predetta. I risultati forniscono preziose informazioni sulla relazione tra i parametri di processo e le prestazioni del rivestimento.

Questa ricerca mira a ottimizzare i parametri del processo di Cold Spray (CS) per i rivestimenti bimetallici, consentendone l'uso in diverse applicazioni come il design leggero, il miglioramento della resistenza all'usura, la protezione dalla corrosione e il miglioramento della resistenza alla fatica attraverso una selezione strategica dei materiali.

Parole chiave: Cold Spray; Efficienza di Deposizione; Rivestimenti Bimetallici; Simulazione FEM; Modellazione Predittiva

Contents

Abstract **i**

Abstract in lingua italiana **iii**

Contents **v**

List of Figures **ix**

List of Tables **xiii**

Introduction **1**

1 Cold Spray **3**

1.1 Process description 3
1.2 Classification according to the powder feeding and acceleration mechanism 3
1.2.1 Classifying cold spray system according to the working pressure . . 4
1.2.2 Nozzle classification 5
1.3 Comparison between cold spray and thermal spray 6
1.3.1 Advantages and limitations 9
1.4 Bonding mechanism and deposition efficiency 11
1.4.1 Bonding mechanism 11
1.4.2 Deposition efficiency (DE) 12
1.5 Temperature and particle velocity 13
1.6 Cold spray feedstock powders 17
1.6.1 Powder size effect 17
1.6.2 Material effect 18
1.6.3 Morphology effect 19
1.7 Possible application 20
1.7.1 Cold spray coatings used to improve corrosion resistance 20
1.7.2 Fatigue resistance improvement through cold spray 21

1.7.3 Wear resistance enhancement 23

2 Modeling of Deposition efficiency 25

2.1 Different models that estimates the deposition efficiency in a cold spray mixture 25

2.1.1 Rule of mixture (ROM) 26

2.1.2 Bond ratio splat tests based model (BRST) 27

2.1.3 Semi-empirical probability model (SEP) 29

2.1.4 FEM assisted DE predictive model 33

2.2 Advantages and limitations of the models 37

3 Particle impact modeling simulation 39

3.1 Different methods for particle impact modeling 39

3.1.1 Lagrangian method 39

3.1.2 Arbitrary Lagrangian-Eulerian (ALE) method 40

3.1.3 Smoothed particle hydrodynamics (SPH) method 41

3.1.4 Coupled Eulerian-Lagrangian (CEL) method 42

3.2 Impact simulation set up 43

4 Experimental test and model development 51

4.1 Powder characterization 51

4.2 Cold spray process 52

4.2.1 Wipe test 52

4.2.2 Thin layer deposit 53

4.2.3 Adhesion probabilities test 54

4.3 Enhanced FEM assisted DE predictive model 57

5 Results and discussion 65

5.1 Impact simulation results 65

5.2 Wipe test impact particle results 68

5.3 Adhesion probabilities obtained experimentally 70

5.4 DE and composition along with thickness 72

6 Conclusions 83

6.1 FEM particle impact simulations 83

6.2 DE predictive model 84

6.3 Future developments 84

Bibliography **85**

A MATLAB Codes **91**
A.1 MATLAB Code for DE predictive model 91
A.2 MATLAB Code for calulating the adhesion probabilities 99

Acknowledgements **101**

Agradecimientos **103**

List of Figures

1.1 High pressure cold spray system [1]. 4
1.2 Low pressure cold spray system [1]. 5
1.3 Supersonic nozzle with upstream powder injection [2]. 5
1.4 supersonic nozzle with downstream powder injection [2]. 5
1.5 Gas pressure, temperature, velocity, and density as a function of distance in a sonic nozzle[2]. 6
1.6 Schematic of a sonic nozzle[2]. 6
1.7 Schematic diagram of a twin-wire arc spray gun [3]. 7
1.8 Schematic diagram of a plasma spray gun [3]. 8
1.9 Schematic diagram of a wire flame spray gun [3]. 8
1.10 Schematic diagram of a HVOF spray gun[3]. 9
1.11 Hardness comparison for pure aluminum, pure nickel and 316 stainless steel, in annealed condition, fully worked and cold sprayed[4]. 10
1.12 Particle impact and break up of oxide layer [5]. 11
1.13 Plot of impact, critical, and erosion velocity for Cu using He as the main process gas at P =30 bar and T =300^{o}C [2]. 14
1.14 Particle and gas velocities as a function of distance along the nozzle. Different particle diameters are indicated in microns [6]. 15
1.15 Particle and gas temperatures as a function of distance along the nozzle. Different particle diameters are indicated in microns [6]. 16
1.16 Coating thickness as a function of the gas inlet temperature for iron powder sprayed onto aluminum, brass, copper, and steel substrates [6]. 16
1.17 Coating thickness as a function of the gas inlet temperature for copper powder onto aluminum, brass, and copper substrates [6]. 17
1.18 Impact velocity(solid) compared to exit velocity (dotted) of copper particles of different diameters [7]. 18
1.19 Impact behavior of different particle-substrate hardness combinations [8]. . 19
1.20 Maximum compressive residual stress and depth of it for different specimens [9]. 22

1.21 Fatigue strength for different specimens [9]. 22
1.22 Hardness of SiC-reinforced Al–12Si coatings as a function of the SiC content [10]. 23

2.1 Comparison between DE obtained experimentally and DE calculated with the ROM [11]. 26
2.2 Comparison between DE obtained experimentally and DE calculated with the BRST [11]. 29
2.3 Impact scenarios during CS of two-component powder mixture of "soft" and "hard" metals [12]. 30
2.4 Percentage of cermet in the coating compared with the weight fraction initially sprayed [13]. 33
2.5 DE of cermet in the coating compared with the weight fraction initially sprayed [13]. 33
2.6 Schematic of the iterative process employed to calculate the layer compositions [14]. 36
2.7 Comparison between the DE of the different samples and that calculated with the model [14]. 36
2.8 Comparison between the experimentally obtained composition for the 60% Al–40% Zn sample and the composition predicted by the model [14]. 37

3.1 Contact interface of the copper particles for different mesh sizes (a)0.5μm, (b)1.5μm and (c)2.0μm [15]. 40
3.2 (a) Equivalent plastic strain and (b) temperature of an Aluminum particle impacting onto an Aluminum substrate[16]. 41
3.3 Equivalent plastic strain for Al on Al impact simulation at 700 mm/s using SPH method [16]. 42
3.4 Time history of the equivalent plastic strain for Al on Al impact simulation at 700 mm/s using SPH method[16] 42
3.5 (a) Equivalent plastic strain in the Al particle and (b) equivalent plastic strain in the Al substrate at 700 mm/s using CEL method [16]. 42
3.6 Assembly used for the case where particle suffers larger plastic deformations 46
3.7 Assembly used for the case where substrate suffers larger plastic deformations 46
3.8 Substrate dimensions for different scenarios depending on the particle's plastic deformation: (a) large plastic deformation in the particle, (b) very large plastic deformation in the particle, and (c) large plastic deformation in the substrate. 47

3.9 Void dimensions for different scenarios depending on the particle's plastic deformation: (a) large plastic deformation in the particle, and (b) very large plastic deformation in the particle. 48
3.10 BC applied to the substrate 49
3.11 Predifined fields applied to the assembly 49
3.12 "Void" and substrate mesh for a 3D CEL model 50

4.1 Probability distribution for both Al and Fe powders 51
4.2 Spray gun mounted on the robotic arm. 52
4.3 Impact Innovations ISS 5/11 spray gun 52
4.4 Impact powder feeders 52
4.5 (a) Image obtained with the SEM microscope for a coating with a feedstock of 50% Al and 50% Fe on an aluminum substrate, and (b) composition analysis performed using ImageJ software. 54
4.6 (a)Layout of the experimental tests, and (b) samples before the spraying process 55
4.7 Anton paar Step machine 55
4.8 Sample holder in Anton paar machine 55
4.9 Schematic of the sections used for the calculation of theoretical deposited mass for a single pass. 57
4.10 Flow diagram used for the prediction of the composition in the coating . . 59

5.1 Fe on Al powder impact simulation 66
5.2 Distorted elements in an Fe on Al powder impact simulation 66
5.3 Al on Al powder impact simulation with a particle diameter of 20.39μm . 66
5.4 Al on Al powder impact simulation with a particle diameter of 32.1μm . . 66
5.5 Al on Al powder impact simulation with a particle diameter of 53.11μm . 66
5.6 Al on Al substrate impact simulation with a particle diameter of 32.1μm . 67
5.7 Al on Fe powder impact simulation for with a particle diameter of 32.1μm 67
5.8 Fe on Fe powder impact simulation with a particle diameter of 31.53μm . 67
5.9 Fe on Al powder impact simulation with a particle diameter of 31.53μm . . 68
5.10 Fe on Al substrate impact simulation with a particle diameter of 31.53μm . 68
5.11 Aluminum particles deposited on an aluminum substrate 69
5.12 Aluminum particle deposited on an iron substrate 69
5.13 Iron particle deposited on an aluminum substrate 69
5.14 Iron particle deposited on an iron substrate 69
5.15 Samples used to determine the amount of deposited material 70

5.16 Coating performed with a Feedstock of 25% Al and 75% Fe on an aluminum substrate . . . 72
5.17 Coating performed with a Feedstock of 50% Al and 50% Fe on an aluminum substrate . . . 72
5.18 Coating performed with a Feedstock of 75% Al and 25% Fe on an aluminum substrate . . . 73
5.19 Comparison between the DE predictive model and the experimentally determined composition obtained for a feedstock of 25%Al and 75%Fe for an aluminum alloy substrate. . . . 74
5.20 Comparison between the DE predictive model and the experimentally determined composition obtained for a feedstock of 50%Al and 50%Fe for an aluminum alloy substrate. . . . 75
5.21 Comparison between the DE predictive model and the experimentally determined composition obtained for a feedstock of 75%Al and 25%Fe for an aluminum alloy substrate. . . . 76
5.22 Coating performed with a Feedstock of 25% Al and 75% Fe on an iron substrate . . . 76
5.23 Coating performed with a Feedstock of 50% Al and 50% Fe on an iron substrate . . . 76
5.24 Coating performed with a Feedstock of 75% Al and 25% Fe on an Aluminum substrate . . . 77
5.25 Comparison between the DE predictive model and the experimentally determined composition obtained for a feedstock of 25%Al and 75%Fe for an iron allow substrate. . . . 78
5.26 Comparison between the DE predictive model and the experimentally determined composition obtained for a feedstock of 50%Al and 50%Fe for a pure iron substrate. . . . 79
5.27 Comparison between the DE predictive model and the experimentally determined composition obtained for a feedstock of 75%Al and 25%Fe for a pure iron substrate. . . . 80
5.28 Predicted DE for 25%*Al*-75%*Fe*, 50%*Al*-50%*Fe*, and 75%*Al*-25%*Fe* onto an aluminum substrate. . . . 81
5.29 Predicted DE for 25%*Al*-75%*Fe*, 50%*Al*-50%*Fe*, and 75%*Al*-25%*Fe* onto an iron substrate. . . . 81

List of Tables

2.1 Bond ratio (BR) of single-component and multi-component coatings [11]. . 27

3.1 Material Properties of Aluminum and Iron 44
3.2 Johnson-Cook parameters for Aluminum, Al6082-T6, Iron, and Pure Iron ARMCO 45

4.1 Particle sizes and the probability of obtaining them 59

5.1 Splat radii for aluminum particles on different powder and substrates. . . . 68
5.2 Splat radii for iron particles on different powders and substrates. 68
5.3 Comparison between deposited, theoretical deposited material, and deposition efficiency (DE) for pure aluminum powder. 70
5.4 Comparison between deposited, theoretical deposited material, and deposition efficiency (DE) for pure iron powder. 71

Introduction

Cold spray (CS) is a manufacturing process that allows us to deposit material onto a substrate by accelerating micron-sized particles up to supersonic velocities. This process is used to produce coatings or near-net-shaped parts [17]. This technology has become of interest to several industries, such as aerospace, automotive, and electronics. The low working conditions and its ability not only to produce components but also to repair them have made it an interesting technology with various applications [18].

One of the main advantages of a CS process is its low working temperature, which avoids the melting of the particles and thus preserves their mechanical properties even after deposition. This significantly reduces the formation of intermetallic compounds and re-crystallization of the deposited material [4]. However, the process still presents some challenges related to the calculation of the deposition efficiency (DE), which is a critical parameter for understanding and optimizing the process. This issue becomes even more complex in cases where more than one type of material is being deposited.

The objective of this thesis is to develop a model that allows us to properly understand the coating formation in bimetallic coatings by modeling its DE and thus determining the coating composition. The scope of this research is to develop a predictive model and validate it through experimental tests. To achieve this, both experimental tests and numerical simulations will be performed, allowing us to properly understand the interactions between the selected materials, which for this research are pure aluminum and pure iron powders.

This thesis is divided into six different chapters, structured as follows:

- **Chapter One**: This chapter focuses on explaining the CS process, detailing how bonding is achieved, how different parameters affect particle deposition, and the uses and limitations of the process.
- **Chapter Two**: This chapter discusses the different DE predictive models that have been developed so far, which are crucial for properly understanding and optimizing bimetallic deposits.

- **Chapter Three**: The different FE particle impact simulation methods are explained here to understand and properly choose the most adequate method that allows us to model the interactions upon impact for the studied materials.
- **Chapter Four**: This chapter provides a detailed explanation of all the experimental procedures to be performed, along with a description of the developed DE predictive model.
- **Chapter Five**: Here, the results of the experimental tests, numerical impact simulations, and the DE predictive model are presented and analyzed.
- **Chapter Six**: Finally, the conclusions related to the FEM particle impact simulations, the predictive model, and future developments were included in this chapter.

1 | Cold Spray

1.1. Process description

The Cold Spray (CS) process is a material consolidation technique that uses supersonic acceleration of micron-sized particles , accelerated through a De Laval rocket nozzle to form a coating or a near-net shaped part. The particles are carried within a high-pressure and temperature gas, which usually is either helium, nitrogen or air in some cases [17].

Generally the size of the particles used in this process ranges from 1 to 50μm, these ones are sprayed at supersonic velocities typically from 300 to 1200 m/s by injecting them into a compressed gas jet. The particle size is really important since it affects both the deposition efficiency and the particle impact velocities [19]. The gases are supplied with pressures ranging from 1.0 to 8.5 MPa, the higher the pressure, the higher the particle impact velocity is going to be, these gases are preheated to temperatures up to 1000°C [2].

1.2. Classification according to the powder feeding and acceleration mechanism

According to T. J. Eden et al. [2] the cold spray systems can be classified according to the mode of operation, the powder feeding and acceleration mechanism.

Regarding the mode of operation there are three classifications, stationary, shop portable and hatchable. In a stationary system, the equipment is attached to a robot which is inside an acoustic room specifically designed for cold spray. The portable systems are usually mounted on carts allowing them to be transported. At last the hatchable are designed to be transported by hand.

With respect to the classification based on working pressure, there are two types of systems: high-pressure and low-pressure. Both systems can utilize either a supersonic nozzle or a sonic nozzle.

1.2.1. Classifying cold spray system according to the working pressure

High pressure cold spray systems

High pressure cold spray system or upstream cold spray system. This kind of system has two main characteristics. The first is its working pressure: Being a high pressure system, it allows the use of a wider range of powder materials due to the higher particle impact velocity that can be reached. The second characteristic is the powder injection method , an upstream cold spray system has the powder inlet on the convergent part of the de Laval nozzle. Since the pressure at this point is higher than the atmospheric pressure, a robust high-pressure powder feeder is required, a high-pressure cold spray system as shown in Figure 1.1 is conformed by a high-pressure gas source, a gas heater, and a de Laval nozzle to accelerate particles [1, 2].

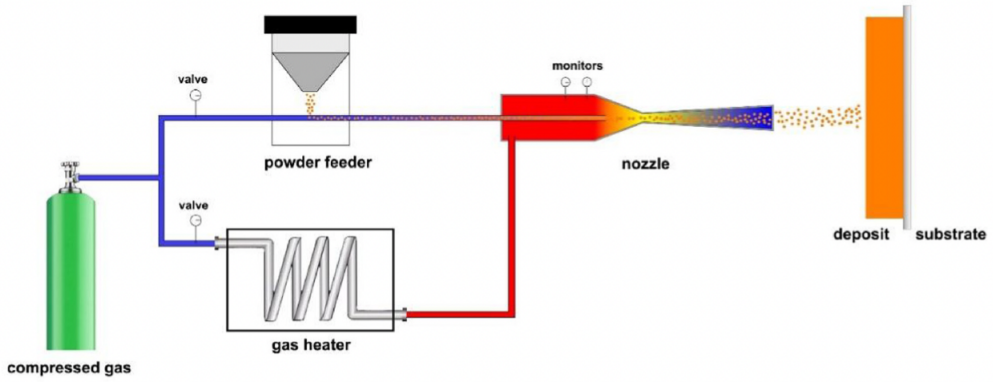


Figure 1.1: High pressure cold spray system [1].

Low pressure cold spray system

The low pressure cold spray system or downstream cold spray system works with lower pressures and because of that this system is less complex, but is limited to specific materials. The other difference with respect to the previous one is that here the powders are injected in the divergent part of the system. A low pressure cold spray system as shown in Figure 1.2 is simpler than the High pressure cold spray system, these ones usually have portable air compressors and a gas heater. [1, 17].

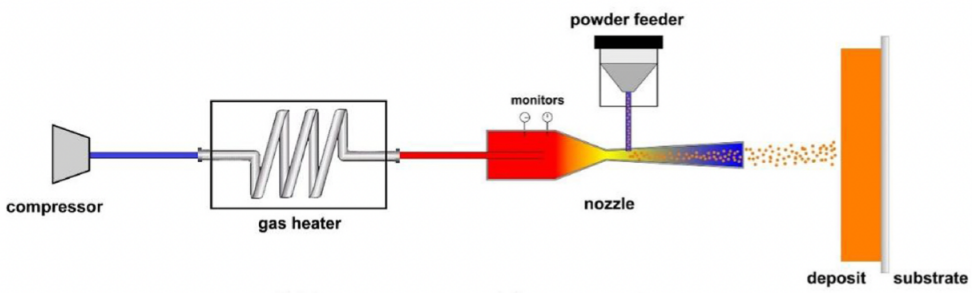


Figure 1.2: Low pressure cold spray system [1].

1.2.2. Nozzle classification

Since the CS process uses the kinetic energy of the particles to create bonding, the nozzles have a really important role in the process, being here where the kinetic and thermal energy are transferred from the gas to the particles. The nozzle serves three primary functions: to transform the gas's kinetic, thermal, and pressure energy into kinetic and thermal energy in the particles, to guide the particles toward the substrate, and to define the area where particles are deposited. The gas's thermal energy is increased by heating, while its potential energy is raised by applying higher pressure. As the gas moves through the nozzle, both its thermal and potential energy are converted into kinetic energy [17].

Supersonic nozzle

According to the description given by T. J. Eden et al. [2], the nozzles can be classified into the supersonic nozzle and sonic nozzle. The super sonic nozzle is used to accelerate the gas to a super sonic speed ($\sim 343 m/s$) to do this it has a convergent-divergent shape. The supersonic nozzle can have two different configurations, the first one a supersonic nozzle with a upstream powder injection as shown in Figure 1.3, where the powder is injected in the convergent section of the nozzle. Figure 1.4 represents the supersonic nozzle with downstream powder injection, where the powder injection is in the divergent region of the nozzle.

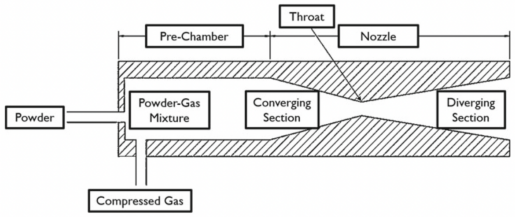


Figure 1.3: Supersonic nozzle with upstream powder injection [2].

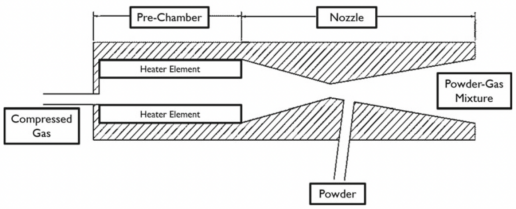


Figure 1.4: supersonic nozzle with downstream powder injection [2].

The main advantage of the supersonic nozzle is that after the nozzle throat the gas reach high speeds which is transferred to the powder particles but at the same time the temperature is kept considerably low as shown in the Figure 1.5

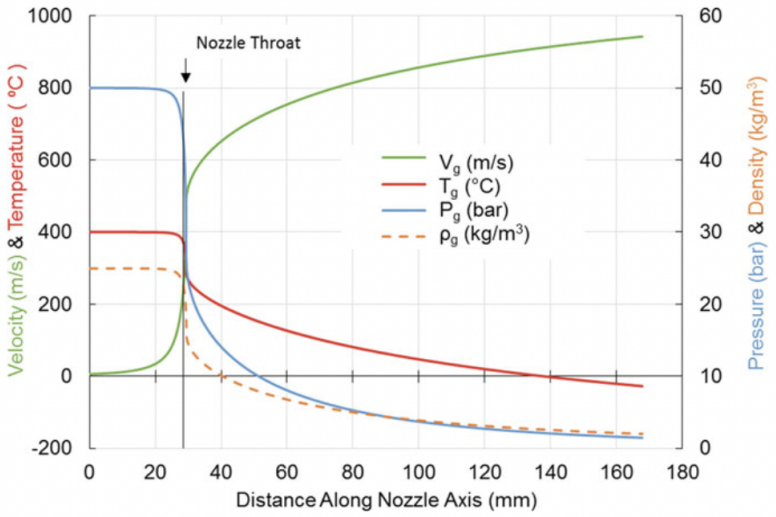


Figure 1.5: Gas pressure, temperature, velocity, and density as a function of distance in a sonic nozzle[2].

Sonic nozzle

Following the description given by T. J. Eden et al. [2] the sonic nozzles can also be used in a cold spray system. Its structure is much simpler, since a convergent-divergent shape is not required (Figure 1.6).

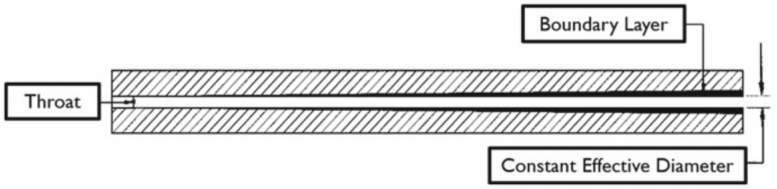


Figure 1.6: Schematic of a sonic nozzle[2].

1.3. Comparison between cold spray and thermal spray

According to the definition given by M.F. Smith [3] in a typical thermal spray process, electrical or chemical energy is utilized to generate small molten or semi-molten droplets, ranging in size from approximately 10 to 100 microns in diameter, from powder, wire,

or rod feedstock. These droplets are then propelled toward the substrate surface by a subsonic or supersonic gas stream, reaching velocities that vary from a few tens of meters per second to approximately 1000 m/s.

When the droplets impact the substrate, they spread and rapidly solidifies at cooling rates on the order of 10^4–10^8 K/s, the formed structures is called "splat" and this one is known as the fundamental microstructural unit of the spray-deposited material. Due to the high cooling rates, individual splats typically solidify before subsequent molten droplets arrive. As a result, these splats accumulate in a random stacking arrangement.

Typically, thermal spray processes are divided into two groups according to the heating mechanisms they utilize, there are those that utilize electrical energy and those that use chemical energy. For the electrical energy typically an electric arc or electric driven plasma are used, a example of a electric arc is the twin-wire arc spray shown in the Figure 1.7, this one use wires as a feedstock and those wire are melted once they get in contact with the electric arc, the melted material is accelerated by a jet of compressed air or inert gas.

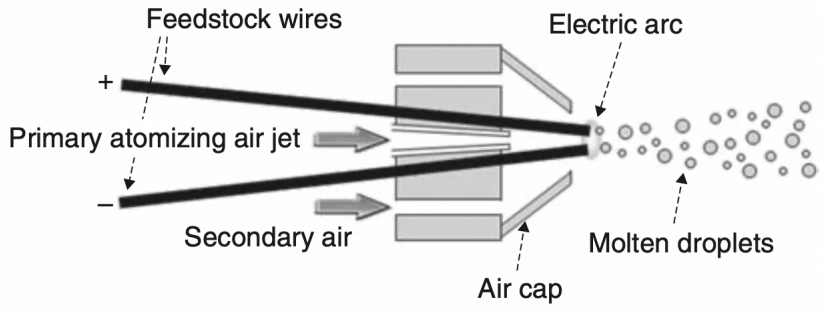


Figure 1.7: Schematic diagram of a twin-wire arc spray gun [3].

Another type of electric thermal spray is plasma spraying, in which a partially ionized conductive gas, known as 'plasma,' melts and propels the material, as shown in Figure 1.8. The material used in this process is typically metallic powder.

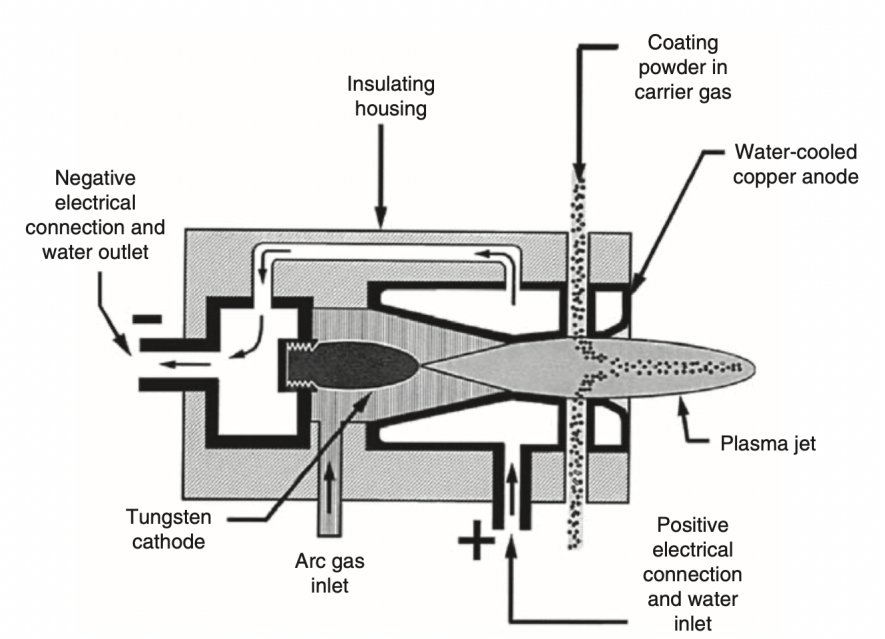


Figure 1.8: Schematic diagram of a plasma spray gun [3].

While in chemical thermal spray, one of the most common solutions is the flame spray. This one uses oxygen and fuel gases, which are burned in order to obtain the desired high temperatures that, upon contact with the feedstock, allow the melting of the material. This thermal spray process is very versatile in terms of feedstock selection; metallic powders, wire, or ceramic rods can be used. To accelerate the droplets, a jet of compressed air is used in this process, as shown in Figure 1.9.

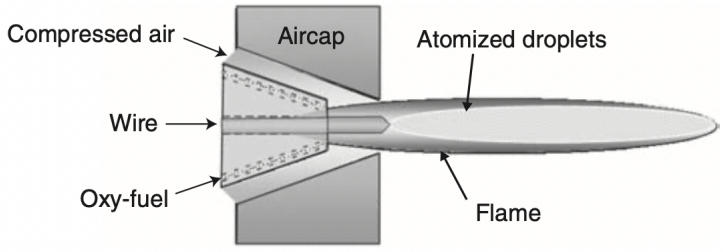


Figure 1.9: Schematic diagram of a wire flame spray gun [3].

High-Velocity Oxygen Fuel (HVOF) is also a chemical spray process, is similar to flame spray but the fuel gases and the compressed air are premixed in a high pressure chamber (Figure 1.10), another important change with respect to flame spray is that the heated gas passes through a converging-diverging nozzle allowing the gas to reach super sonic velocities.

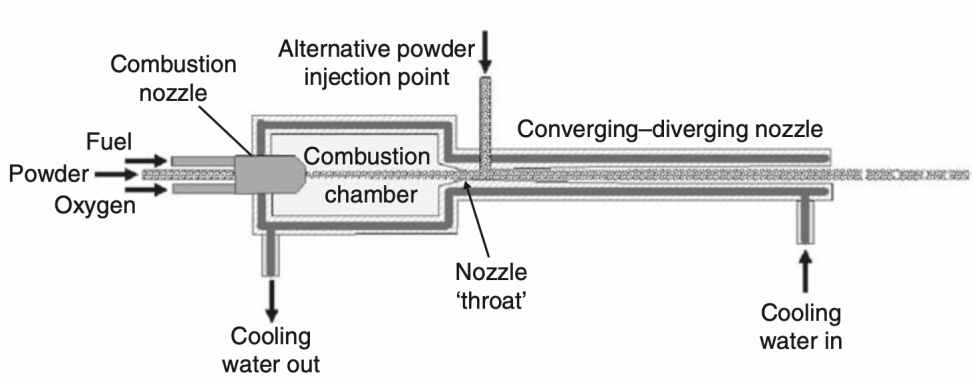


Figure 1.10: Schematic diagram of a HVOF spray gun[3].

As mentioned by V. K. Champagne Jr. [4], cold spray is often compared to conventional thermal spray processes such as flame spray, thermal arc, or HVOF. While both share some common aspects, understanding their differences is essential to selecting the appropriate technique for a given application. CS is usually used for dimensional restoration of engineering materials, particularly in the aerospace industry, where it helps recover high-value components affected by wear and corrosion. Additionally, it is a preferred option when the high temperatures associated with thermal spray could be detrimental to the substrate.

CS operates at lower temperatures with respect to thermal spray, which influences coating formation and material characteristics. It is commonly employed in applications requiring dense and strong deposits, especially for materials sensitive to heat exposure. Moreover, while thermal spray techniques have been explored for restoring certain aerospace components, the results have sometimes been inconsistent due to challenges in bond strength and coating integrity.

Given these factors, CS has gained attention as a viable alternative to traditional thermal spray processes, particularly in scenarios where temperature-sensitive materials or specific coating properties are required.

1.3.1. Advantages and limitations

One of the main advantages that CS presents over thermal spray is its relatively low working temperature. This avoids the emergence of problems such as intermetallic, grain growth, oxidation, and decomposition. Another critical issue mitigated by operating at lower temperatures is the presence of residual tensile stresses, which are typically developed at the substrate-coating interface and can lead to delamination. Furthermore,

since particles impact the substrate at very high velocities, a peening effect is generated, inducing compressive residual stresses, which are beneficial for many applications [4].

Another significant advantage of CS is that it is a solid-state process, which prevents splashing. This is beneficial for obtaining components with very low porosity [3, 4].

In terms of mechanical properties, both the strength and hardness of cold-sprayed components exhibit outstanding performance. The low porosity and minimal presence of material defects contribute to the production of near-net-shape parts, allowing for the achievement of high strength. The cold-sprayed parts also present a really high hard, as shown in the Figure 1.11. The reason behind this is that each individual micron-sized particle impacts the substrate, undergoing intense plastic deformation and experiencing a high level of strain, which significantly exceeds what can be achieved through conventional material processing methods [4].

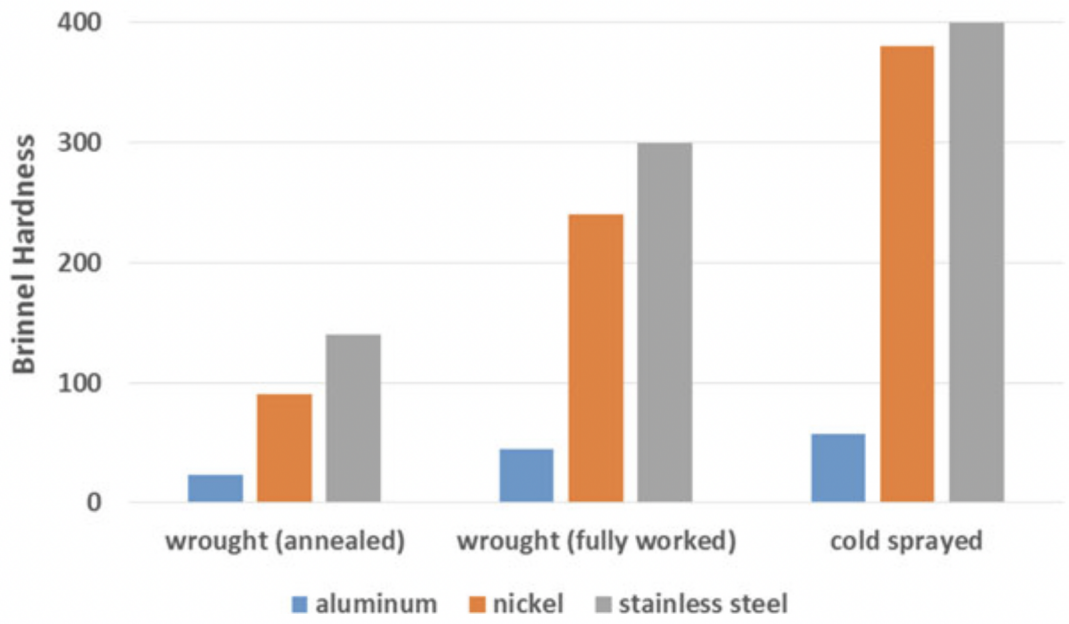


Figure 1.11: Hardness comparison for pure aluminum, pure nickel and 316 stainless steel, in annealed condition, fully worked and cold sprayed[4].

A wide range of materials can be used in the cS process. The low working temperature allows the proper use of materials such as pure metals, cermets, and some polymeric materials. Additionally, for the same reason, cold spray can also be applied to heat-sensitive substrates without compromising their mechanical properties. Furthermore, cold spray enables the use of new material combinations that would not be possible with thermal spray due to solubility limitations [4].

The limitation of materials that can be used in the cold spray process is related to the bonding mechanism. Since particles need to undergo high plastic deformation, this requirement reduces the selection of powder materials to those with sufficient ductility, allowing the necessary plastic deformation and the formation of hydrodynamic shear instability [3].

1.4. Bonding mechanism and deposition efficiency

1.4.1. Bonding mechanism

The bonding mechanisms in CS, although still a matter of debate, are generally classified into two groups: mechanical and metallurgical bonding. These mechanisms are influenced by several factors, including particle impact velocity, substrate and particle material properties and the removal of oxide layers. High velocity impacts are critical in the process as they remove the oxide layers from both the particles and the substrate, exposing clean material and facilitating the bonding as shown in Figure 1.12. Additionally, adiabatic shear instability (ASI) plays a key role in bonding by generating localized shear strain at the particle-substrate interface during high-velocity impacts. This phenomenon creates favorable conditions for both mechanical and metallurgical bonding. Here the two bonding mechanisms, mechanical and metallurgical bonding often coexist [2].

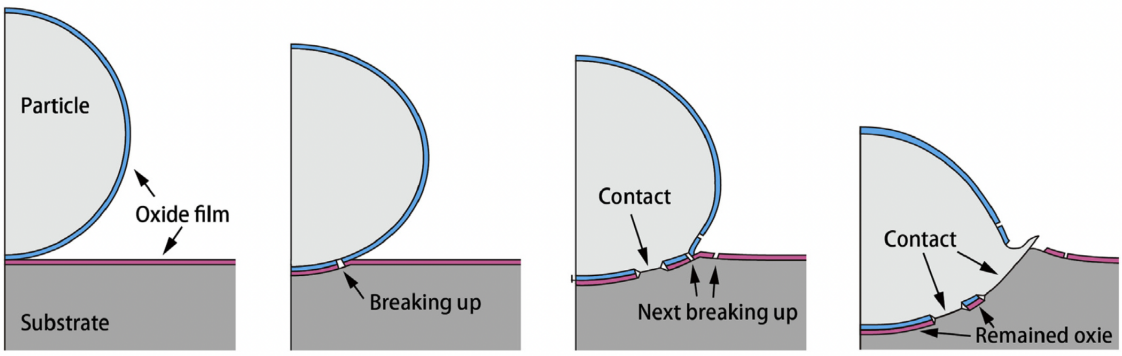


Figure 1.12: Particle impact and break up of oxide layer [5].

Adiabatic shear Instability (ASI)

Adiabatic shear instability is known as the predominant bonding precursor in cold spray. This process occur in the interface of the particle-substrate during impact. Due to the impact a strong pressure field is introduced, this one produce shear loads that accelerate the material laterally, causing localized shear straining which under critical conditions results

in adiabatic shear instability. ASI is critical for achieving bonding because it promotes intense plastic deformation at the interface, allowing the metallurgical and mechanical bond to form [2, 20].

Adiabatic shear instability is usually initiated due to the balance between thermal softening and strain rate hardening. During high strain rate deformation, strengthening occurs as a result of the generation and movement of dislocations. Simultaneously, these dislocations, heat is generated by the plastic work while softening the material making it more malleable. The balance between these two phenomena is critical, as it determines whether ASI occurs or not. This balance is dependent on the impact velocity, with the threshold for ASI being similar to the critical impact velocity required for proper material deposition [20].

Mechanical bonding

Mechanical bonding is usually characterized by particles anchoring and embedding into the substrate, primarily through physical interlocking rather than chemical interactions. This kind of bonding is usually predominant when the particles do not undergo significant plastic deformation, so all the kinetic energy is dissipated upon impact by a significant plastic deformation on the substrate generating a "wavy" interface [21]. However, mechanical bonding on its own presents considerably lower adhesion strength compared to metallurgical bonds [2].

Metallurgical bonding

This type of bonding in cold spray is achieved when atomic-level contact is made between clean metallic surfaces facilitated by the removal of oxide layers. The intense outward flow of material at the particle-substrate interface, known as "jetting," is beneficial for this bonding process as it typically removes surface oxide layers, exposing fresh, reactive surfaces that allow metallurgical bonding to occur. In addition to having a clean surface, high pressure and temperature are required to have this kind of bond, this is provided due to the energy dissipation during the particle impact [2, 21].

1.4.2. Deposition efficiency (DE)

Deposition Efficiency (DE) is a critical parameter in the cold spray process, used to optimize performance and calculate the cost of coating applications. T. J. Eden et al. [2] defined DE as the ratio of the weight of powder successfully bonded to the substrate (Δm) to the total weight of powder passing through the nozzle (M_0), described by the Equation (1.1):

$$DE = \frac{\Delta m}{M_0} \tag{1.1}$$

This parameter usually range from a few percent to values up to 90%. Different strategies can be followed to improve the deposition efficiency, like increasing gas temperature and pressure, optimizing nozzle design and selecting properly the particle size and materials and the gas this will be deeply explained in section 1.5 and 1.6.

Overall, achieving high deposition efficiency involves balancing process costs, gas selection, and powder preparation with the desired coating properties and economic constraints.

1.5. Temperature and particle velocity

The CS is a process that allow us to deposit material without reaching a melting point, and therefore reducing the oxidation and the residual stresses. Van Steenkiste [6] studied the influence of different parameters in the particle impact velocity and temperature and therefore in the deposition efficiency.

Since the CS process relies on the kinetic energy of the powders, Champagne et al. [2] studied the effect of particle impact velocity. They identified two main concepts that determine whether the material is deposited or not, being these ones the erosion velocity and the critical impact velocity.

The critical impact velocity predicts the minimum velocity required for a particle to undergo sufficient plastic deformation and be properly deposited. If this velocity is not reached, the particles will rebound without adhering to the substrate. Conversely, the erosion velocity is the velocity at which the substrate becomes damaged, preventing particle deposition. As shown in the Figure 1.13

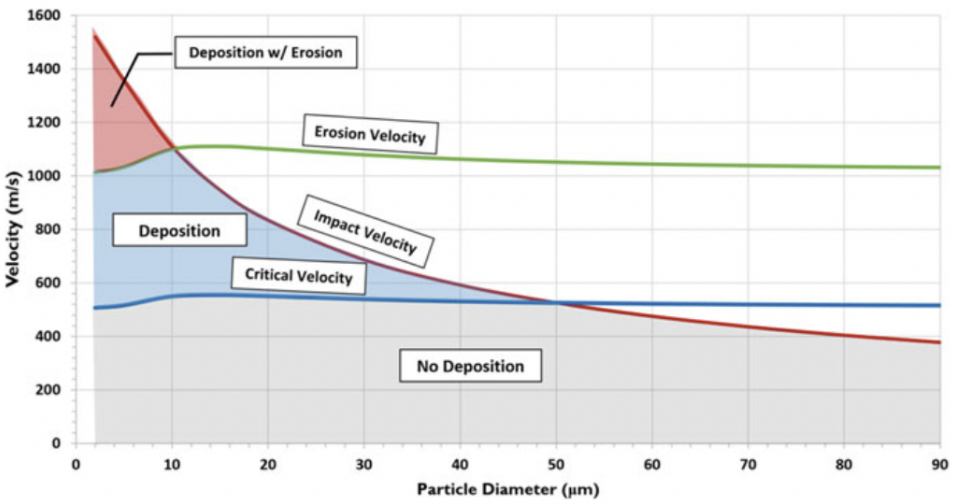


Figure 1.13: Plot of impact, critical, and erosion velocity for Cu using He as the main process gas at P =30 bar and T =300ºC [2].

According to Nikbakht et al. [22] the critical impact velocity has a dependency on the particle material, shape and temperature, following the relationship of the Equation (1.2).

$$v_{cr} = k_1\sqrt{c_p(T_m - T_p)} + 16\frac{\sigma}{\rho_p}\frac{(T_m - T_p)}{(T_m - 293)} \tag{1.2}$$

Where v_{cr} is the critical impact velocity, k_1 is a fitting parameter dependent on particle size, c_p is the specific heat capacity of the particle material, T_m is the melting temperature of the particle material, T_p is the particle temperature upon impact, σ is the tensile strength of the particle material, and ρ_p is the density of the particle material. The term 293 K represents the ambient temperature.

Following the studies realized by Van Steenkiste [6] there are several factors that affects the particle impact velocity, being the first one the gas velocity that follows the relationship of the Equation (1.3)

$$v = \left(\frac{\gamma RT}{M_w}\right)^{1/2} \tag{1.3}$$

Where γ is the ratio of specific heats, R is the gas constant, T is the gas temperature and M_w is the molecular weight of the gas.

In the Figure 1.14 are indicated the particle and gas velocities along the nozzle. From this figure, it can be observed that the particles with smaller diameter tend to reach slower

velocities, due to the interaction with the gas, which will be explained more in depth in the subsection. 1.6.1

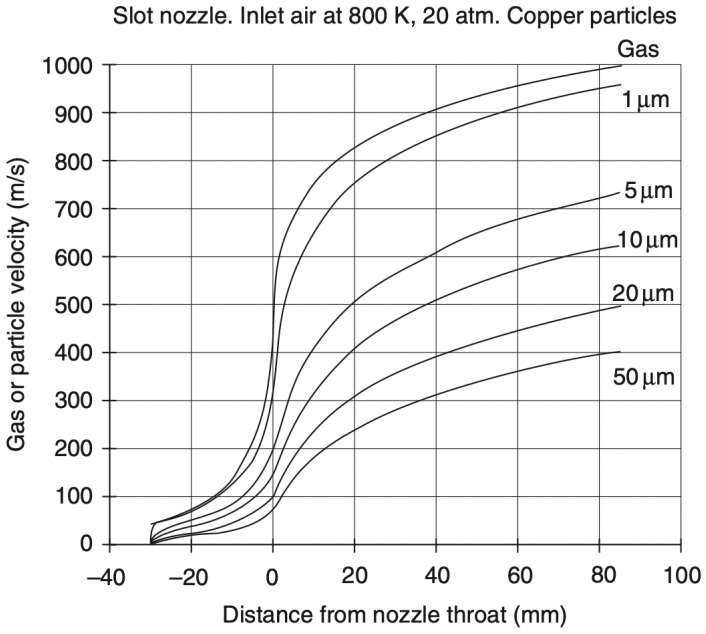


Figure 1.14: Particle and gas velocities as a function of distance along the nozzle. Different particle diameters are indicated in microns [6].

Regarding temperature, Figure 1.15 shows the particle and gas temperature along the nozzle. Understanding the temperature of the particle is crucial because it affects the particle material properties such as Young's modulus which tends to be lower for high temperatures, and so the particles present more plastic deformation later will have an effect on the deposition efficiency.

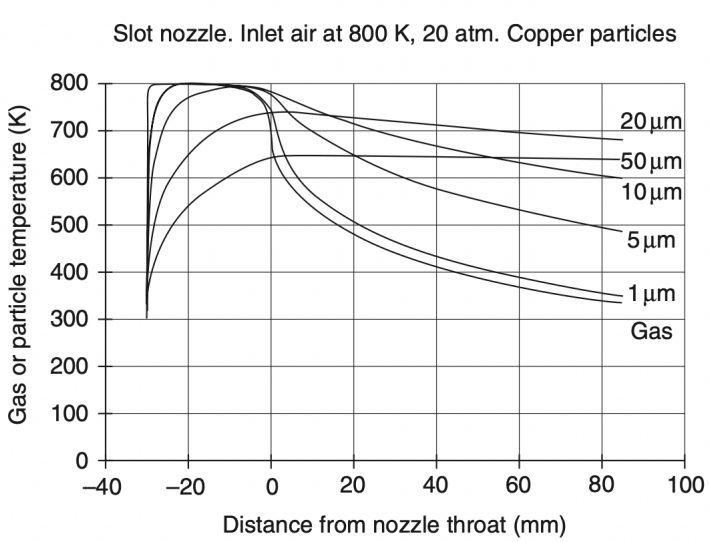


Figure 1.15: Particle and gas temperatures as a function of distance along the nozzle. Different particle diameters are indicated in microns [6].

From Figures 1.16, 1.17, it can be observed that the maximum coating thickness depends on the interaction between the powder and the substrate. Additionally, it is influenced by the gas temperature and so particle temperature. Higher gas temperatures lead to greater coating thickness, thereby improving deposition efficiency.

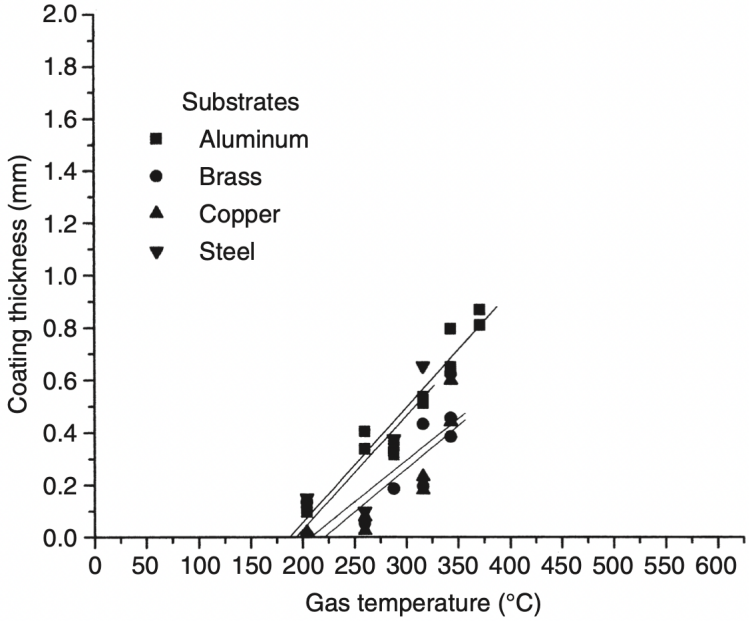


Figure 1.16: Coating thickness as a function of the gas inlet temperature for iron powder sprayed onto aluminum, brass, copper, and steel substrates [6].

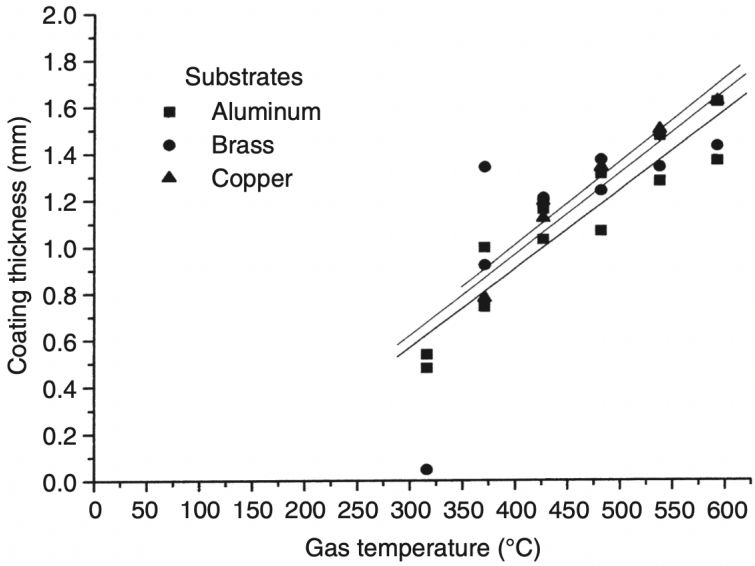


Figure 1.17: Coating thickness as a function of the gas inlet temperature for copper powder onto aluminum, brass, and copper substrates [6].

1.6. Cold spray feedstock powders

1.6.1. Powder size effect

The particle size according to Nastic et al.[23] affects directly the impact velocity and temperature, due to its interaction with the gas flow and particle dynamics.

By applying a force balance, a relation between the particle size and its acceleration can be established according to the equation (1.4),

$$ma_p = \frac{1}{2}\rho V^2 C_d A_p \tag{1.4}$$

Where m is the particle mass, a_p is the acceleration of the particle, ρ is the gas density, V is the gas velocity, C_d is the drag coefficient, and A_p the cross-sectional area of the particle. Since both, the mass and cross-section are a function of the diameter, the equation (1.4) can be simplified into (1.5).

$$a_p = \frac{3\rho V^2 C_d}{\rho_p d} \tag{1.5}$$

Where d is the particle diameter and ρ_p is the density of the particle material. From

equation (1.5) it becomes clear that smaller particles have higher acceleration. Even though the particle acceleration is higher for smaller particles, this does not directly translate to impact velocity. Particles experience deceleration within the stagnant region behind the bow shock, as shown in Figure 1.18, where it can be observed that, for larger particles, the difference between exit velocity and impact velocity is nearly negligible.

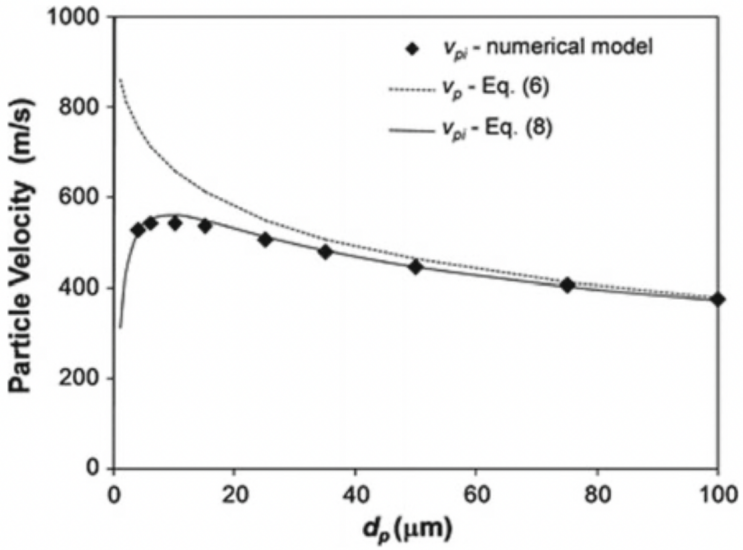


Figure 1.18: Impact velocity(solid) compared to exit velocity (dotted) of copper particles of different diameters [7].

1.6.2. Material effect

Both feedstock and substrate properties have a important role in the deposition efficiency. The soft particles tend to present larger deformation on impact compared to the hard ones, this is beneficial for the adhesion strength. Hard particles on the contrary produce more erosion upon impact with the substrate inducing damage to it. The substrate hardness is also relevant for the deposition mechanism, a "soft-soft" arrange enhance the adhesion strength [8, 24].

According to Nardi et al.[24] the relative hardness between the substrate and particle introduce additional considerations:

- If the substrate is significantly harder than the particles, the particles flatten on the surface barely generating substrate deformation. This typically leads to weaker bonds, as the substrate does not experience sufficient interfacial mixing with the particles.

- On the contrary , when the substrate is much softer with respect to the particles, the particles penetrate deeply into the substrate with minimal deformation. While this can lead to mechanical anchoring, it often creates bonding issues in subsequent layers. The first layer of particles is prone to being dislodged by new impacts, leading to erosion and poor adhesion.

Therefore, an optimal selection of particle and substrate is crucial to ensure maximum deposition efficiency and adhesion strength while also preventing erosion.

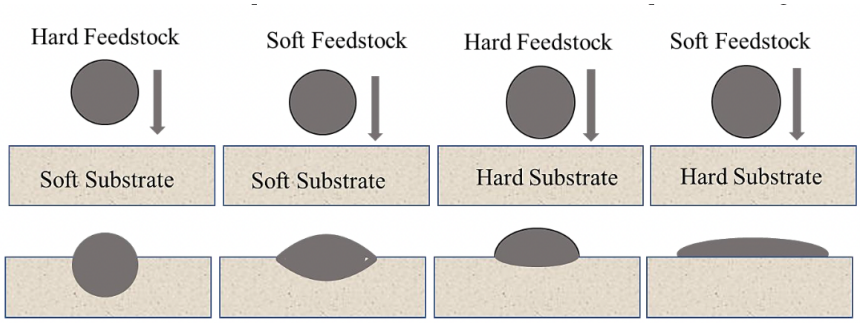


Figure 1.19: Impact behavior of different particle-substrate hardness combinations [8].

1.6.3. Morphology effect

Two particle morphologies are commonly used in CS: irregular and spherical. Irregular shaped particles exhibit higher average velocities compared to spherical ones of the same size due to their higher drag coefficients. However, spherical particles are generally preferred for their ability to achieve stronger adhesion and denser coating micro structures. Spherical particles penetrate deeper into the substrate which generates jet formation, enhancing the adhesion strength. In contrast, irregular particles tend to produce an uneven interface and insufficient deformation, resulting in lower adhesion strength [8].

The porosity is also a parameter to consider in the powder morphology this kind of structure allow the extraction of energy by mean of collapsing this porous structures during the plastic deformation [24]. The porosity level in spherical particles positively influences the plastic deformation rate, which, in turn, enhances bond strength and simplifies the spraying process for porous powders, because of that fully dense particles require greater kinetic and thermal energy to achieve effective adhesion to the substrate [25].

1.7. Possible application

CS allows the formation of dense coatings or near-net-shaped parts without melting the feedstock material, preserving its original microstructure, grain size, and properties. CS offers a unique combination of advantages, such as low-temperature operation, minimal oxidation, and high deposition rates, making it suitable for a wide range of materials, including metals, polymers, and composites.

Over the years, CS has gained significant attention for its diverse applications across industries such as aerospace, automotive, electronics, and medical. Its ability to repair, restore, and protect surfaces has made it a preferred technology in structural repairs, dimensional restoration, and additive manufacturing. Additionally, CS coatings are known for their excellent performance in enhancing corrosion resistance, wear resistance, and fatigue life [18].

1.7.1. Cold spray coatings used to improve corrosion resistance

Corrosion is the degradative process in which a material or its functionality is compromised due to interactions with the surrounding environment. To address corrosion challenges, two fundamental strategies are commonly adopted. The first involves utilizing materials science and engineering to modify the composition and microstructure of bulk materials at the microscopic level, enhancing their inherent resistance to corrosion. The second strategy focuses on designing and applying engineered surface coatings to base materials that are prone to corrosion. These coatings provide improved corrosion resistance to critical areas or act as protective barriers between the metal and its environment [20].

S. M. Hassani-Gangara et al. [20] conducted a research focused on the use of cold spray technology to produce corrosive resistance coatings. These coatings outperforms thermal spray mainly due to the fact that the particles impact the substrate in a solid state, avoiding defects from liquefaction and solidification. The resulting coating are dense, with low porosity which is beneficial for the corrosion resistance, additional to it the coatings due to the peening effect induce a compressive residual stress in both coating and substrate, and thus the delamination tendencies is reduced compared to the tensile residual stresses induced by thermal spray. However, cold spray has some drawbacks, such as lower portability of equipment, risks associated with powder handling, and higher costs. Authors also discovered that in order to achieve higher corrosion resistance the process parameters of cold spray need to be optimized. First increasing temperature and pressure enhances the bonding, cohesion strength and reduce porosity which improves corrosive resistance,

but excessively high temperatures can lead to localized plastic deformation. The particle size is also important, smaller particles produce coatings with a higher density.

The choice of carrier gas significantly influences the coatings quality. Helium is beneficial for the density of the coating but may lead to higher deformation. A mix between helium and nitrogen tend to have a better performance by balancing plastic deformation and coating porosity. Lastly, post-treatment processes, such as heat and laser treatments, can further improve bonding by reducing porosity and eliminating weak interparticle boundaries, ultimately enhancing corrosion resistance.

Cold spray technology offers a versatile solution for enhancing corrosion resistance across various industries. From improving the biocompatibility and durability of biomedical implants to protecting electronic components and mitigating corrosion in naval and energy applications, its adaptability is evident. By addressing specific challenges such as cavitation erosion, hot corrosion, and material degradation, cold spray has established itself as a vital tool in modern corrosion protection strategies.

1.7.2. Fatigue resistance improvement through cold spray

In the aerospace industry, many components are still manufactured using aluminum, titanium and magnesium based alloys and the use of cold spray is beneficial to repair these components, because it can overcome some limitations presented in the other existing technologies like tungsten inert gas (TIG) welding. Due to the low temperature deposition which prevent melting, development of tensile residual stresses, part distortion and undesirable chemical reactions [20].

A. Moridi et al. [9] studied the fatigue resistance of a component that was coated with a Al 6082 cold spray coating combined with a pre- and post-treatment of shot peening (SP) and severe shoot peening (SSP).

The combination of this processes induced a compressive residual stress as shown in Figure 1.20. They all present a similar value of maximum compressive residual stress, the main difference is presented in the depth of the compressed layer where the use of SP and SSP present as a pre-treatment obtains a deeper compressed layer.

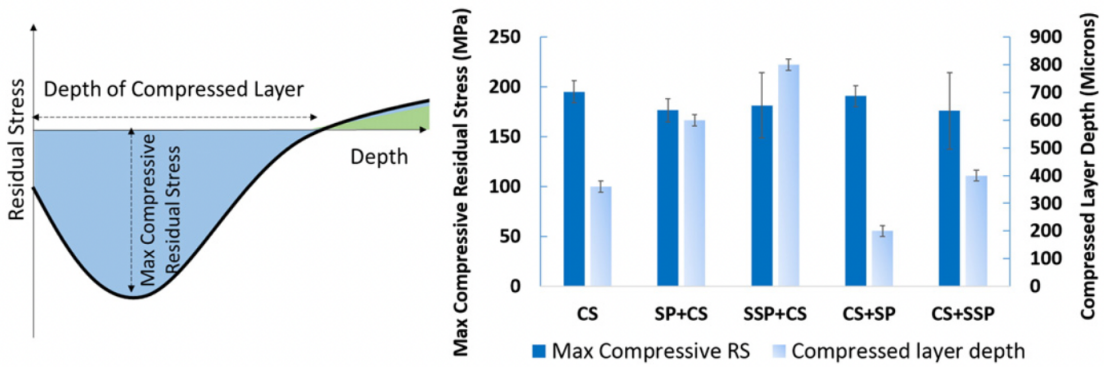


Figure 1.20: Maximum compressive residual stress and depth of it for different specimens [9].

While for the fatigue strength as shown in Figure 1.21. The cold spray coating by itself already present a improvement but this one is enhanced if conventional or severe shoot peening are applied as a pre-treatment

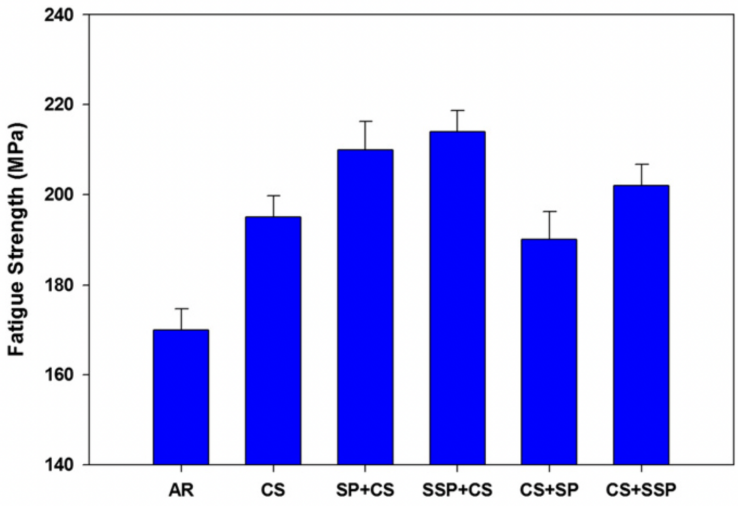


Figure 1.21: Fatigue strength for different specimens [9].

A. Morodi et al. [9] concluded that cold spray coating increased fatigue strength by 15% compared to untreated specimens. However, post-treatment with SP or SSP did not further improve the fatigue strength, as the peening effect caused plastic deformation in the underlying material, leading to coating damage and that acted initial cracks under fatigue loading.

If the shot peening was performed before CS there was a significant improvement of the fatigue strength, with severe shot peening resulting in a 26% increase compared to

untreated specimens.

1.7.3. Wear resistance enhancement

Metal matrix composites (MMCs) have become really relevant materials across a range of industries, including aerospace, automotive, and electronics. These composites are designed to achieve superior properties by incorporating a determinated amount of reinforcement into the metal matrix. By reinforcing alloys with ceramic particulates, significant property enhancements can be achieved, such as increased hardness, improved wear resistance and higher yield strength. Among the possible matrix materials, aluminum and its alloys are particularly interesting for MMC fabrication due to their versatility, lightweight , and excellent mechanical properties [10].

From the research performed by E. Sansoucy et al. [10], it can be stated that CS is an effective method for producing aluminum alloy coatings reinforced with silicon carbides (SiC), which significantly enhance the wear resitance. The process involves embedding SiC particles within an Al–12Si matrix, resulting in coatings with low porosity (below 1%) and a uniform particle distribution. The SiC included on the coating improves mechanical properties like the hardness, which is strictly related with the wear resistance.

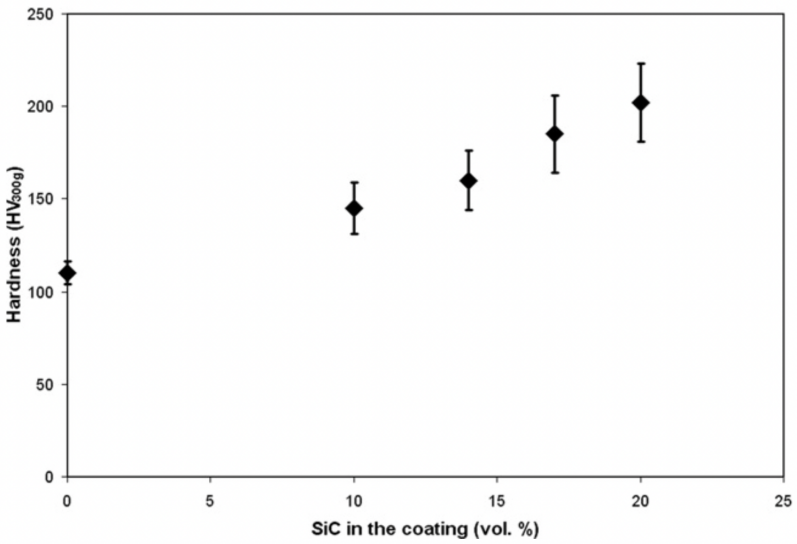


Figure 1.22: Hardness of SiC-reinforced Al–12Si coatings as a function of the SiC content [10].

Another advantage of CS is the ability to avoid common issues found in other thermal spray techniques, such as oxidation and clustering of reinforcement particles. The SiC particles remain uniformly distributed within the aluminum matrix without significant

agglomeration, preserving the integrity of coating and the wear resistance. Moreover, the cold spray process prevents melting of the feedstock material, which helps maintain the original properties of the SiC and aluminum alloy.

These SiC-reinforced aluminum alloy coatings are particularly suitable for applications in the aerospace and automotive industries, where high wear resistance is critical for performance and durability.

2 | Modeling of Deposition efficiency

2.1. Different models that estimates the deposition efficiency in a cold spray mixture

The possibility to deposit multi-component coatings is one of the significant advantages of CS. The simplest way to achieve these coatings is by spraying pre-mixed powder blends.

However, multi-component coatings present certain drawbacks related to the bonding mechanism of the conventional CS process. The presence of different materials complicates process setup, as selecting optimal spraying conditions for one material may result in non-ideal conditions for another. This challenge becomes even more complex due to the fact that each material requires a specific impact kinetic energy to achieve proper adhesion, which depends on its mechanical and thermal properties. Harder materials generally demand higher impact velocities, while increasing the temperature of either the particles or the substrate can help reduce the critical velocity required for bonding. Moreover, in powder mixtures, the gas flow parameters optimized for one component may be ineffective for another, further complicating the optimization of spraying conditions [12].

Due to this complexity, analyzing the composition and DE for these mixtures has been a major challenge throughout the years, leading to numerous studies. One key aspect of cold spray coating deposition is that it occurs in two distinct steps: first-layer formation and coating build-up [11]. Based on these studies, several models have been developed, including the following:

- Rule of Mixture (ROM) [11]
- Bond ratio splat test based model (BRST) [11]
- Semi-empirical probability model (SEP) [12, 13]
- FEM assisted DE predictive model [14]

2.1.1. Rule of mixture (ROM)

The rule of mixture (ROM) is a model used by X. Chu et al. [11]. This model allows us to calculate the deposition efficiency (DE) for a multi-component CS process with different feedstock compositions. In their research, they worked with 316L stainless steel and pure iron. This model was compared with the experimental DE values obtained from six samples. Two of them were single-component coatings of pure iron and pure 316L stainless steel, while the other four were multi-component coatings with varying weight fractions of iron: 10% Fe, 50% Fe, 80% Fe, and 90% Fe.

DE values were calculated following the procedure explained in Subsection 1.4.2, where the total mass gain during the CS process was divided by the total sprayed material fed into the system. With this data, the deposition efficiency for different compositions can be calculated using equation (2.1).

$$DE = DE_A \times f_A + DE_B \times f_B; \tag{2.1}$$

In equation (2.1), A and B correspond to the studied materials, which, in the research conducted by X. Chu et al. [11], are 316L stainless steel and pure iron, respectively. DE_A and DE_B represent the DE for the single-component coatings, while f_A and f_B denote the weight fractions of both materials. Then the comparison between the experimental results and the predictive model is shown in the Figure 2.1.

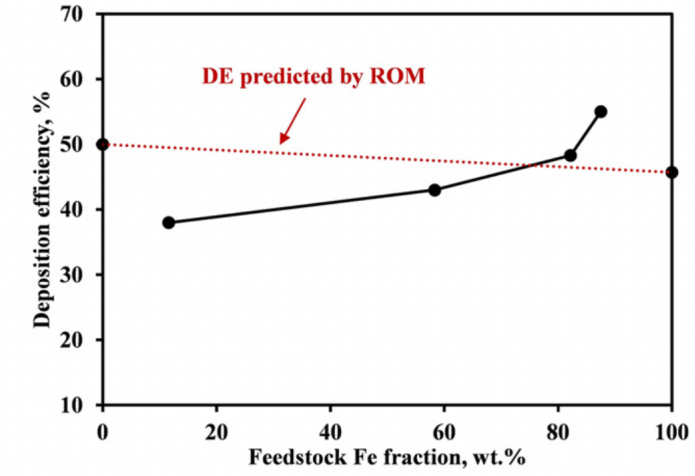


Figure 2.1: Comparison between DE obtained experimentally and DE calculated with the ROM [11].

The ROM model predicted a decreasing DE as the Fe% increased, which is completely

different from the experimental data. The experimental results show an increase in DE with increasing Fe%, even reaching a value higher than that of the coating where only stainless steel was used, specifically at an iron percentage of 90%.

This model can be considered a simple predictive tool. However, since it does not account for interactions between the powders and treats them as independent components, it leads to undesirable results [11].

2.1.2. Bond ratio splat tests based model (BRST)

The BRST model, developed by X. Chu et al. [11], is an improvement over the ROM model. Unlike the ROM model, this model takes into account the interaction between different materials by introducing the bond ratio (BR). The BR was defined by J. Wu et al. [26] as an alternative to DE, calculated as the ratio between the number of deposited particles and the total number of deposited particles and craters on the substrate. BR is considered as a count-type measurement, while DE, as defined previously, is a weight fraction.

X. Chu et al. [11] studied the BR of 316L stainless steel and pure iron not only in single-component coatings but also in the various multi-component coatings mentioned in Subsection 2.1.1. To obtain these bond ratios, splat tests were performed, and the samples were polished to a mirror finish before spraying to clearly reveal craters and deposits. Afterward, the samples were analyzed using a scanning electron microscope (SEM), so from this the bond ratio was following the definition given by J. Wu et al[26], as shown in the Equation (2.2)

$$BR_A = \frac{N_{deposits}}{N_{deposits} + N_{craters}} \tag{2.2}$$

After performing the splat test the BR were calculated for the different coatings as shown in Table 2.1.

Sample	316L BR, %	Fe BR, %
On 316L	45.8	87.3
On Fe	8.3	38.3
On 10Fe	35.8	59.5
On 50Fe	16.0	54.8
On 80Fe	12.3	54.3
On 90Fe	7.9	55.0

Table 2.1: Bond ratio (BR) of single-component and multi-component coatings [11].

By including the BR, the DE can be calculated. To do so, the masses of both 316L and Fe must first be determined. For generalization, these materials will be referred to as A and B, respectively.

$$dM_A = n_A m_A BR_A \tag{2.3}$$

$$dM_B = n_B m_B BR_B \tag{2.4}$$

From Equations (2.3) and (2.4), dM_A and dM_B correspond to the total mass of 316L and Fe in the coating, m_A and m_B represent the mass of a single particle, n_A and n_B denote the number of particles impacting the substrate, and BR_A and BR_B correspond to the bond ratios, which define the probability of particles from both materials adhering to the coating surface.

After that, the total masses of 316L and Fe particles impacting the coating surface are calculated as follows:

$$M_A = n_A m_A \tag{2.5}$$

$$M_B = n_B m_B \tag{2.6}$$

The relationship between the total masses of 316L and Fe particles impacting in the surfaces is described by the Equations (2.7) and (2.8) being this equal to their weight fractions.

$$f_A = \frac{M_A}{M_A + M_B} \tag{2.7}$$

$$f_B = \frac{M_B}{M_A + M_B} = (1 - f_A) \tag{2.8}$$

Then the overall DE is described by the Equation (2.9).

$$DE = \frac{dM_A + dM_B}{M_A + M_B} \tag{2.9}$$

Then by substituting Equations (2.3)-(2.8) into Equation (2.9) the DE can be rewritten as:

$$DE = f_B \times BR_B + (1 - f_B) \times BR_A \tag{2.10}$$

In Figure 2.2, the DE obtained with the BRST model is plotted alongside the experimental data. It can be seen that BRST is much more accurate, resulting in a good prediction of the DE behavior, even though it slightly underestimates it.

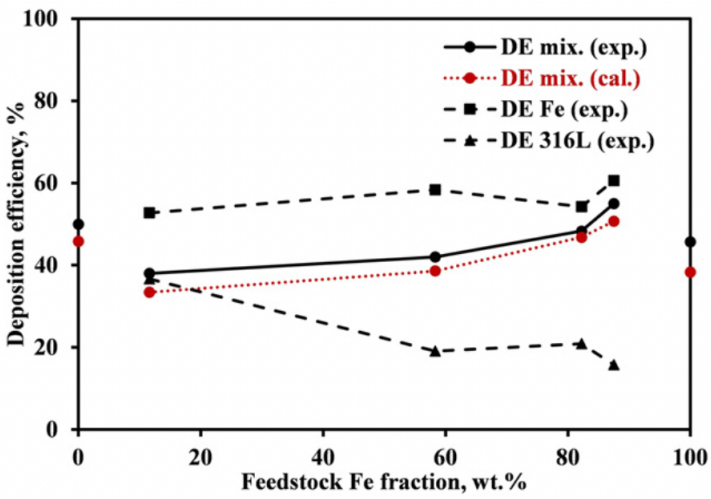


Figure 2.2: Comparison between DE obtained experimentally and DE calculated with the BRST [11].

This model presents a considerable advantage in terms of accuracy compared to the previously mentioned ROM. This improvement is mainly achieved by considering the interaction between the different powders. However, the disadvantage of this model is that these interactions were determined through splat tests, which required a considerable amount of resources.

2.1.3. Semi-empirical probability model (SEP)

As discussed by A. Sova et al. [12], modeling multi-component CS coatings is not an easy task, and the properties of both materials are crucial in order to determine the results in terms of composition and DE. Due to this, they proposed to use a metal mixture of type "soft" metal - "hard" metal. In this kind of mixture, since the adhesion of the particles is related to their mechanical properties, two possible scenarios may arise, as shown in Figure 2.3. If we assume that the spray parameters are optimal for the deposition of "soft" metal but sub-optimal for the "hard" ones, then the impact energy of the soft particles is enough to adhere to both soft materials and the substrate as well. While the impact energy of the hard particles, due to the previously mentioned sub-optimal conditions, is enough to adhere to the previously deposited soft material, as shown in Scenario 1 in Figure 2.3, as they will adhere mainly due to mechanical embedding. The impact energy, though, is not enough to adhere to the previously deposited hard particles, generating a rebound, as shown in Scenario 2 in Figure 2.3.

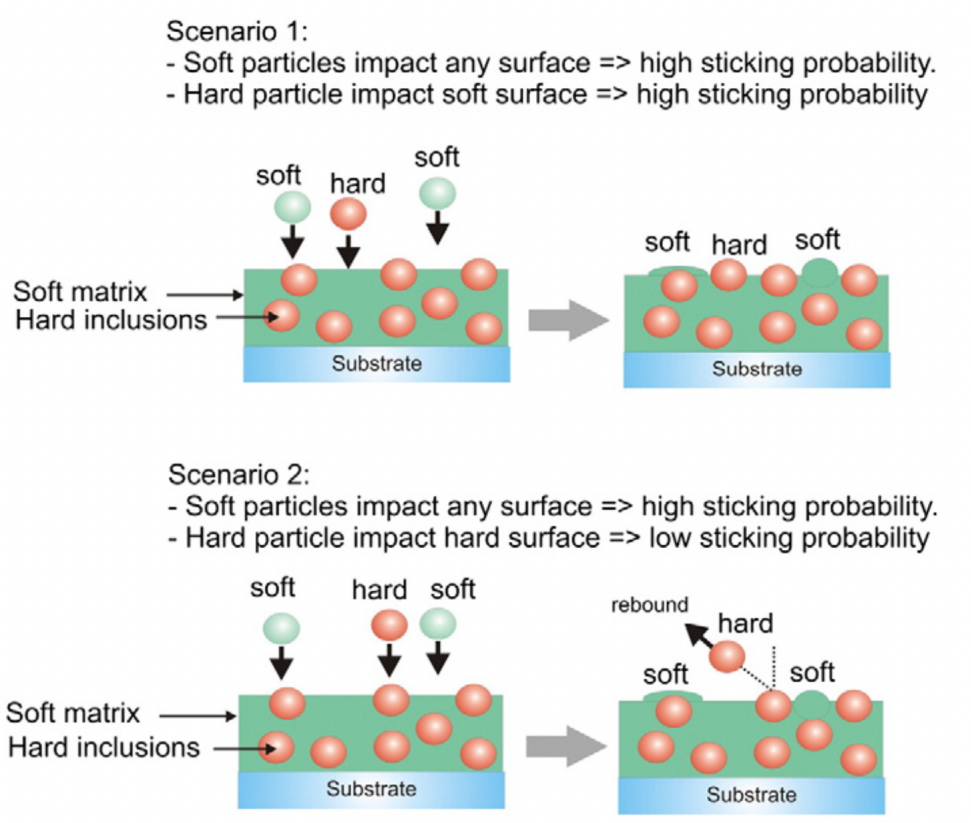


Figure 2.3: Impact scenarios during CS of two-component powder mixture of "soft" and "hard" metals [12].

A. Sova et al.[12] stated that, in this case, the DE values for both materials are different, where the soft materials present a higher DE, and it is also independent of the material they are interacting with. Whereas the DE of the hard particles has a dependence on the particles it is interacting with. Because of this a model that considers the interaction between the different types of materials and their compositions along the thickness was developed by E. Lapushkina and A. Sova [13], this model works under the following assumptions:

- A mixture contains hard and soft powders
- Particles of both powders are spherical
- Particles of hard and soft powders are well mixed in the gas flow
- A continuous layer is being formed, and the first layer of the coating has already formed.

First the model considers that a during a short time a total number of dn particles falls

onto a unit area. From which $(1-c)dn$ are the particles of hard metal and cdn the particles of soft metal. Being c the particle number concentration which is calculated following the Equation (2.11).

$$c = \frac{f_{\text{soft}}\rho_{\text{hard}}\left(\frac{4}{3}d_{\text{hard}}^3\right)}{f_{\text{soft}}\rho_{\text{hard}}\left(\frac{4}{3}d_{\text{hard}}^3\right) + f_{\text{hard}}\rho_{\text{soft}}\left(\frac{4}{3}d_{\text{soft}}^3\right)} \tag{2.11}$$

Where c is the particle number concentration, f_{soft} and f_{hard} are the weight fraction of both soft and hard materials, ρ_{soft} and ρ_{hard} are the densities, and d_{soft} and d_{hard} are the particle diameters.

Then the contact areas needs to be calculated as well:

$$PS_{soft} = Kd_{soft}^2 \tag{2.12}$$

$$PS_{hard} = Kd_{hard}^2 \tag{2.13}$$

Where PS_{soft} and PS_{hard} are the contact areas, and K is a proportionality coefficient. This coefficient represents how the particle deformation is taken into account.

Then, in order to implement the model, the different adhesion probabilities need to be determined experimentally: first, those related to the soft particles $p_{soft-soft}$ and $p_{soft-hard}$ and similarly for the hard particles $p_{hard-hard}$ and $p_{hard-soft}$. With this, the changing relative surface area covered by the soft metal (ds_{soft}) can be calculated using Equation (2.14).

$$ds_{\text{soft}} = -\rho_{\text{hard-soft}}(1-c)s_{\text{soft}}P_{\text{hard}}dn + \rho_{\text{soft-hard}}cs_{\text{hard}}P_{\text{soft}}dn \tag{2.14}$$

The relative surface area covered by both materials follow the relationship established in the Equation (2.15).

$$s_{soft} + s_{hard} = 1 \tag{2.15}$$

Then the total mass of particles impacting the surface(dM_p) can be calculated as expressed in the Equation (2.16)

$$dM_p = dM_{phard} + dM_{psoft} = (1-c)m_{hard}dn + cm_{soft}dn \tag{2.16}$$

Where M_{phard} and M_{psoft} are the total mass of hard and soft particles impacting a surface, and m_{hard} and m_{soft} represent the mass of a single hard or soft particle, respectively.

Then the total increase in the mass of the coating (dM_c) is described by the Equation (2.17).

$$dM_c = dM_{soft} + dM_{hard} \tag{2.17}$$

Where M_{soft} and M_{hard} represent the mass of both soft and hard particles in the coating and the increment of them both is obtained following Equations (2.18) and (2.19).

$$dM_{soft} = c\left(p_{soft}s_{soft} + p_{soft}s_{hard}\right)m_{soft}dn \tag{2.18}$$

$$dM_{hard} = (1-c)\left(p_{hard-soft}s_{soft} + p_{hard-hard}s_{hard}\right)m_{hard}dn \tag{2.19}$$

Then the deposition efficiencies of both hard and soft powders can be calculated following the Equation (2.20) and (2.21).

$$DE_{soft} = \frac{dM_{soft}}{dM_{psoft}} \tag{2.20}$$

$$DE_{hard} = \frac{dM_{hard}}{dM_{phard}} \tag{2.21}$$

In order to validate this model, E. Lapushkina and A. Sova [13] performed experimental tests using a metal mixture of pure copper (Cu) as the soft component, while the hard one was cermet (Cr_2C_3NiCr) at two different gas temperatures 350 ºC and 450 ºC.

The results are shown in Figures 2.4 and 2.5. The first figure displays the composition calculated by the model and compares it with the experimentally obtained data for the two previously mentioned temperatures. The second figure shows the deposition efficiencies, comparing the theoretical values with the experimental data.

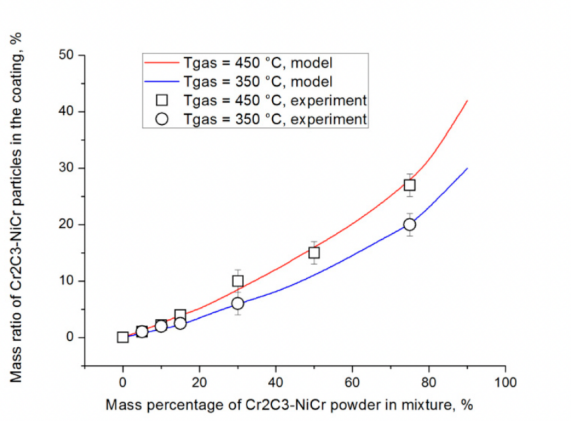


Figure 2.4: Percentage of cermet in the coating compared with the weight fraction initially sprayed [13].

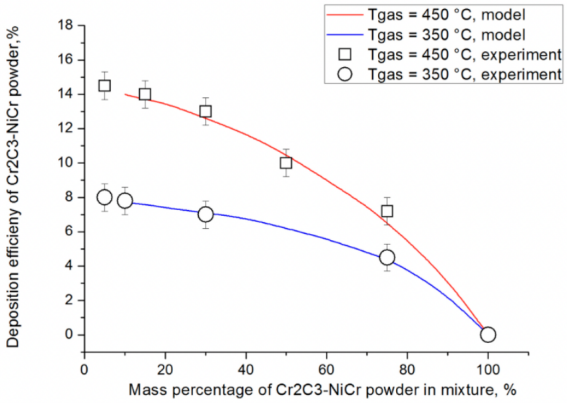


Figure 2.5: DE of cermet in the coating compared with the weight fraction initially sprayed [13].

2.1.4. FEM assisted DE predictive model

A. Ardeshiri Lordejani et al. [14] improved the SEP model that allows consideration of substrate interaction in the process, allowing the calculation of the composition near the substrate. Another improvement is the way the splat areas are taken into account. In the SEP model, they were defined as detailed in Equations (2.12) and (2.13). However, the fact that the splat areas depend on a single proportionality coefficient neglects the effect of particle morphology and material properties, assuming that all particles deform in the same way. This new model includes finite element modeling (FEM), where particle impact simulations are used to improve accuracy in determining the different splat areas.

Thus, the model estimates the composition along the thickness by considering the interaction between the different materials and the effect of the composition of the layer deposited previously on the new layer. To do so, the following assumptions are considered.

- Particles are well-mixed in the gas flow
- The thickness of each deposited layer is assumed to be constant regardless of the layer composition
- Spherical particles are assumed
- The composite can be approximated as a sequence of layers
- Each layer composition is a function of the previous one
- Average-size particles are going to be assumed

To do so, first the layer thickness needs to be calculated by assuming volume conservation. The shape of the deformed particle is considered an imaginary cylinder with the same volume as the particle (V_{avg}). Its diameter is the largest one found after deformation, known as the splat diameter (w). The height of each layer in the case of a single component can calculated as follows:

$$h = \frac{4V_{avg}}{\pi w^2} \tag{2.22}$$

If we have a multi-component coating with N constituents, the layer height can be calculated using Equation (2.23), where h_i is the calculated height for constituent i and f_i is its weight fraction.

$$h = f_A \times h_A + f_B \times h_B + \cdots + f_N \times h_N \tag{2.23}$$

This model can be used for multiple components, but for the sake of simplicity, the following equations consider a bimetallic coating formed by materials A and B. The first step is to calculate the number concentration of powder particles (c_A and c_B), as described in Equations (2.24) and (2.25).

$$c_A = \frac{f_A \rho_B V_B}{f_A \rho_B V_B + f_B \rho_A V_A} \tag{2.24}$$

$$c_B = \frac{f_B \rho_A V_A}{f_A \rho_B V_B + f_B \rho_A V_A} = 1 - c_A \tag{2.25}$$

Where V_A and V_B are the undeformed particle volumes, and ρ_A and ρ_B represent the apparent density of each material.

After calculating the number concentration of each powder, the relative splat areas (SA) will be calculated for the impact of both materials on material A (SA_{A-A} and SA_{B-A}), on material B (SA_{A-B} and SA_{B-B}), and on the substrate (SA_{A-s} and SA_{B-s}), as described in Equations (2.26) and (2.27). Here, A_{A-A} and A_{B-A} represent the splat areas of an average-size particle, determined via FEM.

$$S_{A-A} = \frac{A_{A-A}}{A_{A-A} + A_{B-A}} \tag{2.26}$$

$$S_{B-A} = \frac{A_{B-A}}{A_{A-A} + A_{B-A}} = 1 - S_{A-A} \tag{2.27}$$

Then, in order to calculate the relative areas (s), the adhesion probabilities are required. These will be obtained following the same procedure described in Subsection 2.1.3. Additionally, the adhesion probabilities of both materials on the substrate will also be calculated. Finally, the adhesion probabilities are as follows:

- p_{A-A} is the adhesion probability of A on A (DE of A on A)
- p_{A-B} is the adhesion probability of A on B (DE of A on B)
- p_{B-A} is the adhesion probability of B on A (DE of B on A)
- p_{B-B} is the adhesion probability of B on B (DE of B on B)
- p_{A-S} is the adhesion probability of A on substrate (DE of A on substrate)
- p_{B-S} is the adhesion probability of B on substrate (DE of B on substrate)

The layer calculations will consider the effect of the previous layer, and an iterative process is required to determine the composition of each new layer. Three parameters, all related to the area (considered as a unit area), are calculated during this iterative process. The first is the ideal layer area (ILA), which represents the theoretical amount of powder needed to cover the entire area. Next is the layer area (LA), the actual covered area, which accounts for the adhesion probabilities, resulting in a value lower than the ideal layer area. Finally, the remaining layer area (RLA) is the area not covered by LA. This process is repeated through several iterations until full coverage is achieved (i.e., RLA = 0). This iterative process is illustrated in Figure 2.6, where the three previously mentioned parameters are depicted.

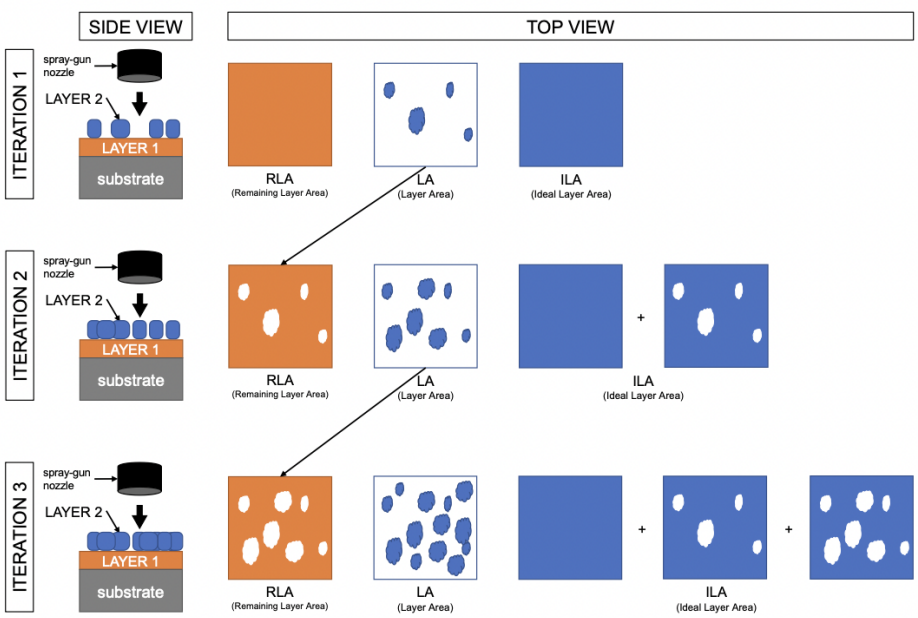


Figure 2.6: Schematic of the iterative process employed to calculate the layer compositions [14].

This model allows us to successfully predict not only the DE for the process but also the composition of each layer. To validate their model, A. Ardeshiri Lordejani et al. [14] performed experimental tests on bimetallic CS coatings using pure zinc powder and pure aluminum powder, sprayed with two different Al-Zn compositions. The first was 60% Al–40% Zn, and the second was 40% Al–60% Zn.

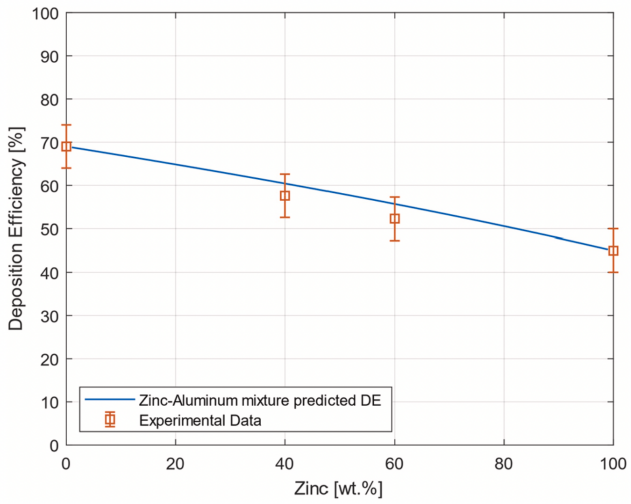


Figure 2.7: Comparison between the DE of the different samples and that calculated with the model [14].

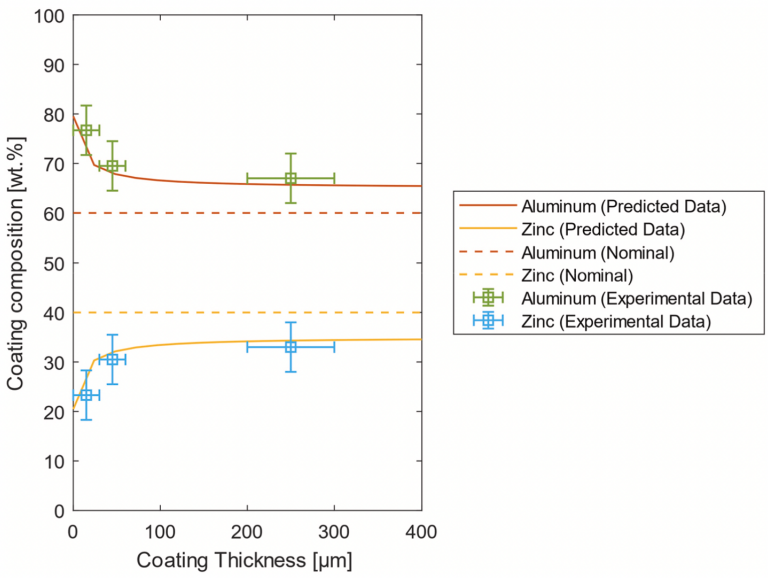


Figure 2.8: Comparison between the experimentally obtained composition for the 60% Al–40% Zn sample and the composition predicted by the model [14].

As shown in Figure 2.7, the model allows us to accurately predict the DE for different feedstocks. Meanwhile, Figure 2.8 illustrates that the FEM-assisted predictive model can correctly estimate the composition along the coating thickness. It also demonstrates that this model effectively considers the substrate effect, revealing that in the early stages of coating formation, the composition may differ from that at steady state.

2.2. Advantages and limitations of the models

As mentioned in Section 2.1, different researchers have approached the modeling of the DE in a cold spray process in various ways, considering different experimental tests and numerical simulations, and making different assumptions for each model. All of these assumptions and considerations come with some advantages and limitations, which will be discussed in this section.

Rule of mixture (ROM)

The ROM model, as discussed in Subsection 2.1.1, is a very simple model that calculates the DE as the average of the DEs of the two powders, and to do so, only two experimental tests need to be performed. The simplicity and minimal requirement of experimental tests could be considered a strength, but this model did not present good results in predicting the behavior of the mixture DE, which is a major drawback. This can be explained by the fact that, by being so simple, the model neglects the interaction between the two different

powders, which turns out to be an essential consideration in the following DE predictive models.

Bond ratio splat test based model (BRST)

In the BRST model proposed by X. Chu et al.[11] presents higher accuracy in predicting the DE of the mixture, thanks to the introduction of bond ratios. This addition not only clarifies the interaction between the different materials but also leads to good performance in terms of accuracy. Its major drawback is the large number of experimental tests required and the processing of these tests using the counting method described in their work. For a bi-metallic coating, the number of tests depends on the number of different feedstocks, requiring two experimental tests for each composition. In their research, they analyzed six different compositions, so 12 experimental tests were needed to apply the model. This could be considered its major limitation.

Semi-empirical probability model(SEP)

The SEP model, discussed previously in Subsection 2.1.3, presents good performance by considering the interaction between different powders. However, the model has its limitations. First, it neglects the interaction between the powders and the substrate by assuming that the first layer has already been formed. Additionally, the way this model accounts for particle deformation—by introducing a proportionality coefficient, as shown in Equations (2.12) and (2.13)—assumes that all particles deform in the same way, regardless of the material they impact. Lastly, the assumption of steady-state deposition implies that the effect of the previous layer is not considered.

FEM assisted DE predictive model

The model presented by A. Ardeshiri Lordejani et al. [14] demonstrates strong performance in predicting composition and DE. Additionally, the calculation of composition near the substrate is an important element, as it allows for a better understanding of the transient behavior in coating formation. Although the number of required experimental tests is higher compared to the SEP model, the inclusion of substrate-powder interaction justifies this increase, as it provides deeper insight into the coating formation process.

One limitation of the model is the assumption that all particles are of the same size throughout the entire coating. In reality, this is not the case, as producing powders with perfectly uniform particle size is not feasible.

3 | Particle impact modeling simulation

3.1. Different methods for particle impact modeling

The interaction between the substrate and the particle in a CS process is very complex to analyze, as it is a highly transient, nonlinear, and dynamic phenomenon. Along with the extremely short impact time, this makes it very difficult to study experimentally. Thus, numerical simulations become crucial, which allows to properly model plastic deformations, temperature changes, and to analyze the transient behavior itself, which would otherwise be difficult to examine [15, 16].

There are different finite element (FE) formulations that have been used over time, ranging from conventional FE models such as the Lagrangian method to mesh-free methods like Smoothed Particle Hydrodynamics (SPH), and some hybrid solutions like the Coupled Eulerian-Lagrangian (CEL) or the Arbitrary Lagrangian-Eulerian (ALE) [27].

Understanding the interaction between particles and substrate is crucial for DE predictive models. As mentioned in Chapter 2, some models account for this interaction indirectly (e.g., the BRST), while others, such as the FEM-assisted DE predictive model, require input data like the deformed radius, which must be obtained using FEM. Consequently, the following models have been proposed over time.

3.1.1. Lagrangian method

In the Lagrangian approach, the movement of the continuum is a function of the material coordinates and time. This model is usually applied to solid structures, and the nodes of the mesh in this kind of simulation move alongside the material. This allows differentiation of the interface between materials in the case of particle impact simulation [16].

According to several studies, it has been proven that the Lagrangian method can provide good results in terms of deformation behavior in CS particle impact simulation [15]. In

order to obtain the strains and temperatures at the contact interface, the mesh size plays a crucial role. Thus, to achieve high-precision results, a very fine mesh must be used [28–30].

In their research, Shuo Yin et al. [15] performed particle impact simulations for a copper particle and confirmed that the mesh size plays an important role at the contact interface. The mesh size was changed from 2.0 μm to 0.5 μm, and as shown in Figure 3.1, it can be observed that for a coarser mesh, the jetting effect is not so prominent as for the finer ones.

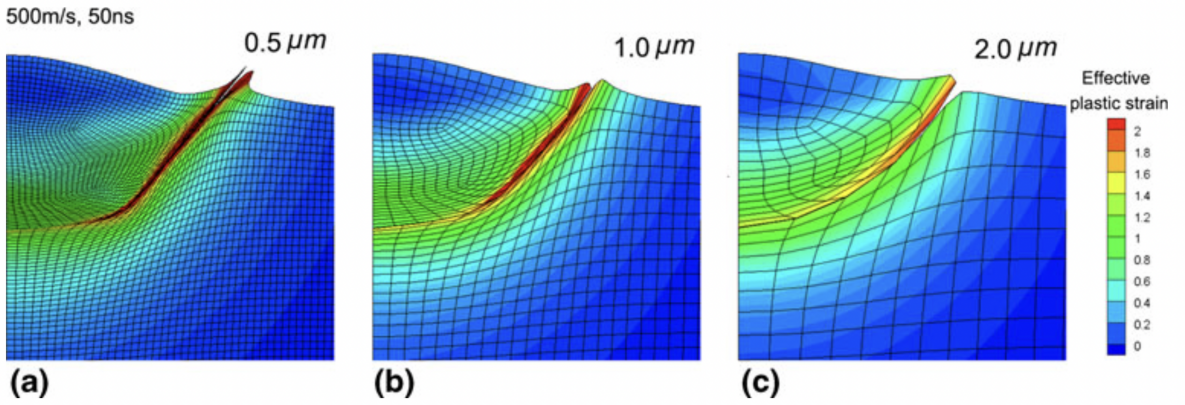


Figure 3.1: Contact interface of the copper particles for different mesh sizes (a)0.5μm, (b)1.5μm and (c)2.0μm [15].

Jing Xie et al. [16] performed research on a combination of aluminum and copper. Large distortions were observed, making it impossible to complete the simulation. Due to this mesh distortion, unrealistic behaviors were also obtained in terms of both plastic strain and temperature.

3.1.2. Arbitrary Lagrangian-Eulerian (ALE) method

ALE is a numerical approach that combines both the Lagrangian and Eulerian models, enabling the grid to be redefined continuously. ALE can be used not only to model solids but also fluids. This method allows maintaining a high-quality mesh even under large deformations [16].

This approach is highly efficient for performing large displacement simulations, and the computational costs can be further reduced by properly defining the domains of the adaptive mesh [31].

Jing Xie et al.[16] achieved proper mesh quality in their research but observed some per-

formance issues with this model. The first issue is related to bonding problems, as shown in Figure 3.2, where the particle rebounds. Additionally, the jetting effect is smoother compared to the Lagrangian model, which exhibits sharper edges. The main concern, however, is that the temperature and plastic equivalent strain over time reach a high peak and then decrease to a plateau, which is unrealistic and occurs due to interpolation errors caused by the adaptive meshing algorithm during the remapping phase.

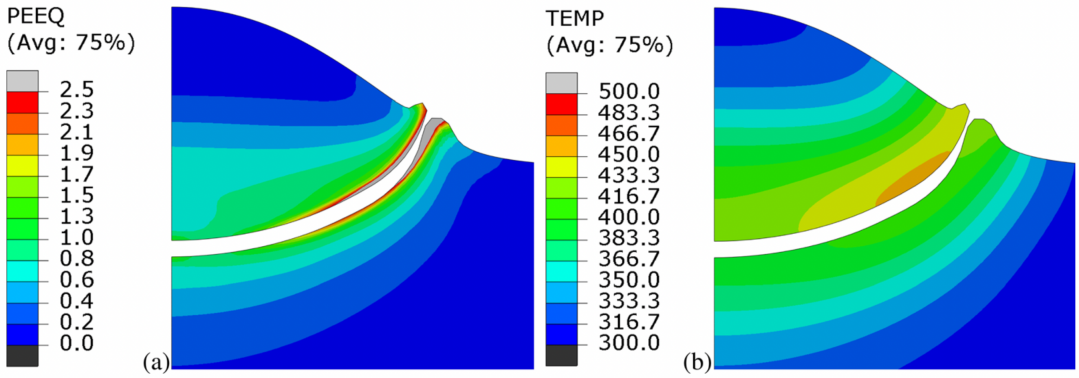


Figure 3.2: (a) Equivalent plastic strain and (b) temperature of an Aluminum particle impacting onto an Aluminum substrate[16].

3.1.3. Smoothed particle hydrodynamics (SPH) method

The SPH numerical approach belongs to the mesh-free methods, where the nodes are not defined within the domain as in traditional FE methods. In this approach, the modeled body is represented by a series of points, called pseudo-particles or particles in smoothed particle hydrodynamics [31].

This model has proven to be suitable for predicting the critical impact velocity in particle impact modeling [32, 33]. Being a meshless method, SPH performs well in multi-particle impact simulations, providing highly accurate results for interface contact [34].

During their research, Jing Xie et al.[16] performed FE particle impact simulations for different combinations of aluminum and copper and compared SPH with other models such as ALE and Lagrangian. The obtained results for the SPH approach are shown in Figure 3.3. No material jetting was observed, and the particle penetrated deeper into the substrate compared to the other simulations performed. The equivalent plastic strain (PEEQ) in the substrate also exhibited an unrealistic behavior, continuously increasing over time.

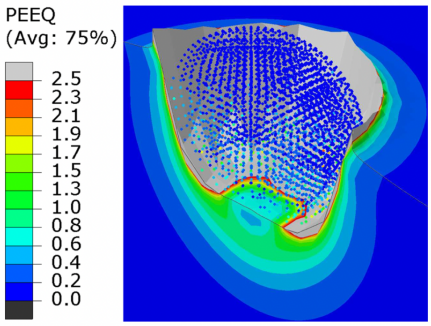


Figure 3.3: Equivalent plastic strain for Al on Al impact simulation at 700 mm/s using SPH method [16].

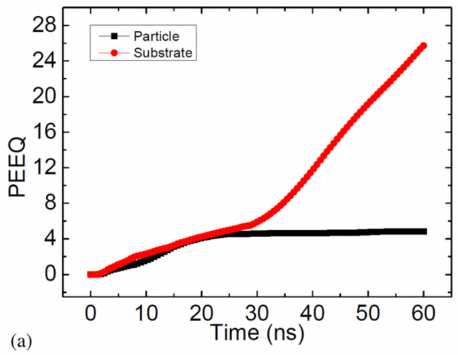


Figure 3.4: Time history of the equivalent plastic strain for Al on Al impact simulation at 700 mm/s using SPH method[16]

3.1.4. Coupled Eulerian-Lagrangian (CEL) method

The Coupled Eulerian-Lagrangian (CEL) approach allows the interaction of Lagrangian elements through Eulerian-Lagrangian contact. In this approach, the material is tracked as a flow moving through the mesh by calculating its Eulerian volume fraction in each element. This method enables a single element to contain more than one material at a time, and if the sum of these materials does not fully occupy the element, the remaining portion is filled with void material, which has neither mass nor strength. CEL performs particularly well in solving complex fluid-structure interaction problems, including large displacements and large strains, within a single simulation [16].

Jing Xie et al. [16] realized during their research that the performance of the CEL method was particularly good for particle impact simulation due to its fluid-like behavior upon impact. CEL allows for a significant reduction in mesh distortion and unrealistic deformed shapes. Additionally, the jetting effect is obtained, as shown in Figure 3.5.

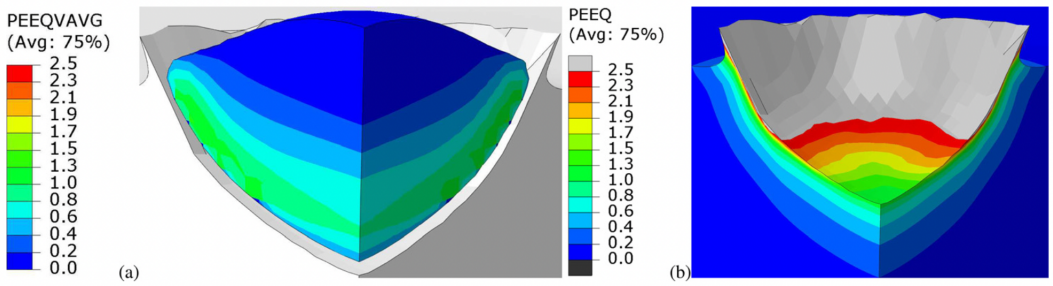


Figure 3.5: (a) Equivalent plastic strain in the Al particle and (b) equivalent plastic strain in the Al substrate at 700 mm/s using CEL method [16].

3.2. Impact simulation set up

The different particle impact simulations will be performed using ABAQUS/CAE 2024 software. This section describes the setup details for the FE simulations. The objective of these simulations is to analyze the interaction between the particle and the substrate for different material combinations and particle diameters, ultimately obtaining the splat radius, which will later be used in the model described in Chapter 4. The CEL approach has been selected as the FE method due to the significant plastic deformations that can occur in this material combination, making it a suitable approach for this study.

Material set up

For this research, four different materials will be considered: pure aluminum and iron powders, and the substrate, which will be aluminum alloy Al6082 and pure iron ARMCO. For the model, the material properties related to elastic behavior, plastic behavior, and thermal properties were introduced, filling the following sections:

- Elastic properties
- Plastic rate dependent (Johnson Cook model)
- Density
- Expansion coefficient
- Specific heat
- Conductivity

For the material properties, since both the iron powder and the iron substrate are pure iron, they will be assumed to be the same material, as they share the same material properties and Johnson-Cook parameters, which will be further explained in this section. The material properties for aluminum powder are indicated in Table 3.1. The information about the material properties for pure aluminum powder was obtained from the literature, specifically from Peter C. King et al. [35], Bae Gyuyeol et al. [36], T. Hussain et al. [37], and Jing Xie et al. [16]. Meanwhile, the material properties for the aluminum alloy substrate were extracted from the Granta EduPack 2021 R2 database [38]. For pure iron, the material properties were obtained from the research conducted by Sara Bagherifard et al. [39] and Gordon R. Johnson et al. [40].

Material Properties	Aluminum (Powder)	Al6082T6	Pure iron
Density [t/mm^3]	2.698E-09	2.70E-09	7.87E-09
Expansion Coef. [1/K]	2.31E-05	2.31E-05	6.50E-06
Conductivity [W/mK]	237.2	172	971
Specific Heat [Nmm/tK]	89820000	90000000	44000000
Young's Modulus [MPa]	69000	72000	200000
Poisson Ratio [-]	0.3	0.3	0.33

Table 3.1: Material Properties of Aluminum and Iron

In order to model the plastic behavior of the material, the Johnson-Cook (JC) material model is used. As described by V. K. Reddy Sirigiri et al. [41], the JC model is employed to analyze the stress-strain behavior of materials undergoing large deformations and high strain rates. This model is widely used by engineers to predict material flow behavior through the flow stress equation, which is expressed in Equation (3.1).

$$\sigma = (A + B\epsilon^n)\,(1 + C\ln\dot{\epsilon}^*)\,(1 - T^*)^m \tag{3.1}$$

Where σ is the equivalent stress and ε the equivalent plastic strain. The JC equation material constants are: A, the yield stress of the material in standard conditions; B, the strain hardening coefficient; n, the strain hardening exponent; C, the strengthening factor of strain rate; and m, the thermal softening coefficient. The equation is divided into three parts, the first one is the strain hardening effect, the second considers the strain rate strengthening effect and temperature effect.

$$\dot{\epsilon}^* = \frac{\dot{\epsilon}}{\dot{\epsilon}_{ref}} \tag{3.2}$$

$$T^* = \frac{T - T_{ref}}{T_m - T_{ref}} \tag{3.3}$$

Where $\dot{\varepsilon}^*$ represents the dimensionless strain rate, T^* corresponds to the homologous temperature, T_m is the melting temperature, T is the deformation temperature, $\dot{\varepsilon}_{ref}$ is the reference strain rate, and T_{ref} is the reference deformation temperature.

To determine the strain hardening variable B and the strain hardening factor n the affect of both strain rate strength and thermal softening factor have a small effect leading to

the Equation 3.4

$$\sigma = (A + B\varepsilon^n) \tag{3.4}$$

Equation 3.4 is modified by applying the natural logarithm to both sides, as shown in Equation 3.5. From this equation, a linear relationship between the parameters B and n can be obtained by performing a linear regression.

For the constant C instead, the thermal softening is negligible knowing this, the flow stress equation can be rearranged, obtaing the Equation

$$\ln(\sigma - A) = n \ln \epsilon + \ln B \tag{3.5}$$

For the constant C, the thermal softening is considered negligible. Knowing this, the flow stress equation can be rearranged, obtaining Equation (3.6). By substituting the previously obtained values, a linear fitting can be applied to properly determine the constant C.

$$\frac{\sigma}{A + B\epsilon^n} = (1 + C \ln \dot{\epsilon}^*) \tag{3.6}$$

The JC parameters for Al6082-T6 were obtained from S.P.F.C. Jaspers [42] and are indicated in Table 3.2. The parameters for pure iron were determined in the research conducted by Sara Bagherifard et al. [39] and also by Gordon R. Johnson et al. [40].

Johnson-Cook	**Al (Powder)**	**Al6082-T6**	**Fe (Powder)**
A [MPa]	148.4	428.5	175
B [MPa]	345.5	327.7	380
n [-]	0.183	1.008	0.32
m [-]	0.895	1.31	0.55
T_{melt} [K]	916	855	1811
T_{trans} [K]	293	293	293
C [-]	0.001	0.00747	0.26573
$\dot{\epsilon}_{ref}$	1	1	1

Table 3.2: Johnson-Cook parameters for Aluminum, Al6082-T6, Iron, and Pure Iron ARMCO

Geometry and boundary conditions (BC)

For the geometry, a 3D CEL approach is used, where only a quarter of the particle is modeled, applying the respective symmetries. Regarding the substrate, it is modeled as a quarter of a cylinder.

For these geometries, two possible situations need to be considered. The first occurs when the particle undergoes significantly larger plastic deformations compared to the substrate. In this case, three main components must be defined, as shown in Figure 3.6: the particle, the substrate, and the void, which corresponds to the Eulerian domain.

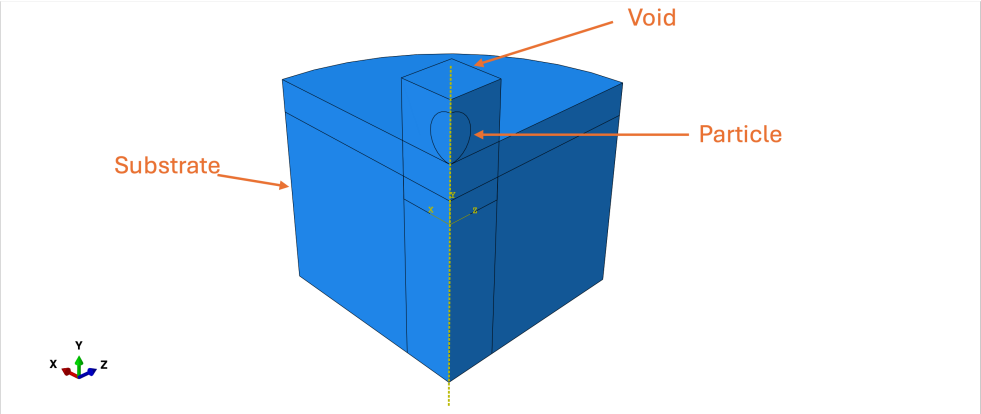


Figure 3.6: Assembly used for the case where particle suffers larger plastic deformations

If the substrate experiences significantly larger plastic deformation compared to the particle, the model shown in Figure 3.7 is used. In this case, the components are limited to the particle, which is no longer part of the Eulerian domain, and the substrate, which is now included in the Eulerian domain.

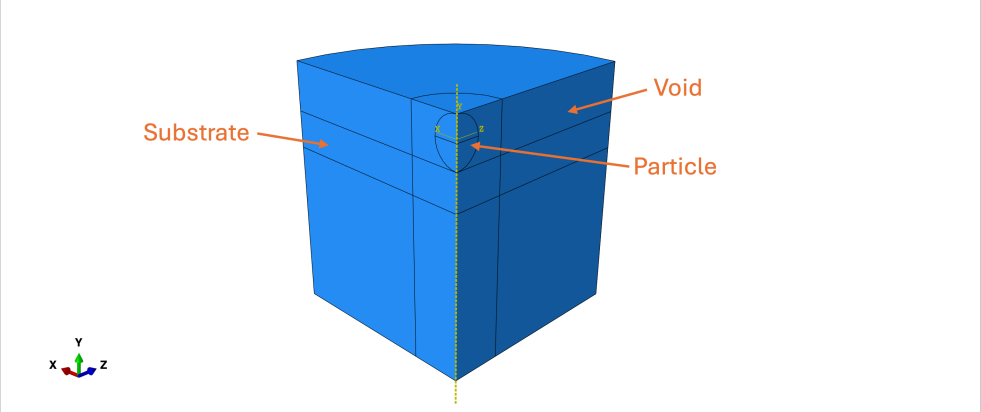


Figure 3.7: Assembly used for the case where substrate suffers larger plastic deformations

The dimensions of this component are all a function of the particle diameter, leading to different scenarios depending on the extent of plastic deformation in both the particle and the substrate. Regarding the substrate dimensions, three scenarios are considered, as shown in Figure 3.8. Cases (a) and (b) correspond to situations where the particle undergoes greater plastic deformation compared to the substrate, and in these cases, the particle is part of the Eulerian domain. Case (b) represents a situation where the particle deformation is particularly large. The third scenario, case (c), corresponds to a situation where the particle exhibits very low plastic deformation, resulting in significant deformation of the substrate.

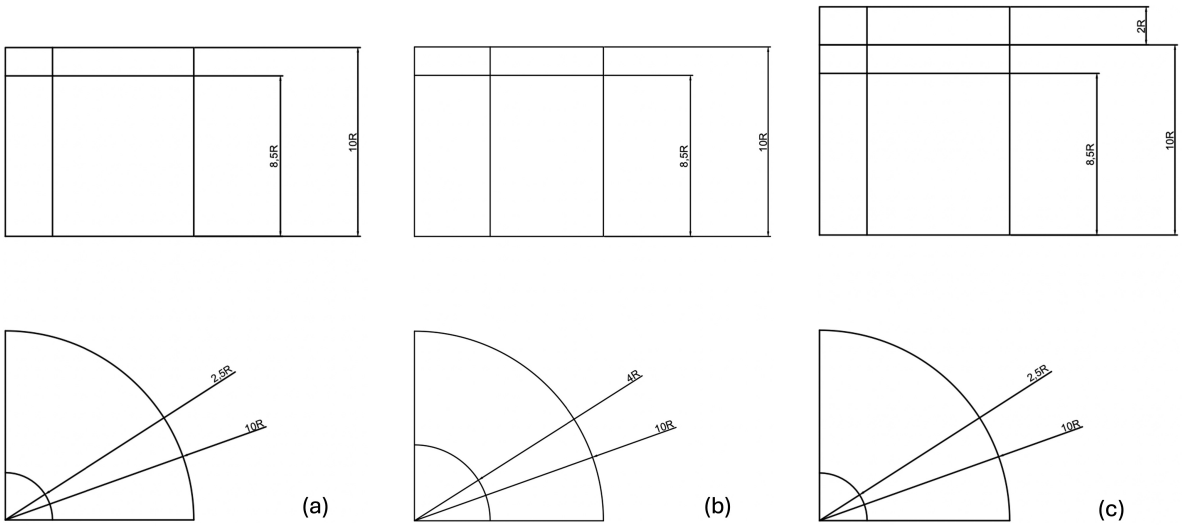


Figure 3.8: Substrate dimensions for different scenarios depending on the particle's plastic deformation: (a) large plastic deformation in the particle, (b) very large plastic deformation in the particle, and (c) large plastic deformation in the substrate.

A parallelepiped with the dimensions indicated in Figure 3.9 is used, with the particle initially positioned as shown. Two different scenarios are considered: case (a) represents a particle with large deformations relative to the substrate, while case (b) corresponds to a particle with very large plastic deformation.

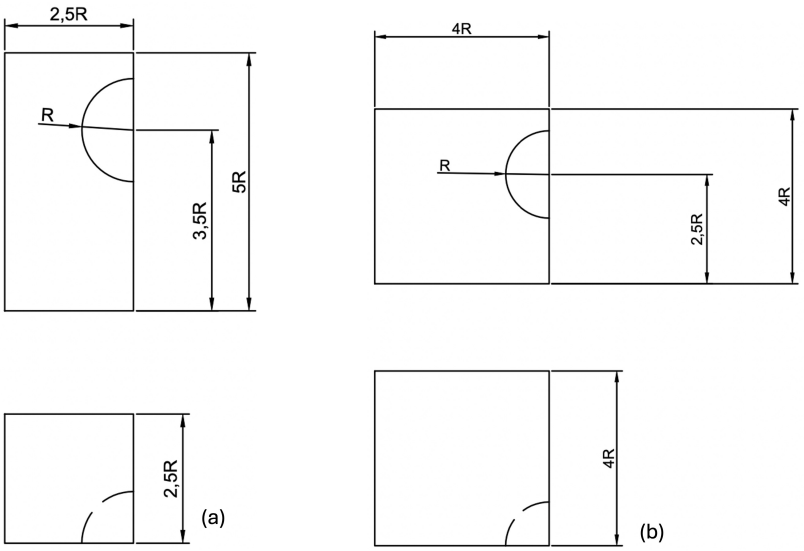


Figure 3.9: Void dimensions for different scenarios depending on the particle's plastic deformation: (a) large plastic deformation in the particle, and (b) very large plastic deformation in the particle.

For the boundary conditions (BC), since a CEL approach is used, the volume fraction needs to be defined to distinguish between material and void regions. In the case of large plastic deformation in the particle, this volume fraction is applied to the void region, and a node region must be defined at the initial location of the particle. For the other scenario, where the substrate undergoes larger plastic deformation, the volume fraction is defined in the substrate, with its upper part designated as void.

The substrate must be constrained by applying all relevant symmetries and boundary conditions, as shown in Figure 3.10. In the YZ plane, an X symmetry condition is applied ($U1 = UR2 = UR3 = 0$), while in the XY plane, a Z symmetry condition is enforced ($U3 = UR1 = UR3 = 0$). The remaining free edge is also constrained with ($U1 = U3 = UR1 = UR3 = 0$), and finally, the lower part of the substrate is fully fixed using an encastre boundary condition, restricting all displacements and rotations.

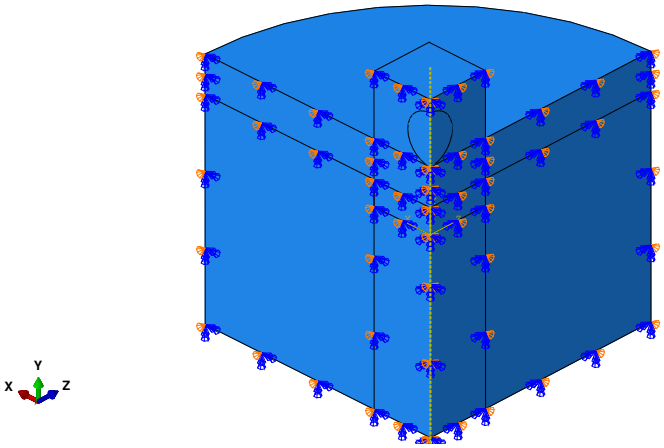


Figure 3.10: BC applied to the substrate

Beside from that, also the predifined fields needs to be introduced, considering the particle's impact velocity and temperature, which are a function of the particle diameter and also the substrate temparature needs to be defined which for our case is equal to 298 K. Beside from that in the case of the Eulerian domain the material needs to be assigned as well.

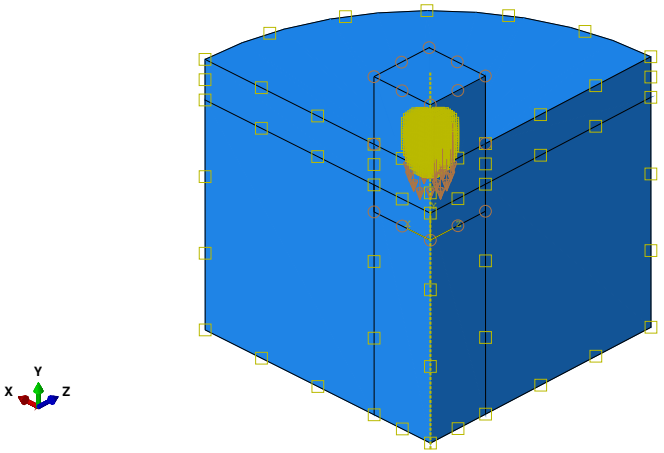


Figure 3.11: Predifined fields applied to the assembly

Mesh

For the meshing of the assembly, three different components are meshed. The first one is the "void" region, which is assigned a structured mesh with a mesh size of $1.5\mu m$. The element type used is EC3D8R: an 8-node linear Eulerian brick with reduced integration and hourglass control.

The particle is meshed only in the case where large plastic deformations occur in the substrate. For this case, a structured mesh with a mesh size of $1.5\mu m$ is also used. The element type corresponds to C3D8T: an 8-node thermally coupled brick with trilinear displacement and temperature.

For the substrate, a more complex meshing strategy is applied, as shown in Figure 3.12. Following the defined partitions, a finer mesh is applied in the central region with a mesh size of $1.5\mu m$, while for the rest of the edges, a single bias is applied, transitioning from $1.5\mu m$ to $25\mu m$. This mesh is obtained using a combination of structured and swept meshing techniques.

The element type assigned to the substrate depends on the deformation characteristics. When small plastic strains are present, the element type used is C3D8RT: an 8-node thermally coupled brick with trilinear displacement and temperature, reduced integration, and hourglass control. For cases involving large strains in the substrate, the element type is EC3D8R: an 8-node linear Eulerian brick with reduced integration and hourglass control.

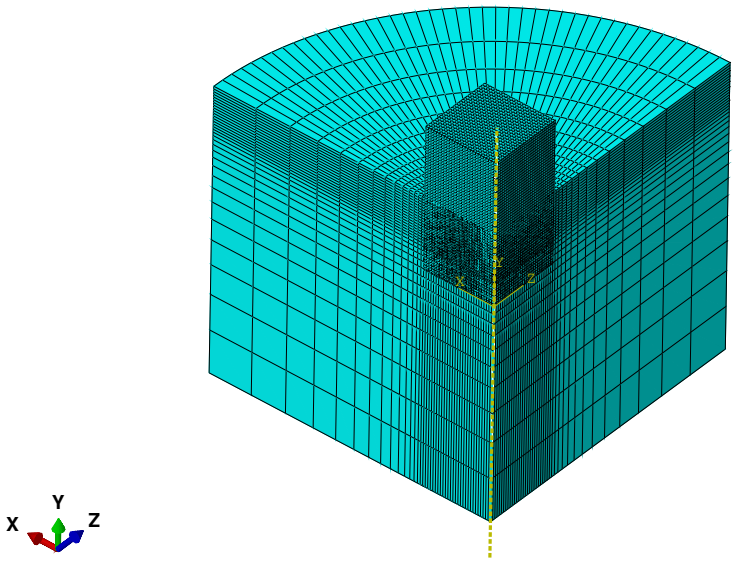


Figure 3.12: "Void" and substrate mesh for a 3D CEL model

4 | Experimental test and model development

4.1. Powder characterization

For the bimetallic deposits, two different materials were used: aluminum powder supplied by Toyal Group and iron powder supplied by Pometon, where both were produced by gas atomization. The aluminum powder is a high-purity powder (Al weight content >99.998%) with an average particle diameter of 32.1μm. The iron powder has a high purity as well (Fe weight content >99.64%) and an average particle diameter of 31.53μm.

To analyze the particle size distribution (PSD), these powders were characterized using a Mastersizer 2000 machine from Malvern PANalytical Ltd., UK. Leading to the results shown in Figure 4.1. Additionally, the apparent density of the aluminum powder was measured as 0.0014 g/mm^3, while for the iron powder, it was found to be 0.00365 g/mm^3.

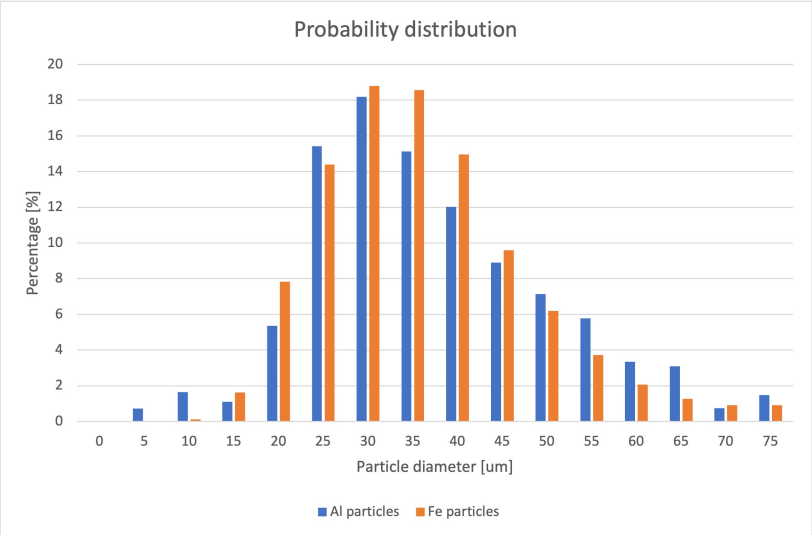


Figure 4.1: Probability distribution for both Al and Fe powders

4.2. Cold spray process

The experimental tests were performed at Politecnico di Milano, and the equipment used for these cold spray tests consisted of an ABB IRB4600 (40 kg) robot (Figure 4.2) and the cold spray system itself. The cold spray system is an Impact Innovations ISS 5/11 (Impact Innovations Inc., Germany) with a convergent-divergent SiC Out-1 nozzle (expansion ratio: 5.6) (Figures 4.3 and 4.4).



Figure 4.2: Spray gun mounted on the robotic arm.



Figure 4.3: Impact Innovations ISS 5/11 spray gun



Figure 4.4: Impact powder feeders

4.2.1. Wipe test

The wipe test allows us to qualitatively identify the behavior of a particle after impacting a determined substrate. To perform this test, the spray gun operates at a considerably

higher speed compared to both the thin-layer deposit test and the adhesion probability experimental tests, which will be detailed later. This higher speed allows the deposition of nearly individual particles, preventing their overlapping. After spraying, the substrates will be embedded in resin and analyzed under a microscope to analyse the material interaction.

For these experimental tests, nitrogen was used as the process gas at a pressure of 50 bar and a temperature of 450^{o}C. The substrates used for these tests were aluminum alloy (Al6032) and pure iron, both with dimensions of 20×25 mm. Both substrates were polished until reaching a $1\mu m$ diamond suspension solution. The parameters related to the movement of the spray gun were as follows: a stand-off distance (SOD) of 20 mm, a transverse speed of 750 mm/s for aluminum powder being deposited on an iron substrate, and 1600 mm/s for all other combinations. For this type of test, only a single pass was made for each sample.

After spraying, the samples were cut to obtain a visible cross-section and then embedded using a conductive resin. These specimens were grinded and polished until 1 um and then with UPS solution to obtain a better surface for analysis under the microscope. The SEM used for analysis was a Zeiss EVO 50 Scanning Electron Microscope (Carl Zeiss Microscopy GmbH, Germany).

4.2.2. Thin layer deposit

In a thin layer deposits, the spray gun generates coatings of considerable thickness, allowing for the analysis of the effective composition of the coating and the determination of DE.

For these experimental tests, nitrogen was used as the process gas at a pressure of 50 bar and a temperature of 450^{o}C. The substrates used for these tests were aluminum alloy (Al6032) and pure iron, both with dimensions of 20×20 mm. Both substrates were previously sandblasted with a powder of 60 mesh size. The sprayed area covered a region of 15×30 mm. The parameters related to the movement of the spray gun were as follows: a stand-off distance (SOD) of 20 mm, a transverse speed of 250 mm/s, and a hatch distance of 1 mm. Six different samples were obtained for three different feedstocks, with two substrates for each feedstock, leading to the following experimental tests:

- 25% aluminum and 75% iron on an aluminum substrate
- 50% aluminum and 50% iron on an aluminum substrate
- 75% aluminum and 25% iron on an aluminum substrate

- 25% aluminum and 75% iron on an iron substrate
- 50% aluminum and 50% iron on an iron substrate
- 75% aluminum and 25% iron on an iron substrate

After performing these tests, the samples were cut and embedded into a non-conductive resin and then polished until 1 um and then with the UPS solution, so that they could be analyzed under a microscope. The microscope used was a Zeiss EVO 50 Scanning Electron Microscope (Carl Zeiss Microscopy GmbH, Germany). The obtained results were then analyzed using ImageJ software version 1.53A, as shown in Figure 4.5.

Images/Figureschapter4/Coatinganaly01.jpg

Figure 4.5: (a) Image obtained with the SEM microscope for a coating with a feedstock of 50% Al and 50% Fe on an aluminum substrate, and (b) composition analysis performed using ImageJ software.

4.2.3. Adhesion probabilities test

The adhesion probability tests consist of spraying the two different materials onto various impact surfaces, which could be either the substrates or materials with previous deposits. The aim of this is to later calculate the deposition efficiencies, allowing us to understand the different interactions between materials, which will later be introduced into the DE predictive model. The calculation of the DE for each case follows the procedure described in Subsection 1.4.2.

As mentioned in Subsection 2.1.4, six adhesion probabilities are needed to apply the model for a given substrate material. In this research, eight experimental tests were performed due to the fact that two different substrates are being analyzed. The layout of the different experimental tests is shown in Figure 4.6, where it can be seen that eight different samples will be analyzed.

Two main procedures were applied. The first one consists of generating a thin layer deposit by using a larger hatch distance and, therefore, a lower number of passes, as well as higher transverse speeds in some cases. The second procedure consists of obtaining thicker deposits; to achieve this, a lower hatch distance was applied, leading to a higher number of passes.

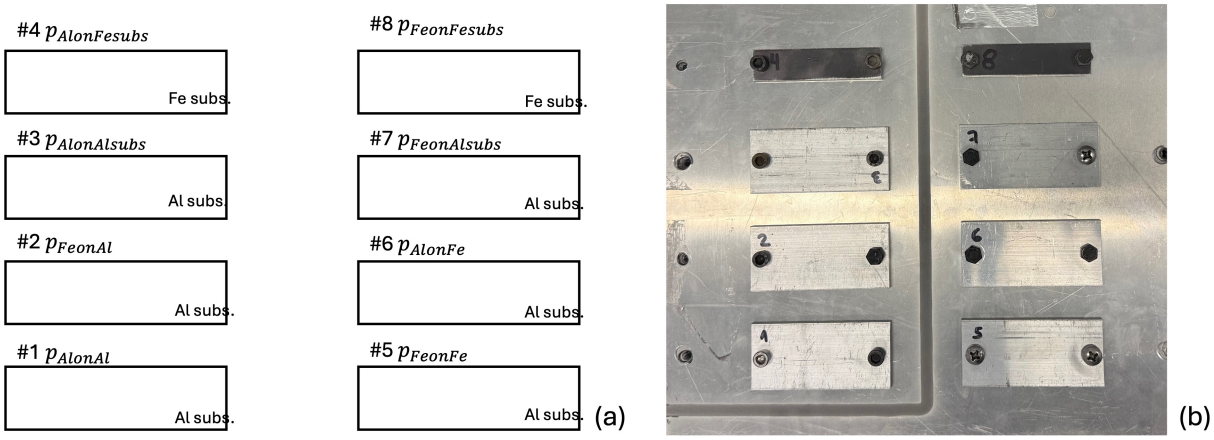


Figure 4.6: (a)Layout of the experimental tests, and (b) samples before the spraying process

Before spraying, the transverse speed values need to be optimized. To achieve this, a track optimization process was performed. This process involved spraying iron and aluminum powders onto aluminum substrates, making three passes at the following transverse speeds: *250 mm/s*, *350 mm/s*, and *500 mm/s*. The goal of this process was to find the optimal transverse speed that leads to a coating thickness close to the particle diameter.

To analyze the thickness of the different passes, the sprayed tracks were examined using an Anton Paar Step machine (Figure 4.7).

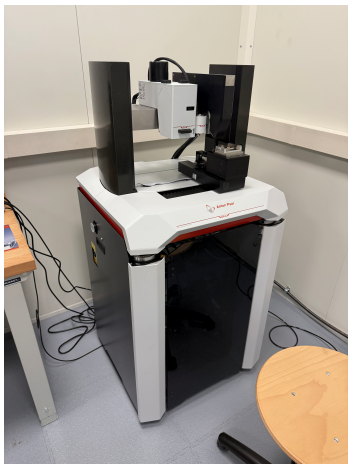


Figure 4.7: Anton paar Step machine

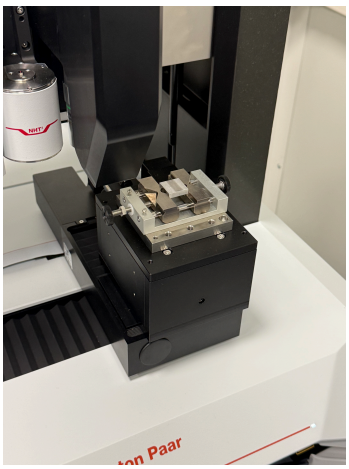


Figure 4.8: Sample holder in Anton paar machine

To obtain the adhesion probabilities, the substrates were weighed before and after spraying to determine the amount of deposited material. These measurements were performed

using a high-precision electronic Scaltec SBC22 scale, with an accuracy of 0.0001 g.

Before performing the tests, all the samples were sandblasted with a ceramic powder of 60 mesh size. After sandblasting, the samples were sprayed using nitrogen gas at a pressure of 50 bar and a temperature of 450ºC, all of them at a stand of distance of 20 mm. The experimental tests were conducted using two types of substrates: an aluminum alloy (Al6082) substrate with dimensions of 85×40 *mm* and a spray area of 50×55 *mm*, and pure iron substrates with dimensions of 85×20 *mm* and a spray area of 50×35 *mm*.

For samples #1 and #2, indicated in Figure 4.6, aluminum alloy (Al6032) substrates were used. The deposit consisted of a two-layer aluminum powder coating, where each layer was produced by performing fifty passes at a transverse speed of *250 mm/s* with a hatch distance of 1 mm. After this first step, both samples were weighed, and a second spraying process was performed.

For sample #1, after the two-layer deposit was performed, a thin-layer aluminum powder deposit was applied, consisting of six passes at a transverse speed of *500 mm/s* with a hatch distance of 8 mm. For sample #2, instead, the same thin-layer deposit was produced but using iron powder at a transverse speed of *250 mm/s*.

For samples #3 and #4, thin-layer deposits were produced, both made with aluminum powder. Each deposit consisted of six passes at a transverse speed of *500 mm/s* and a hatch distance of 8 mm. However, for sample #3, the substrate was the aluminum alloy, while for sample #4, the substrate was pure iron.

In the case of samples #5 and #6, aluminum alloy substrates were used, and a thick-layer deposit was produced with iron powder. This deposit consisted of two layers, each formed by 50 passes at a transverse speed of *250 mm/s* with a hatch distance of 1 mm. After producing these two layers, the samples were weighed. For sample #6, a thin-layer deposit was then produced by spraying aluminum powder, using six passes with a hatch distance of 8 mm and a transverse speed of *500 mm/s*.

Finally, for samples #7 and #8, thin-layer deposits were produced by spraying iron powder, making six passes at a hatch distance of 8 mm and a transverse speed of *250 mm/s*. In the case of sample #7, an aluminum alloy substrate was used, whereas for sample #8, a pure iron substrate was used.

For the theoretical calculation of the mass of the deposited material, the sprayed volume can be multiplied by its apparent density. The challenge in this process arises from the fact that the nozzle sprays material before being fully positioned over the substrate. To account for this, the theoretical deposited material is divided into three steps, as shown

in Figure 4.9. Sections 1 and 3 consider the nozzle gradually moving into and out of the substrate, while Section 2 accounts for the period when the nozzle is fully positioned over the substrate.

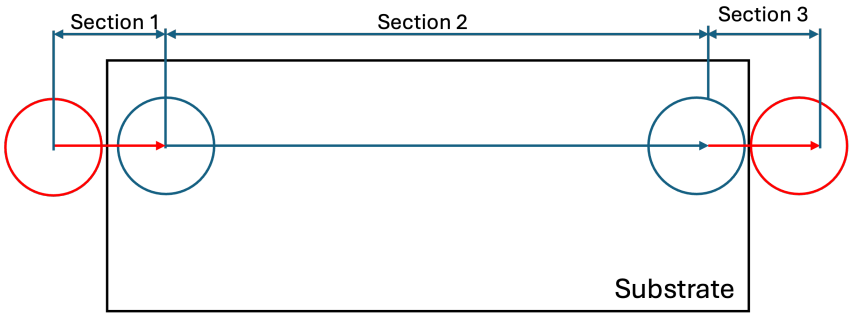


Figure 4.9: Schematic of the sections used for the calculation of theoretical deposited mass for a single pass.

The volume of deposited material is calculated similarly for both Sections 1 and 3 and is described by Equation (4.1), where t_i corresponds to the time required for the nozzle to transition from fully outside/inside the substrate to being fully inside/outside of it, $\dot{V}$ is the volumetric flow rate of material supplied by the CS feeder, $A(t)$ represents the area of the nozzle inside the substrate as a function of time, defined in Equation (4.2), and A is the total nozzle area.

$$V_i = \int_0^{t_i} \dot{V} \cdot \frac{A(t)}{A} \cdot t \, dt \tag{4.1}$$

In Equation (4.2), r corresponds to the radius of the region sprayed by the nozzle, v_t is the transverse speed at which the nozzle is moving, and t represents the time instant.

$$A(t) = r^2 \cos^{-1}\left(\frac{r - v_t t}{r}\right) - r(r - v_t t)\cos\left[\sin^{-1}\left(\frac{r - v_t t}{r}\right)\right] \tag{4.2}$$

4.3. Enhanced FEM assisted DE predictive model

The enhanced FEM-assisted DE predictive model was developed as an improvement to the FEM-assisted DE predictive model proposed by A. Ardeshiri Lordejani et al. [14]. The focus of this improvement is to account for different particle sizes while calculating the composition of the layers. To achieve this, the probability distribution of the powders mentioned in Section 4.1 will be considered. For this research, three different particle

sizes will be used, and the probabilities introduced into the model correspond to the conditional probability of obtaining a particle of a given size, considering that only these three particle sizes can be obtained.

Thus, we define a set of three different particle sizes for each powder, as described in Equation (4.3).

$$\{D\} = \begin{bmatrix} D_1 & D_2 & D_3 \end{bmatrix} \tag{4.3}$$

Equation (4.4) represents the probability of obtaining a particle of size D_j. This probability is extracted from the data presented in Section 4.1.

$$P(A) = P(D_j) \tag{4.4}$$

Additionally, the probability of obtaining a particle among the three different sizes is described in Equation (4.5), which corresponds to the sum of the probabilities of individually obtaining each of the three particle sizes. These values are obtained from the probability distribution.

$$P(B) = P(\{D\}) = P(D_1) + P(D_2) + P(D_3) \tag{4.5}$$

Given both the probability of obtaining a single particle and the sum of the three probabilities, the conditional probability can be calculated, as shown in Equation (4.6).

$$P(A|B) = \frac{P(A \cap B)}{P(B)} = \frac{P(D_j)}{P(D_1) + P(D_2) + P(D_3)} \tag{4.6}$$

By incorporating multiple particle sizes, the model aims to provide a more accurate prediction. This model will calculate the values of ILA, LA, and RLA for each layer, going through a certain number of iterations per layer, as shown in Figure 4.10. In every iteration, the splat radius used will vary, along with the relative splat areas. This approach results in a behavior that more closely resembles the experimental observations, where not all particles are of average size.

For this research, only three different sizes for each powder type were considered. This will lead to a set of different splat radii depending on the particle size. The particle size for each iteration will be selected based on its probability of occurrence, in accordance with the data provided by Malvern PANalytical Ltd., UK. The probability of occurrence for each particle size is shown in Table 4.1.

Aluminum particle size	$P(D_j)$	Iron particle size	$P(D_j)$
$D_1 = 20.39[\mu m]$	18.29%	$D_1 = 19.98[\mu m]$	23.85%
$D_2 = 32.1[\mu m]$	62.02%	$D_2 = 31.53[\mu m]$	57.27%
$D_3 = 53.11[\mu m]$	19.68%	$D_3 = 47.33[\mu m]$	18.88%

Table 4.1: Particle sizes and the probability of obtaining them

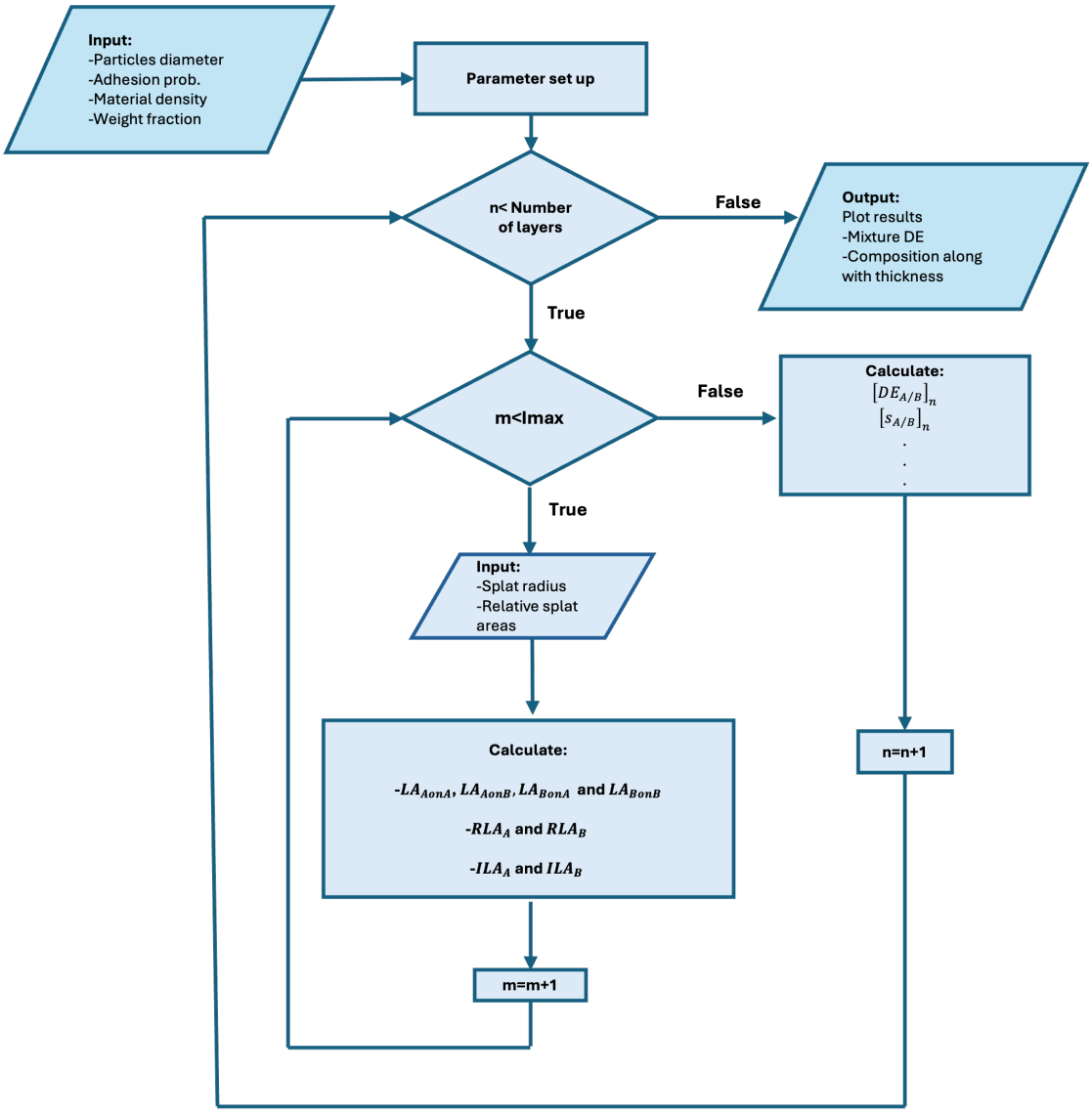


Figure 4.10: Flow diagram used for the prediction of the composition in the coating

First, the height and the number concentration of powder particles will be calculated as described in Equations (2.23)-(2.25), following the procedure outlined by A. Ardeshiri Lordejani et al. [14]. These values will remain constant throughout the entire iterative process.

On the other hand, the splat radius will change in each iteration as a function of the particle diameter (D_j) selected in that iteration, following the probabilities presented in Table 4.1. Consequently, the splat areas will also depend on the particle diameter (D_j), as well as the relative splat areas. The splat area calculations will be performed as described in Equations (4.7) and (4.8).

$$S_{A-A}(D_j) = \frac{A_{A-A}(D_j)}{A_{A-A}(D_j) + A_{B-A}(D_j)} \tag{4.7}$$

$$S_{B-A}(D_j) = \frac{A_{B-A}(D_j)}{A_{A-A}(D_j) + A_{B-A}(D_j)} = 1 - S_{A-A}(D_j) \tag{4.8}$$

Where A_{A-A} corresponds to the splat area of a particle of material A upon impact with a surface composed of material A. To calculate this splat area, it will be assumed to be a circle with a radius equal to the splat radius. These splat areas will be calculated for all combinations of powders and substrates used in the case study. Additionally, they will be a function of the particle size D_j, which will vary throughout the iterations.

The notation for the data acquired for each layer will be written as $[value]n$, being n the layer number. Then, understanding that the relative splat areas are going to have a variable value for every iteration, the model first calculates the composition in the first layer, considering the interaction between the two materials and the substrate. The first step consists in calculating the relative areas, and thus the percentage of area covered by each material, using Equations (4.9) and (4.10).

$$[s_A]_1 = \frac{p_{A-S} c_A S_{A-S}(D_j)}{c_A S_{A-S}(D_j) + p_{B-S} c_B S_{B-S}(D_j)} \tag{4.9}$$

$$[s_B]_1 = \frac{p_{B-S} c_B S_{B-S}(D_j)}{c_A S_{A-S}(D_j) + p_{B-S} c_B S_{B-S}(D_j)} = 1 - [S_A]_1 \tag{4.10}$$

In the previous equations, the relative splat areas covered by both materials, s_A and s_B, are calculated. To do so, the adhesion probabilities of materials A and B on the substrate are used, following the notation p_{A-S}, which was previously detailed in Subsection 2.1.4. This adhesion probability accounts for the interaction between different powders and substrates. The last term corresponds to the relative splat areas, $S_{A-S}(D_i)$ and $S_{B-S}(D_i)$, which depend not only on the interacting materials but also on the particle size, which varies in each iteration.

For the esquations For the DE of each material in the first layer, they will be calculated as follows:

$$[DE_A]_1 = p_{A-S} \tag{4.11}$$

$$[DE_B]_1 = p_{B-S} \tag{4.12}$$

$$[DE]_1 = f_A \times p_{A-S} + f_B \times p_{B-S} \tag{4.13}$$

Since a new iterative process has now been introduced, the notation for the calculated parameters is $[(value)_m]_n$, with m as the iteration number and n as the layer number.

According to the method described by A. Ardeshiri Lordejani et al. [14], the first iteration of the second layer accounts for the composition of the previous layer (first layer). To achieve this, the RLA incorporates its composition, as described by Equations (4.14) and (4.15).

$$[(RLA_A)]_2 = [s_A]_1 \tag{4.14}$$

$$[(RLA_B)]_2 = [s_B]_1 \tag{4.15}$$

Once the RLA is known, the LA can be calculated by considering the adhesion probabilities for each material, the different relative splat areas, and the powder number concentration, following the relationships from Equations (4.16)-(4.19). Where LA_{AonA} correspond to the new layer area of material A formed on top of the area originally covered by material A.

$$[(LA_{AonA})_1]_2 = c_A p_{A-A} \, [(RLA_A)_1]_2 \, SA_{A-A}(D_j) \tag{4.16}$$

$$[(LA_{AonB})_1]_2 = c_A p_{A-B} \, [(RLA_B)_1]_2 \, SA_{A-B}(D_j) \tag{4.17}$$

$$[(LA_{BonA})_1]_2 = c_B p_{B-A} \, [(RLA_A)_1]_2 \, SA_{B-A}(D_j) \tag{4.18}$$

$$[(LA_{BonB})_1]_2 = c_B p_{B-B} [(RLA_B)_1]_2 SA_{B-B}(D_j) \tag{4.19}$$

In addition, the ideal layer area (ILA) can be determined by applying the approach described in Equations (4.20) and (4.21).

$$[(ILA_A)_1]_2 = c_A \{[(RLA_A)_1]_2 SA_{A-A}(D_j) + [(RLA_B)_1]_2 SA_{A-B}(D_j)\} \tag{4.20}$$

$$[(ILA_B)_1]_2 = c_B \{[(RLA_A)_1]_2 SA_{B-A}(D_j) + [(RLA_B)_1]_2 SA_{B-B}(D_j)\} \tag{4.21}$$

The RLA, LA, and ILA values will be iteratively calculated until the layer is fully covered, meaning that RLA_A and RLA_B are equal to 0, or until the maximum number of iterations is reached. The equations described below correspond to the generalized equations for the m^{th} iteration of these parameters:

The RLA calculations, as explained in Equations (4.22) and (4.23), for the m^{th} iteration will be determined as the relative percentage areas of the respective material minus the LA of both A and B from the $(m-1)^{th}$ iteration.

$$[(RLA_A)_m]_2 = [s_A]_1 - \left\{\left[(LA_{AonA})_{m-1}\right]_2 + \left[(LA_{BonA})_{m-1}\right]_2\right\} \tag{4.22}$$

$$[(RLA_B)_m]_2 = [s_B]_1 - \left\{\left[(LA_{AonB})_{m-1}\right]_2 + \left[(LA_{BonB})_{m-1}\right]_2\right\} \tag{4.23}$$

The Equations (4.24)-(4.27) correspond to the LA calculations for the m^{th} iteration. To compute them, they take into account the concentration of powder particles, the relative splat areas, the adhesion probabilities, and the sum of all RLAs up to the m^{th} iteration.

$$[(LA_{AonA})_m]_2 = c_A p_{A-A} \left\{\sum_{i=1}^{m} [(RLA_A)_i]_2\right\} SA_{A-A}(D_j) \tag{4.24}$$

$$[(LA_{AonB})_m]_2 = c_A p_{A-B} \left\{\sum_{i=1}^{m} [(RLA_B)_i]_2\right\} SA_{A-B}(D_j) \tag{4.25}$$

$$[(LA_{BonA})_m]_2 = c_B p_{B-A} \left\{\sum_{i=1}^{m} [(RLA_A)_i]_2\right\} SA_{B-A}(D_j) \tag{4.26}$$

$$[(LA_{BonB})_m]_2 = c_B p_{B-B} \left\{ \sum_{i=1}^{m} [(RLA_B)_i]_2 \right\} SA_{B-B}(D_j) \tag{4.27}$$

The ILA calculations for the m^{th} iteration, described in Equations (4.28) and (4.29), are essentially determined as the sum of all the ILA values from the previous iterations. Thus, the RLA values of both materials, the relative splat areas, and the concentration of powder particles are taken into account.

$$[(ILA_A)_m]_2 = c_A \left\{ \sum_{i=1}^{m} [(RLA_A)_i]_2 \, SA_{A-A}(D_j) + [(RLA_B)_i]_2 \, SA_{A-B}(D_j) \right\} \tag{4.28}$$

$$[(ILA_B)_m]_2 = c_B \left\{ \sum_{i=1}^{m} [(RLA_A)_i]_2 \, SA_{B-A}(D_j) + [(RLA_B)_i]_2 \, SA_{B-B}(D_j) \right\} \tag{4.29}$$

After all the required iterations to form the layer have been completed, a few parameters must be set for use in subsequent layers. These are the relative splat areas and the DE for both materials, which are calculated as follows:

$$[DE_A]_2 = \frac{[(LA_{AonA})_m]_2 + [(LA_{AonB})_m]_2}{[(ILA_A)_m]_2} \tag{4.30}$$

$$[DE_B]_2 = \frac{[(LA_{BonA})_m]_2 + [(LA_{BonB})_m]_2}{[(ILA_B)_m]_2} \tag{4.31}$$

$$[DE]_2 = f_A \times [DE_A]_2 + f_B \times [DE_B]_2 \tag{4.32}$$

$$[s_A]_2 = [(LA_{AonA})_m]_2 + [(LA_{AonB})_m]_2 \tag{4.33}$$

$$[s_B]_2 = [(LA_{BonA})_m]_2 + [(LA_{BonB})_m]_2 \tag{4.34}$$

5 | Results and discussion

5.1. Impact simulation results

Regarding the particle impact simulations, eighteen simulations were performed. The purpose of these simulations was to obtain the splat radius, which, as described in Section 4.3, is necessary to calculate the relative splat areas and, consequently, the other parameters required to determine the composition and DE of the coating for each layer.

The eighteen impact simulations that were performed considered the impact of aluminum and iron particles of three different sizes, as shown in Table 4.1, onto two different substrates: the aluminum alloy Al6082 and the pure iron substrate. In addition to these simulations, impacts on surfaces composed of both pure aluminum and pure iron powders were also analyzed, leading to the following list of combinations:

- Aluminum on aluminum powder
- Aluminum on iron powder
- Aluminum on aluminum substrate
- Aluminum on iron substrate
- Iron on aluminum powder
- Iron on iron powder
- Iron on aluminum substrate
- Iron on iron substrate

The first attempts at impact simulations were performed using the Lagrangian method. However, the results for the cases where material combination with iron and aluminum were not satisfactory due to excessive element distortion, as shown in Figures 5.1 and 5.2.

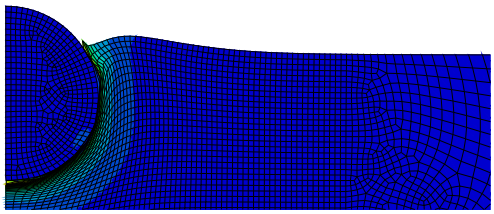


Figure 5.1: Fe on Al powder impact simulation

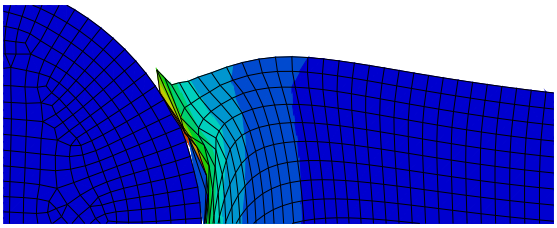


Figure 5.2: Distorted elements in an Fe on Al powder impact simulation

To overcome the problem of mesh distortion, particle impact simulations were performed using the CEL method, which significantly reduced element distortion and was more appropriate due to the large plastic deformations occurring in the interactions between iron and aluminum, as shown in Figures 5.3–5.5. For this simulation, the substrate corresponded to the Lagrangian domain, while the particle was assigned to the Eulerian domain.

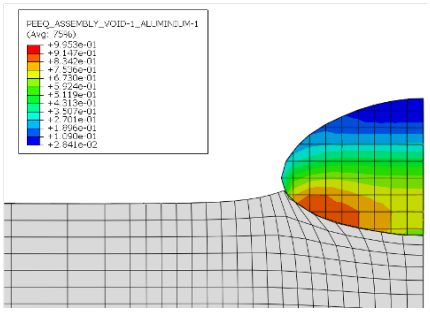


Figure 5.3: Al on Al powder impact simulation with a particle diameter of 20.39μm

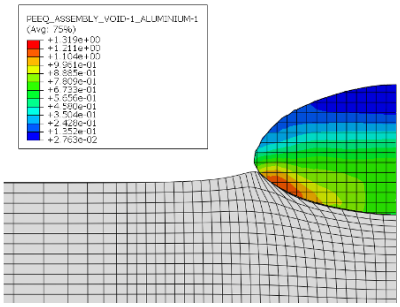


Figure 5.4: Al on Al powder impact simulation with a particle diameter of 32.1μm

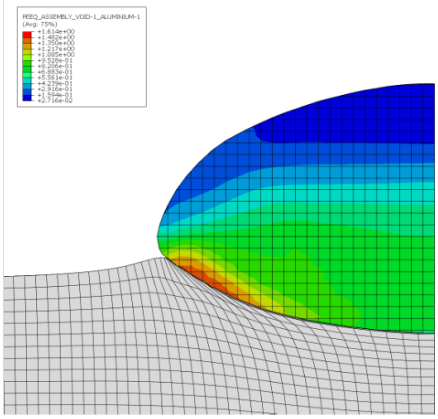


Figure 5.5: Al on Al powder impact simulation with a particle diameter of 53.11μm

In Figures 5.6–5.8, the Eulerian and Lagrangian domains were defined just like in the aluminum on aluminum powder impact simulations, with the substrate being part of the Lagrangian domain and the particle part of the Eulerian domain.

Besides that, in Figure 5.7, the particle has a really large plastic deformation with a more flattened shape compared to the other ones, while the substrate has barely undergone plastic deformation. In Figure 5.8, it is slightly less deformed compared to the aluminum on aluminum powder/substrate impacts.

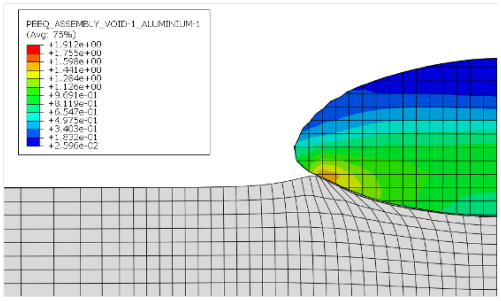


Figure 5.6: Al on Al substrate impact simulation with a particle diameter of 32.1μm

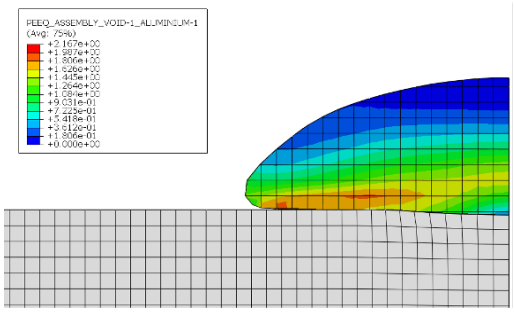


Figure 5.7: Al on Fe powder impact simulation for with a particle diameter of 32.1μm

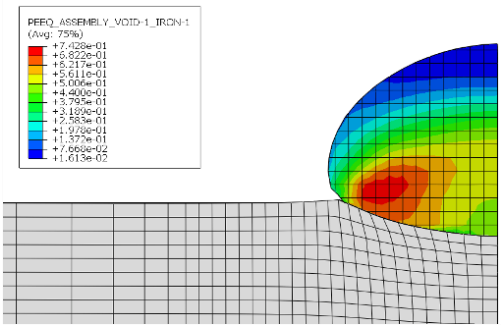


Figure 5.8: Fe on Fe powder impact simulation with a particle diameter of 31.53μm

For the iron on aluminum powder and substrate impact simulations shown in Figures 5.9 and 5.10, the Lagrangian and Eulerian domains were inverted, defining the particle as part of the Lagrangian domain and the substrate as the Eulerian domain. This is due to the fact that the substrate undergoes considerably larger plastic deformations compared to the particle.

In Figures 5.9 and 5.10, it can be seen that the particles penetrate deep into the substrate. This is because the iron powder is considerably harder compared to both the pure aluminum powder and the aluminum alloy.

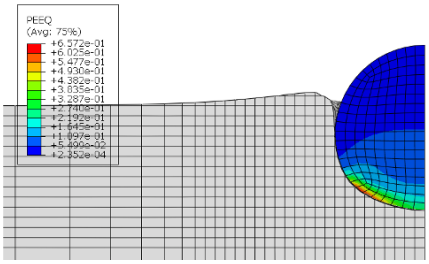


Figure 5.9: Fe on Al powder impact simulation with a particle diameter of $31.53\mu m$

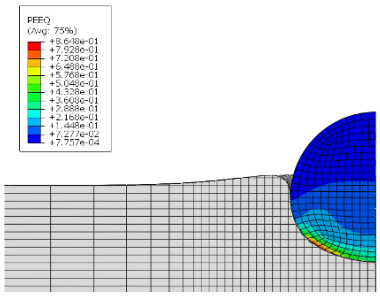


Figure 5.10: Fe on Al substrate impact simulation with a particle diameter of $31.53\mu m$

After performing all the simulations, the splat radii were measured for all of them, leading to the results shown in the Tables 5.1 and 5.2. The first one correspond to the splat radius to be used for a coating deposited on the aluminum alloy substrate, while the Table 5.2 correspond to the data related to the coating deposited in the pure iron substrate.

	Al on Al	**Al on Fe**	**Al on Al subs.**	**Al on Fe subs.**
D1	12.590	14.504	13.599	14.504
D2	20.674	24.474	23.151	24.474
D3	36.229	43.706	37.468	43.706

Table 5.1: Splat radii for aluminum particles on different powder and substrates.

	Fe on Al	**Fe on Fe**	**Fe on Al subs.**	**Fe on Fe subs.**
D1	10.1667	11.95	10.3156	11.95
D2	16.033	18.995	16.3757	18.995
D3	24.035	28.254	24.4259	28.254

Table 5.2: Splat radii for iron particles on different powders and substrates.

5.2. Wipe test impact particle results

The wipe test results allow us to understand how one material particles behave upon impact with same or different material surfaces and thus qualitatively compare them with the FE impact simulations.

From Figure 5.12, it can be seen that the aluminum particle, upon impact with an iron substrate, completely flattens, similar to what was observed in Figure 5.7. Meanwhile, in the case presented in Figure 5.13, the iron particle penetrates deeply into the substrate, just like the modeled behavior obtained by FE in Figure 5.9.

For Figures 5.11 and 5.14, it can be observed that both the particle and the substrate undergo plastic deformation, rather than just one of them. This can be explained by the fact that in Figure 5.14, both the particle and the substrate are composed of pure iron, meaning they have the same hardness. In the case of Figure 5.11, even though the materials are not identical, since pure aluminum particles impact an aluminum alloy substrate, they still possess similar mechanical properties. As the hardness difference between them is not significant, plastic deformation can be identified in both the particle and the substrate.

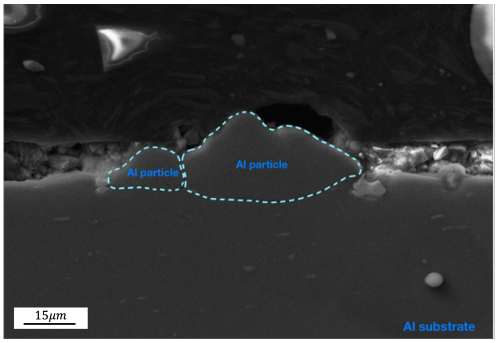


Figure 5.11: Aluminum particles deposited on an aluminum substrate

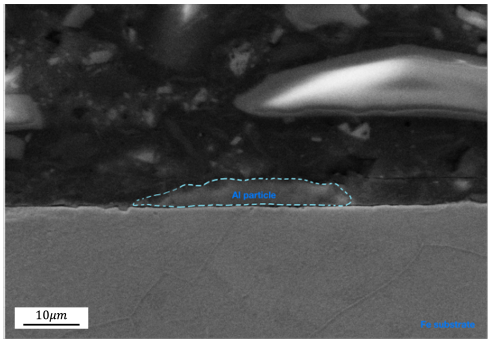


Figure 5.12: Aluminum particle deposited on an iron substrate

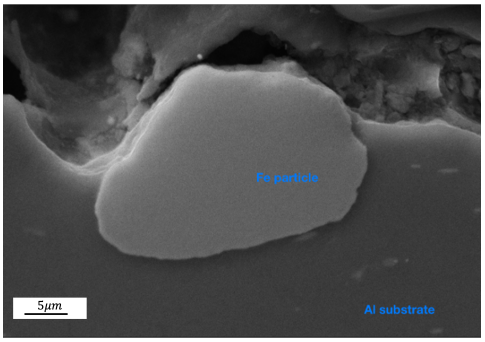


Figure 5.13: Iron particle deposited on an aluminum substrate

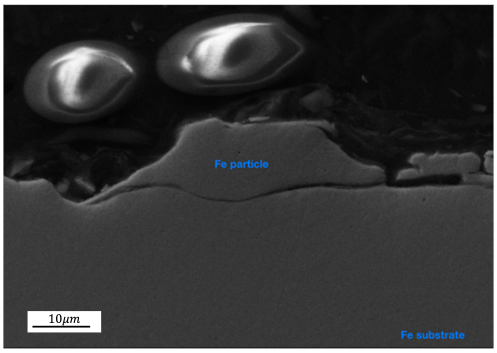


Figure 5.14: Iron particle deposited on an iron substrate

Besides that, during the analysis of the wipe test samples, it was noticed that not all these interactions occurred with the same frequency. The most frequently observed interaction

during the microscope analysis was iron particles impacting an aluminum substrate, where the particles most often penetrated deeply into the substrate. This was followed by aluminum particles impacting an aluminum substrate and iron particles impacting an iron substrate, which were observed less frequently but still in greater numbers than the last interaction, where aluminum particles impacted an iron substrate.

5.3. Adhesion probabilities obtained experimentally

After performing the experimental tests, the mass of the deposited material was measured, and the theoretical amount of material was also calculated following the procedure described in Subsection 4.2.3.

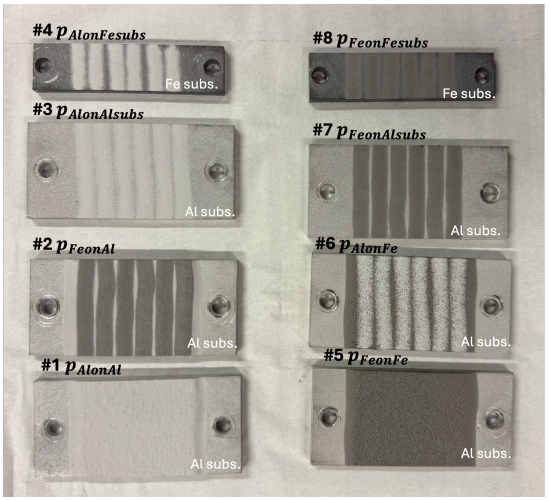


Figure 5.15: Samples used to determine the amount of deposited material

After performing the experimental tests, both the theoretical deposited material and the experimentally obtained deposited material were compared to determine the adhesion probabilities, as shown in Tables 5.3 and 5.4. In the case of iron, both the powder and the substrate were assumed to have the same properties, as explained in Section 3.2.

	p_{AlonAl}	$p_{AlonAlsubs}$	p_{AlonFe}	$p_{AlonFesubs}$
Deposited material [g]	0.0881	0.0849	0.01764	0.01764
Theoretical deposited material [g]	0.1625	0.1625	0.0627	0.0627
DE %	54.22%	52.24%	28.12%	28.12%

Table 5.3: Comparison between deposited, theoretical deposited material, and deposition efficiency (DE) for pure aluminum powder.

	p_{FeonAl}	$p_{FeonAlsubs}$	p_{FeonFe}	$p_{FeonFesubs}$
Deposited material [g]	0.486	0.393	0.14	0.14
Theoretical deposited material [g]	0.8492	0.8492	0.3291	0.3291
DE %	53.23%	46.28%	42.54%	42.54%

Table 5.4: Comparison between deposited, theoretical deposited material, and deposition efficiency (DE) for pure iron powder.

Then, the adhesion probabilities were calculated for all the combinations, obtaining the following values:

- $p_{AlonAl} = 54.22\%$
- $p_{AlonFe} = 28.12\%$
- $p_{AlonAls} = 52.24\%$
- $p_{AlonFes} = 28.12\%$
- $p_{FeonAl} = 57.23\%$
- $p_{FeonFe} = 42.54\%$
- $p_{FeonAls} = 46.28\%$
- $p_{FeonFes} = 42.54\%$

The adhesion probabilities p_{AlonFe} and $p_{AlonFes}$ were considered equal, following the assumption made in Section 3.2, where it was stated that the properties of both the iron powder and the substrate are the same, as found in the literature. The same applies to the adhesion probabilities p_{FeonFe} and $p_{FeonFes}$.

These results are consistent with the behavior observed during the wipe test analysis, as the lowest adhesion probability corresponds to both aluminum particles impacting an iron substrate and iron powder. This behavior can also be justified by the significantly lower hardness of aluminum. A lower hardness means that the particle is less likely to penetrate the substrate, preventing mechanical interlocking, which has been proven to be one of the most significant bonding mechanisms in the CS process.

The completely opposite case can be observed in the interaction between iron and aluminum powder. Here, the iron particle is much harder compared to the aluminum particle, enabling mechanical interlocking as the particles deeply penetrate the formed coating. Additionally, for the interaction between iron particles and an aluminum substrate, a lower

adhesion probability is observed. This is reasonable if we consider that the aluminum alloy substrate is slightly harder compared to the aluminum powder.

For interactions between the same material, such as aluminum on aluminum powder and iron on iron powder, the values are also relatively high compared to the interactions between aluminum and iron. Since they share the same hardness, mechanical interlocking is easier to achieve. Besides that, the interactions between aluminum and aluminum powder/substrate are higher compared to the interactions between iron and iron powder/-substrate. This can also be explained by the fact that aluminum particles exhibit higher ductility, which facilitates plastic deformation, allowing the process to achieve higher DE values.

5.4. DE and composition along with thickness

The thin layer deposits were performed for the combinations of feedstocks and substrates indicated in Subsection 4.2.2. After processing them, the data regarding the composition along the thickness was analyzed, which will be detailed later in this section.

Coatings on an aluminum substrate

In Figures 5.16–5.18, the obtained cross-sections for coatings performed on an aluminum alloy substrate for the three different feedstocks previously mentioned can be seen. These cross-sections were embedded in resin and polished up to 1 micron, as described in Subsection 4.2.2, before capturing the images with the SEM to later analyse their compositions with the ImageJ software.

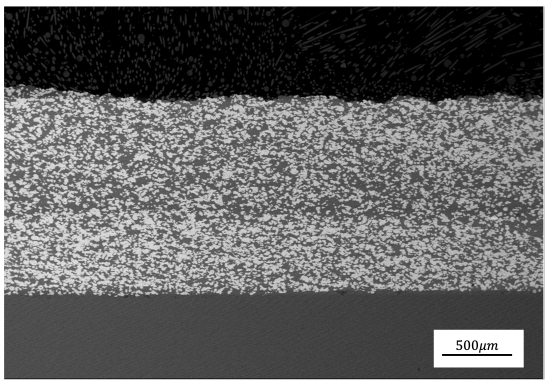


Figure 5.16: Coating performed with a Feedstock of 25% Al and 75% Fe on an aluminum substrate

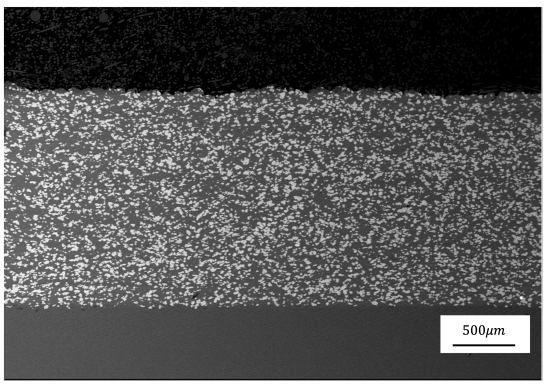


Figure 5.17: Coating performed with a Feedstock of 50% Al and 50% Fe on an aluminum substrate

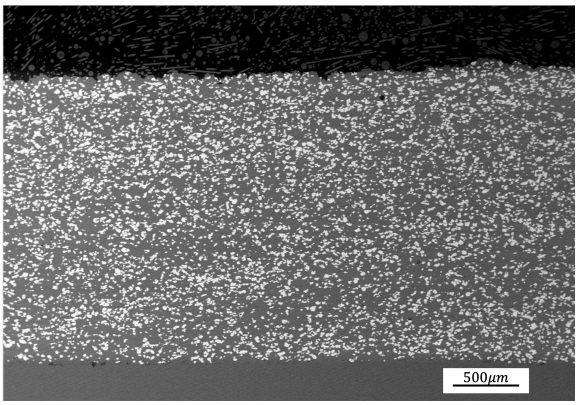


Figure 5.18: Coating performed with a Feedstock of 75% Al and 25% Fe on an aluminum substrate

In Figure 5.19, a comparison is presented between the experimentally obtained data and the results obtained with the predictive model for a feedstock of 25% Al and 75% Fe. Regarding the experimental data, two regions can be observed: near the substrate, a transient behavior occurs, where the aluminum composition initially reaches a maximum of 69.35% and then decreases until reaching a steady-state value that oscillates between 57.23% and 49.89%. This steady-state value is reached at a thickness of 45μm.

For the predictive model, the initial aluminum percentage calculated reaches 61.77% and then decreases until reaching a steady-state value at a thickness of 38μm that oscillates between 55.01% and 51.95%.

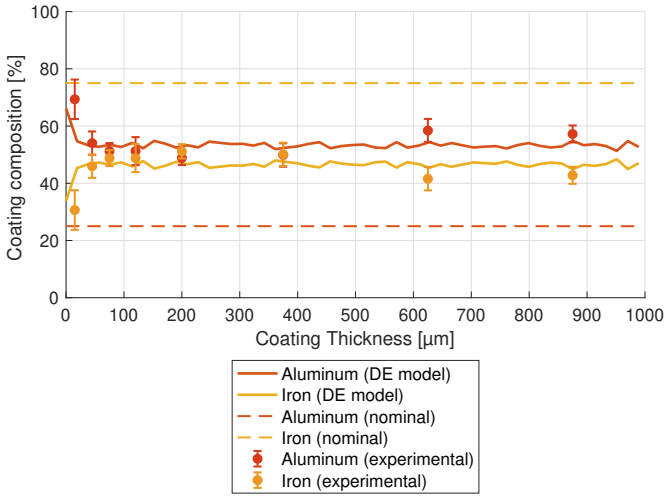


Figure 5.19: Comparison between the DE predictive model and the experimentally determined composition obtained for a feedstock of 25%Al and 75%Fe for an aluminum alloy substrate.

Figure 5.20 shows the comparison for a feedstock of 50% Al and 50% Fe, where two regions can also be observed. For the experimental data, the aluminum percentage at the beginning of the transient phase has a value of 85.79% and decreases to a steady-state value that oscillates between 73.84% and 74.89%. These values are reached at a thickness of $45\mu m$ in the experimental data.

For the predictive model, the transient phase starts at 86.17% and reaches a steady-state value at a thickness of $16.98\mu m$, with values oscillating between 80.25% and 77.50%.

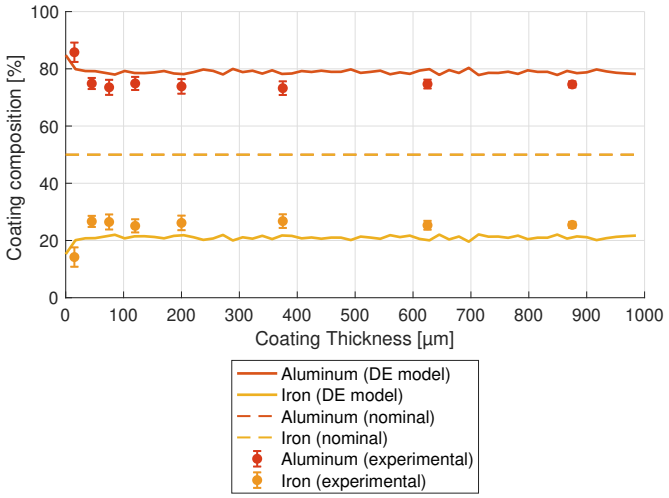


Figure 5.20: Comparison between the DE predictive model and the experimentally determined composition obtained for a feedstock of 50%Al and 50%Fe for an aluminum alloy substrate.

The composition for the coating with a feedstock of 75% Al and 25% Fe is shown in Figure 5.21. For this feedstock, a larger deviation can be observed between the experimental results and the predicted composition.

In the case of the experimentally determined aluminum percentage, a noticeable drop can be seen from the initial values in the transient state to the steady-state value. The initial aluminum percentage in the transient state corresponds to 91.03%, and the steady-state value is reached at a thickness of $75\mu m$, oscillating between 78.48% and 77.61%.

For the predictive model, a small change is observed from the beginning of the transient state to the steady state. The initially calculated aluminum percentage is 94.36%, differing from the experimental value by only 3.33%. The predictive model reaches the steady state at a thickness of $29\mu m$, with values oscillating between 92.78% and 91.56%, which is considerably higher than the experimental values, showing a difference of approximately 14%.

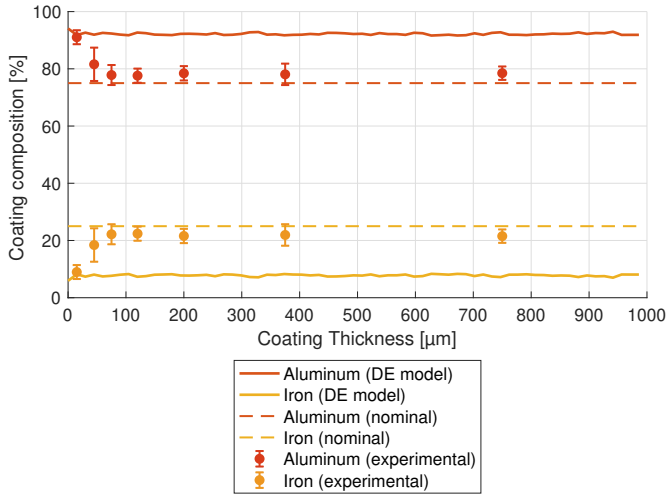


Figure 5.21: Comparison between the DE predictive model and the experimentally determined composition obtained for a feedstock of 75%Al and 25%Fe for an aluminum alloy substrate.

Coatings on an iron substrate

The results for the coating performed on a pure iron substrate can be seen in Figures 5.22-5.24, where three different feedstocks were used to produce the thin layer coatings.

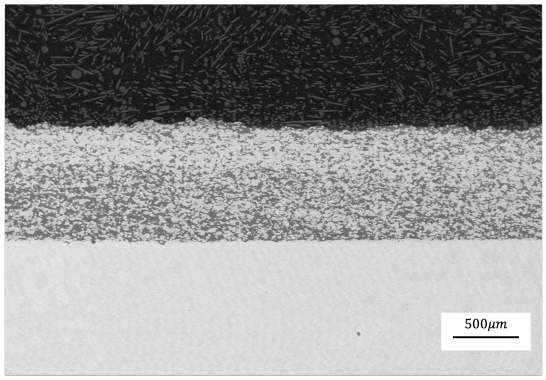


Figure 5.22: Coating performed with a Feedstock of 25% Al and 75% Fe on an iron substrate

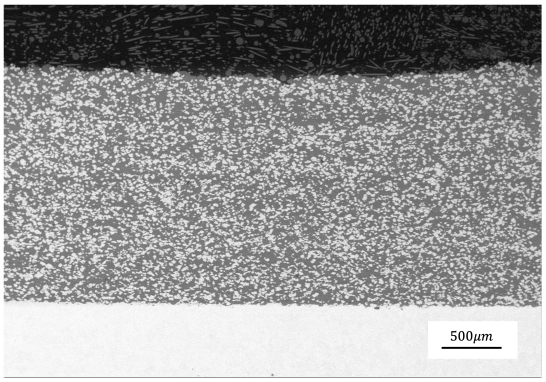


Figure 5.23: Coating performed with a Feedstock of 50% Al and 50% Fe on an iron substrate

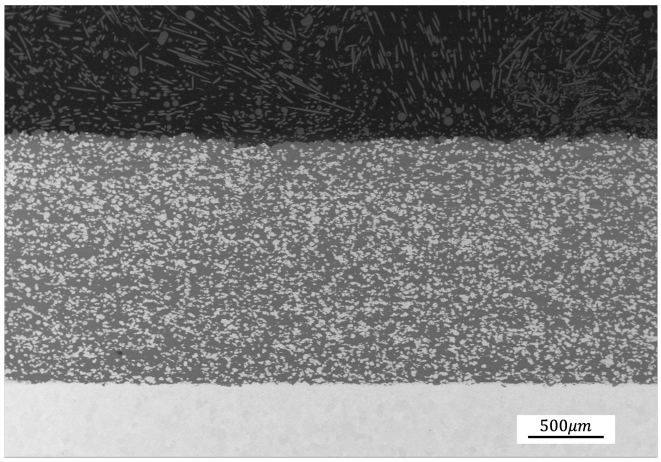


Figure 5.24: Coating performed with a Feedstock of 75% Al and 25% Fe on an Aluminum substrate

In Figure 5.25, it can be seen that the composition has not reached a steady-state value at the point furthest from the substrate, and thus the predictive model has not been able to correctly determine the composition along the thickness.

In the case of the experimental data, the aluminum percentage started at 48.16% and continuously decreased, reaching a value of 29.35% at a thickness of $733\mu m$. For the predictive model, the aluminum percentage oscillates between 47.27% and 55.45%, making it ineffective in accurately predicting the experimental behavior.

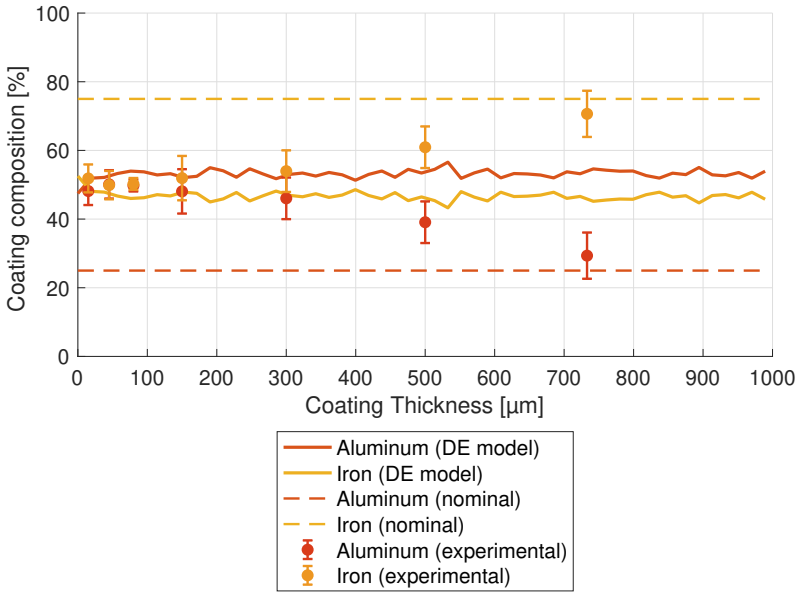


Figure 5.25: Comparison between the DE predictive model and the experimentally determined composition obtained for a feedstock of 25%Al and 75%Fe for an iron allow substrate.

In the case of a 50% Al–50% Fe feedstock, the results are shown in Figure 5.26, where it can be seen that the predictive model slightly overestimates the aluminum percentage.

The experimental data presents minimal differences between the transient phase and the steady state, where the initial aluminum percentage corresponds to 67.65% and then oscillates between 68.18% and 69.81%.

For the predictive model, a transition between the transient phase and steady state can be slightly noticed. The predicted aluminum percentage at the beginning of the transient phase is 73.05%, and the steady state is reached at a thickness of $33\mu m$, with the percentage oscillating between 81.19% and 77.65%.

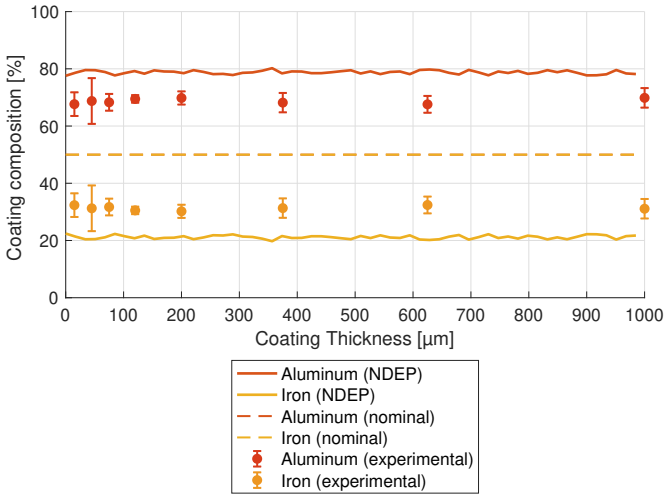


Figure 5.26: Comparison between the DE predictive model and the experimentally determined composition obtained for a feedstock of 50%Al and 50%Fe for a pure iron substrate.

For the coating obtained from a feedstock of 75% Al and 25% Fe, a higher deviation can be observed, with an overestimation of the aluminum percentage as well. From the experimental data, a transient phase cannot be clearly identified; the initial aluminum percentage is 69.70%, and along the thickness, this value oscillates between 69.32% and 73.63%. The predictive model does not show a clear transition between the transient phase and the steady state. The first calculated aluminum percentage corresponds to 89.05%, and then it oscillates between 91.52% and 92.90%. These values are higher compared to the experimental values, with a difference of approximately 19%.

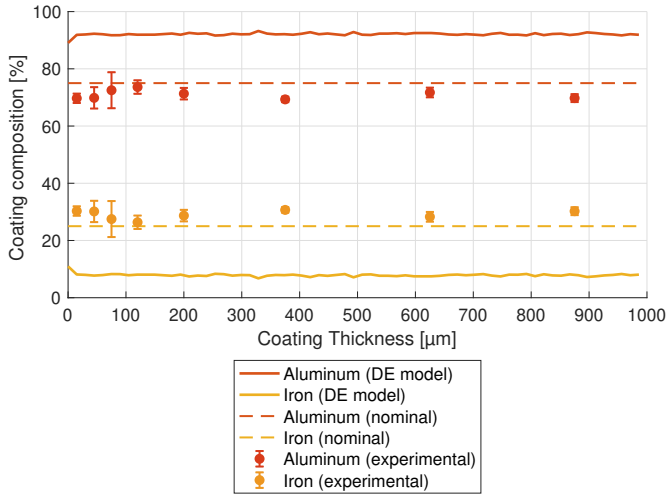


Figure 5.27: Comparison between the DE predictive model and the experimentally determined composition obtained for a feedstock of 75%Al and 25%Fe for a pure iron substrate.

The model is able to effectively predict the composition of the coating for feedstocks with less than 50% Al, but it shows a tendency to overestimate the aluminum percentage in the coating. This is particularly evident for feedstocks with 75% Al and 25% Fe, where the difference between the predicted aluminum percentage and the experimentally obtained values was 14% for the aluminum substrate case and 19% for the pure iron substrate. This discrepancy can be attributed to the fact that the particles were not completely spherical but rather elongated or oval-shaped. Not considering this possibly led to inaccuracies in the impact simulations and in the measurement of the adhesion probabilities, both of which are key inputs for the predictive model.

In Figures 5.28 and 5.29, the predicted DEs can be seen. In Figure 5.28, it can be observed that as the aluminum percentage increases in the feedstock, the DE also increases. However, the peak is not present at the highest aluminum percentage but at 75%. This trend shows a continuous increase, as both aluminum and iron exhibit good adhesion onto an aluminum substrate due to its ductility, which is beneficial for deposition.

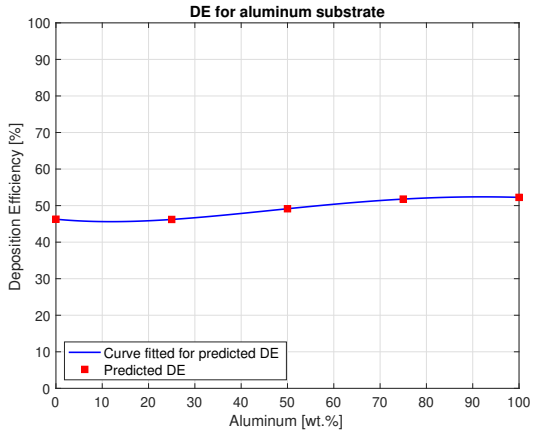


Figure 5.28: Predicted DE for 25%Al-75%Fe, 50%Al-50%Fe, and 75%Al-25%Fe onto an aluminum substrate.

For the DE of different feedstocks onto an iron substrate, a different behavior can be observed. The DE increases as the aluminum percentage rises, but it experiences a significant drop when reaching 100% aluminum. This occurs due to the low adhesion probability of aluminum on an iron substrate, primarily caused by the high hardness of the iron substrate. As a result, the aluminum particles barely deform the substrate upon impact, as seen in both the FE particle impact simulations and the wipe test results. The fact that the substrate does not deform is detrimental to particle adhesion, as it prevents the development of mechanical bonding mechanisms such as mechanical interlocking. For the iron substrate the highest value of DE is obtained for feedstock that has a 75% aluminum.

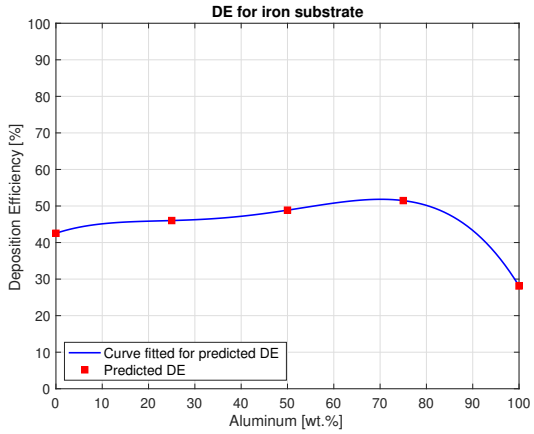


Figure 5.29: Predicted DE for 25%Al-75%Fe, 50%Al-50%Fe, and 75%Al-25%Fe onto an iron substrate.

6 | Conclusions

In this thesis work, a model was developed to predict the composition of a bimetallic coating produced by means of a cold spray process. The materials used to produce the coatings were pure aluminum powder and pure iron powder. These were deposited using three different feedstocks: 25% Al–75% Fe, 50% Al–50% Fe, and 75% Al–25% Fe, onto two different types of substrates: an aluminum alloy (Al6082) substrate and a pure iron ARMCO substrate. The objective was to develop a model capable of predicting their compositions.

The developed predictive model considered existing predictive models and enhanced them by incorporating the probability distribution of the bimetallic powder, thereby simulating a behavior that is closer to the experimental one. This model utilized both numerical simulations and experimental data as inputs to accurately predict the composition for different feedstocks and materials.

6.1. FEM particle impact simulations

For the numerical data, impact simulations were performed. One of the major challenges related to these simulations was the significant difference in hardness between the materials, leading to large plastic deformations. These deformations were later corroborated with the images obtained experimentally from the wipe tests.

To perform these simulations, the CEL method was selected due to its strong performance. This method allowed the preservation of regular elements after impact, ensuring a reliable simulation that could be later incorporated into the model. The CEL method successfully modeled both scenarios: when the substrate was significantly harder than the particle, leading to particle flattening, and the opposite case, where the particle was much harder than the substrate.

Thus, it can be stated that for particle impact simulations in a cold spray process, where large plastic deformations are expected, the CEL method proves to be highly effective. It allows for the accurate determination of the splat radius, which is later required for

predictive models.

6.2. DE predictive model

The model allows us to calculate the composition of the coating for a given bimetallic coating and different feedstocks. This model considers the interaction between the different materials, not only between the powders but also with the substrate, which enables a more comprehensive and detailed analysis, capturing both the transient and steady-state behavior.

Overall, the predictive model was able to accurately predict the composition for the different feedstocks. However, inaccuracies significantly increased as the aluminum powder percentage increased. This could be due to the fact that the aluminum powder morphology was not considered, i.e., a spherical particle was assumed, which may have affected both the experimental calculation of the adhesion probabilities and the impact simulations.

Beyond the obtained results, it is important to highlight that the developed predictive model holds significant potential in optimizing the manufacturing processes of bimetallic coatings. Although the predictions aligned well with most cases, considering additional parameters such as powder particle morphology could enhance the model's accuracy. As different material combinations and experimental conditions are explored, the model is likely to continue evolving, allowing its integration into more complex industrial applications, such as improving wear and corrosion resistance in critical components.

6.3. Future developments

The Enhanced FEM-assisted DE predictive model shows a strong performance but can be further improved by studying and incorporating the effect of powder particle morphology. As observed in this research, the fact that the aluminum particles were not completely spherical had a non-negligible impact on the model's output, leading to variations from the experimentally obtained results.

Since these particles are not perfectly spherical, their flowability is affected, which in turn influences the coating formation. This effect significantly impacts the adhesion probability calculations, a key input parameter for the predictive model. Additionally, it can influence the FE particle impact simulations, leading to variations in the splat radius after impact and, consequently, in the relative splat areas introduced into the iterative loop.

Bibliography

[1] Shuo Yin, Xiao-fang Wang, Bao-peng Xu, and Wen-ya Li. Examination on the Calculation Method for Modeling the Multi-Particle Impact Process in Cold Spraying. *Journal of Thermal Spray Technology*, 19(5):1032–1041, September 2010. ISSN 1059-9630, 1544-1016. doi: 10.1007/s11666-010-9489-9.

[2] Victor Kenneth Champagne, Ozan Cagatay Ozdemir, and Timothy J. Eden, editors. *Practical Cold Spray*, chapter 2, pages 27–51. Springer International Publishing, Cham, 2021. ISBN 978-3-030-70055-3 978-3-030-70056-0. doi: 10.1007/978-3-030-70056-0.

[3] M.F. SMITH. 3 - comparing cold spray with thermal spray coating technologies. In Victor K. Champagne, editor, *The Cold Spray Materials Deposition Process*, Woodhead Publishing Series in Metals and Surface Engineering, pages 43–61. Woodhead Publishing, 2007. ISBN 978-1-84569-181-3. doi: https://doi.org/10.1533/9781845693787.1.43.

[4] Victor Kenneth Champagne. *Introduction*, pages 1–25. Springer International Publishing, Cham, 2021. ISBN 978-3-030-70056-0. doi: 10.1007/978-3-030-70056-0_1.

[5] Yuji Ichikawa, Ryotaro Tokoro, Masatoshi Tanno, and Kazuhiro Ogawa. Elucidation of cold-spray deposition mechanism by auger electron spectroscopic evaluation of bonding interface oxide film. *Acta Materialia*, 164:39–49, 2019. ISSN 1359-6454. doi: https://doi.org/10.1016/j.actamat.2018.09.041.

[6] T. Van Steenkiste. *The cold spray materials deposition process: fundamentals and applications*, chapter 8, pages 127–147. Woodhead Publishing in materials. Woodhead, Cambridge Boca Raton, 2007. ISBN 978-1-84569-181-3 978-1-84569-378-7.

[7] Hamid Assadi, Tobias Schmidt, Horst Richter, J.-O Kliemann, Kurt Binder, F. Gärtner, Thomas Klassen, and Heinrich Kreye. On parameter selection in cold spraying. *Journal of Thermal Spray Technology*, 20:1161–1176, 12 2011. doi: 10.1007/s11666-011-9662-9.

[8] Surinder Singh, R. K. Singh Raman, Christopher C. Berndt, and Harpreet Singh.

Influence of cold spray parameters on bonding mechanisms: A review. *Metals*, 11 (12), 2021. ISSN 2075-4701. doi: 10.3390/met11122016. URL `https://www.mdpi.com/2075-4701/11/12/2016`.

[9] A. Moridi, S.M. Hassani-Gangaraj, S. Vezzú, L. Trško, and M. Guagliano. Fatigue behavior of cold spray coatings: The effect of conventional and severe shot peening as pre-/post-treatment. *Surface and Coatings Technology*, 283:247–254, 2015. ISSN 0257-8972. doi: https://doi.org/10.1016/j.surfcoat.2015.10.063. URL `https://www.sciencedirect.com/science/article/pii/S0257897215303583`.

[10] E. Sansoucy, P. Marcoux, L. Ajdelsztajn, and B. Jodoin. Properties of sic-reinforced aluminum alloy coatings produced by the cold gas dynamic spraying process. *Surface and Coatings Technology*, 202(16):3988–3996, 2008. ISSN 0257-8972. doi: https://doi.org/10.1016/j.surfcoat.2008.02.017.

[11] Xin Chu, Hanqing Che, Phuong Vo, Rohan Chakrabarty, Binhan Sun, Jun Song, and Stephen Yue. Understanding the cold spray deposition efficiencies of 316l/fe mixed powders by performing splat tests onto as-polished coatings. *Surface and Coatings Technology*, 324:353–360, 2017. ISSN 0257-8972. doi: https://doi.org/10.1016/j.surfcoat.2017.05.083.

[12] A. Sova, R. Maestracci, M. Jeandin, Ph. Bertrand, and I. Smurov. Kinetics of composite coating formation process in cold spray: Modelling and experimental validation. *Surface and Coatings Technology*, 318:309–314, May 2017. ISSN 02578972. doi: 10.1016/j.surfcoat.2016.06.084.

[13] Lapushkina and Alexey Sova. Effect of powder mixture composition on the deposition efficiency in cold spay: Modelling and experimental validation. *Coatings*, 9:832, 12 2019. doi: 10.3390/coatings9120832.

[14] Amir Ardeshiri Lordejani, Luca Vitali, Mario Guagliano, and Sara Bagherifard. Estimating deposition efficiency and chemical composition variation along thickness for cold spraying of composite feedstocks. *Surface and Coatings Technology*, 436:128239, April 2022. ISSN 02578972. doi: 10.1016/j.surfcoat.2022.128239.

[15] Shuo Yin, Xiaofang Wang, Bao-peng Xu, and Wenya li. Examination on the calculation method for modeling the multi-particle impact process in cold spraying. *Journal of Thermal Spray Technology*, 19:1032–1041, 09 2010. doi: 10.1007/s11666-010-9489-9.

[16] Jing Xie, Daniel Nélias, Hélène Walter-Le Berre, Kazuhiro Ogawa, and Yuji Ichikawa.

Simulation of the cold spray particle deposition process. *Journal of Tribology*, 137 (4):041101, 10 2015. ISSN 0742-4787. doi: 10.1115/1.4030257.

[17] Victor Kenneth Champagne, Ozan Cagatay Ozdemir, and Aaron Nardi, editors. *Practical Cold Spray*. Springer International Publishing, Cham, 2021. ISBN 978-3-030-70055-3 978-3-030-70056-0. doi: 10.1007/978-3-030-70056-0.

[18] Victor Kenneth Champagne, Dennis Helfritch, Christian Widener, Brian James, Chris Howe, Alex Krakovitz, and Tom Stamey. *Applications*, pages 381–441. Springer International Publishing, Cham, 2021. ISBN 978-3-030-70056-0. doi: 10.1007/978-3-030-70056-0_10.

[19] V.F. Kosarev, S.V. Klinkov, A.P. Alkhimov, and A.N. Papyrin. On Some Aspects of Gas Dynamics of the Cold Spray Process. *Journal of Thermal Spray Technology*, 12(2):265–281, June 2003. ISSN 00000000, 10599630. doi: 10.1361/105996303770348384.

[20] S. M. Hassani-Gangaraj, A. Moridi, and M. Guagliano. Critical review of corrosion protection by cold spray coatings. 31(11):803–815. ISSN 0267-0844, 1743-2944. doi: 10.1179/1743294415Y.0000000018.

[21] Mostafa Hassani, David Veysset, Yuchen Sun, Keith A. Nelson, and Christopher A. Schuh. Microparticle impact-bonding modes for mismatched metals: From co-deformation to splatting and penetration. 199:480–494. ISSN 13596454. doi: 10.1016/j.actamat.2020.08.038.

[22] Roghayeh Nikbakht, Hamid Assadi, Kamal Jahani, Mohammad Saadati, and Bertrand Jodoin. Cold spray deformation and deposition of blended feedstock powders not necessarily obey the rule of mixture. *Surface and Coatings Technology*, 424: 127644, October 2021. ISSN 02578972. doi: 10.1016/j.surfcoat.2021.127644.

[23] Aleksandra Nastic, Daniel MacDonald, and Bertrand Jodoin. The Influence of Feedstock Powder. In Sunil Pathak and Gobinda C. Saha, editors, *Cold Spray in the Realm of Additive Manufacturing*, pages 33–85. Springer International Publishing, Cham, 2020. ISBN 978-3-030-42755-9 978-3-030-42756-6. doi: 10.1007/978-3-030-42756-6_3. Series Title: Materials Forming, Machining and Tribology.

[24] Aaron Nardi, Danielle Cote, and Victor Kenneth Champagne. *Feedstock Powders*, pages 101–142. Springer International Publishing, Cham, 2021. ISBN 978-3-030-70056-0. doi: 10.1007/978-3-030-70056-0_4. URL `https://doi.org/10.1007/978-3-030-70056-0_4`.

[25] Spyros Kamnis, Sai Gu, and Michalis Vardavoulias. The influence of powder porosity on the bonding mechanism at the impact of thermally sprayed solid particles. 41(13): 3517–3524. ISSN 1073-5623, 1543-1940. doi: 10.1007/s11661-010-0488-8.

[26] Jingwei Wu, Hongyuan Fang, Sanghoon Yoon, HyungJun Kim, and Changhee Lee. The rebound phenomenon in kinetic spraying deposition. *Scripta Materialia*, 54(4): 665–669, 2006. ISSN 1359-6462. doi: https://doi.org/10.1016/j.scriptamat.2005.10.028. Viewpoint set no. 38 on: Frontiers on fabrication and properties of porous and cellular metallic materials.

[27] Matteo Terrone, Amir Ardeshiri Lordejani, Jan Kondas, and Sara Bagherifard. A numerical approach to design and develop freestanding porous structures through cold spray multi-material deposition. *Surface and Coatings Technology*, 421:127423, 2021. ISSN 0257-8972. doi: https://doi.org/10.1016/j.surfcoat.2021.127423.

[28] Wen-Ya Li, Hanlin Liao, Chang-Jiu Li, Gang Li, Christian Coddet, and Xiaofang Wang. On high velocity impact of micro-sized metallic particles in cold spraying. *Applied Surface Science*, 253(5):2852–2862, December 2006. doi: 10.1016/j.apsusc.2006.05.126.

[29] Wenya li, Chao ZHANG, Chang-Jiu Li, and Hanlin Liao. Modeling aspects of high velocity impact of particles in cold spraying by explicit finite element analysis. *Journal of Thermal Spray Technology*, 18:921–933, 05 2009. doi: 10.1007/s11666-009-9325-2.

[30] Wen-Ya Li, Hanlin Liao, Chang-Jiu Li, Hee-Seon Bang, and C. Coddet. Numerical simulation of deformation behavior of al particles impacting on al substrate and effect of surface oxide films on interfacial bonding in cold spraying. *Applied Surface Science*, 253(11):5084–5091, 2007. ISSN 0169-4332. doi: https://doi.org/10.1016/j.apsusc.2006.11.020.

[31] Oyinbo, Sunday Temitope and Jen, Tien-Chien. Feasibility of numerical simulation methods on the cold gas dynamic spray (cgds) deposition process for ductile materials. *Manufacturing Rev.*, 7:24, 2020. doi: 10.1051/mfreview/2020023.

[32] Abreeza Manap, O. Nooririnah, Halina Misran, T Okabe, and Kazuhiro Ogawa. Experimental and sph study of cold spray impact between similar and dissimilar metals. *Surface Engineering*, 30:335–341, 06 2014. doi: 10.1179/1743294413Y.0000000237.

[33] Baran Yildirim, Sinan Muftu, and Andrew Gouldstone. Modeling of high velocity impact of spherical particles. *Wear*, 270:703–713, 04 2011. doi: 10.1016/j.wear.2011.02.003.

[34] Shuo Yin, Xiaofang Wang, Bao-peng Xu, and Wenya li. Examination on the calculation method for modeling the multi-particle impact process in cold spraying. *Journal of Thermal Spray Technology*, 19:1032–1041, 09 2010. doi: 10.1007/s11666-010-9489-9.

[35] Peter C. King, Gyuyeol Bae, Saden H. Zahiri, Mahnaz Jahedi, and Changhee Lee. An Experimental and Finite Element Study of Cold Spray Copper Impact onto Two Aluminum Substrates. *Journal of Thermal Spray Technology*, 19(3):620–634, March 2010. ISSN 1544-1016. doi: 10.1007/s11666-009-9454-7. URL `https://doi.org/10.1007/s11666-009-9454-7`.

[36] Gyuyeol Bae, Yuming Xiong, S. Kumar, Kicheol Kang, and Changhee Lee. General aspects of interface bonding in kinetic sprayed coatings. *Acta Materialia*, 56(17):4858–4868, 2008. ISSN 1359-6454. doi: https://doi.org/10.1016/j.actamat.2008.06.003.

[37] T Hussain, D G McCartney, and P H Shipway. Bonding between aluminium and copper in cold spraying: Story of asymmetry. *Materials Science and Technology*, 28 (12):1371–1378, 2012. doi: 10.1179/1743284712Y.0000000051.

[38] Granta Design. Granta edupack 2021 r2. `https://www.ansys.com/it-it/products/materials/granta-edupack`, 2021. Version 21.2.0.

[39] Sara Bagherifard, Mauro Filippo Molla, Daniel Kajanek, Riccardo Donnini, Branislav Hadzima, and Mario Guagliano. Accelerated biodegradation and improved mechanical performance of pure iron through surface grain refinement. *Acta Biomaterialia*, 98:88–102, 2019. ISSN 1742-7061. doi: https://doi.org/10.1016/j.actbio.2019.05.033. 10th BIOMETAL2018 - International Symposium on Biodegradable Metals.

[40] Gordon R. Johnson and William H. Cook. Fracture characteristics of three metals subjected to various strains, strain rates, temperatures and pressures. *Engineering Fracture Mechanics*, 21(1):31–48, January 1985. ISSN 00137944. doi: 10.1016/0013-7944(85)90052-9.

[41] Vasu Kumar Reddy Sirigiri, Vinith Yadav Gudiga, Uday Shankar Gattu, G. Suneesh, and Krishna Mohan Buddaraju. A review on johnson cook material model. *Materials Today: Proceedings*, 62:3450–3456, 2022. ISSN 2214-7853. doi: https://doi.org/10.1016/j.matpr.2022.04.279. International Conference on Materials, Processing Characterization (13th ICMPC).

[42] S.P.F.C. Jaspers. *Metal cutting mechanics and material behaviour*. Phd thesis 1 (research tu/e / graduation tu/e), Mechanical Engineering, 1999.

A | MATLAB Codes

A.1. MATLAB Code for DE predictive model

Listing A.1: MATLAB Code for Bimetallic Coating Simulation and DE Calculation for a feedstock of 25% Al and 75% Fe on an aluminum substrate

```
clc
clear
close all

%% Height estimation
n=2 ; %Number of materials
%Remember n=1 is for Al and n=2 Fe

r=zeros(n,1);  %Particles undeformed radius [um]
r(1)=32.1/2;   %Aluminum underformed radius [um]
r(2)=31.53/2;   %Iron undeformed radius [um]
sr=zeros(n,1); %Splat radius for different particles[um]
sr(1)=20.674; %Splat radius Al on Al[um]
sr(2)=15.747; %Splat radius Fe on Fe [um]
f=zeros(n,1);  %Weight fraction
f(1)=0.25;  %Weight fraction Al
f(2)=1-f(1); % Weight fraction Fe
%These vectors need to be filled with the data obtained
   numerically and
%experimentally

h=zeros(n,1); %Height of a particle [um]
havg=0; %Average height of a layer[um]
Vavg=zeros(n,1); %Volume for every single particle [um^3]

for i=1:2
```

```
    Vavg(i)=4*pi()*r(i)^3/3;
    h(i)=Vavg(i)/(pi()*sr(i)^2);
    Vavg2(i)=4*2*r(i)^3/3;
    havg=havg+h(i)*f(i);
end

th=1000; %Total thickness
lay=ceil(th/havg); %Number of layers to model

Dat=zeros(lay,6); %Matrix that will include #layer, thickness,
   DEal, DEfe, %Al, %Fe

%% Parameters to be used for the whole coating
rho=[1.4E-12 3.65E-12]; % Densities in [g/um^3]

c=zeros(n,1); % Number of powder particles
c(1)=f(1)*rho(2)*Vavg(2)/(f(1)*rho(2)*Vavg(2)+f(2)*rho(1)*Vavg(1));
c(2)=1-c(1);

% **Splat radii organized by case (Rows) and particle size
   (Columns)**
% Rows: 1 = Impact on Aluminum, 2 = Impact on Iron, 3 = Impact on
   Substrate
% Columns: 1 = D10, 2 = D50, 3 = D90

sral = zeros(3,3); % Splat radius for Aluminum particles [um]
srfe = zeros(3,3); % Splat radius for Iron particles [um]

% Aluminum splat radii [um]
sral(1,:) = [12.590, 20.674, 36.229]; % Al on Al for D10, D50, D90
sral(2,:) = [14.504, 24.474, 43.706]; % Al on Fe for D10, D50, D90
sral(3,:) = [13.599, 23.151, 37.468]; % Al on Substrate for D10,
   D50, D90

% Iron splat radii [um]
srfe(1,:) = [10.167, 16.033, 24.035]; % Fe on Al for D10, D50, D90
srfe(2,:) = [11.950, 18.995, 28.254]; % Fe on Fe for D10, D50, D90
srfe(3,:) = [10.316, 16.378, 24.426]; % Fe on Substrate for D10,
   D50, D90
```

```
60
61 % **C lculo de  reas  de splat (Matrices 3x3)**
62 A_sral = pi() * sral.^2; % Splat area for Aluminum [um^2]
63 A_srfe = pi() * srfe.^2; % Splat area for Iron [um^2]
64
65 % Relative splat areas (Matrices 3x3)
66 for i=1:3
67     SA_alonal(i)=A_sral(1,i)/(A_sral(1,i)+A_srfe(1,i)); %Relative
       splat area of Aluminum on Aluminum
68     SA_feonal(i)=A_srfe(1,i)/(A_sral(1,i)+A_srfe(1,i)); %Relative
       splat area of Iron on Aluminum
69     SA_feonfe(i)=A_srfe(2,i)/(A_sral(2,i)+A_srfe(2,i)); %Relative
       splat area of Aluminum on Iron
70     SA_alonfe(i)=A_sral(2,i)/(A_sral(2,i)+A_srfe(2,i)); %Relative
       splat area of Iron on Iron
71     SA_alons(i)=A_sral(3,i)/(A_sral(3,i)+A_srfe(3,i)); %Relative
       splat area of Aluminum on Iron THIS ONE CHANGES FROM IRON
       TO ALUMINUM SUBSTRATE
72     SA_feons(i)=A_srfe(3,i)/(A_sral(3,i)+A_srfe(3,i)); %Relative
       splat area of Iron on Iron THIS ONE CHANGES FROM IRON TO
       ALUMINUM SUBSTRATE
73 end
74 %SA_alonal=[0.3 0.45 0.49]; %Testing values
75 %SA_feonal=1.-SA_alonal;
76 %Probabilities of getting a D10,D50 and D90 of Aluminum and Iron
77
78 pd10Al=0.1829;  %Probability of having a D10 size Al particle
79 pd50Al=0.6202;  %Probability of having a D50 size Al particle
80 pd90Al=0.1969;  %Probability of having a D90 size Al particle
81
82
83
84 pd10Fe=0.2385;  %Probability of having a D10 size Fe particle
85 pd50Fe=0.5727;  %Probability of having a D50 size Fe particle
86 pd90Fe=0.1888;  %Probability of having a D90 size Fe particle
87
88
89 % Adhesion probabilities
90 p=zeros(6,1);
```

```
91
92  p(1)=0.5422;  % Probability of adhesion of Aluminum on Aluminum
93  p(2)=0.2812;  % Probability of adhesion of Aluminum on Iron
94  p(3)=0.5225;  % Probability of adhesion of Aluminum on coating
       surface
95  p(4)=0.5723;  % Probability of adhesion of Iron on Aluminum
96  p(5)=0.4254;  % Probability of adhesion of Iron on Iron
97  p(6)=0.4628;  % Probability of adhesion of Iron on coating surface
98
99  datos=[0 0 0];
100 datos2=[0 0 0];
101 %% First layer calculation
102
103 x=randsrc(1,1,[1,2,3; pd10Al, pd50Al, pd90Al]);
104 y=randsrc(1,1,[1,2,3; pd10Fe, pd50Fe, pd90Fe]);
105
106 datos(x)=datos(x)+1;
107 datos2(y)=datos2(y)+1;
108 s_al=(p(3)*c(1)*SA_alons(x))/(p(3)*c(1)*SA_alons(x)+p(6)*c(2)*SA_feons(y));
       %Relative area, percentage of area covered by Al THIS ONE
       CHANGES FROM IRON TO ALUMINUM SUBSTRATE
109 s_fe=1-s_al; %Relative area, percentage of area covered by Fe
       THIS ONE CHANGES FROM IRON TO ALUMINUM SUBSTRATE
110
111 DE_al=p(3); %Deposition efficiency of Aluminum
112 DE_fe=p(6); %Deposition efficiency of Iron
113
114 Dat(1,1)=1;       %Layer number
115 Dat(1,2)=0; %Height or thickness [mm]
116 Dat(1,3)=DE_al;  %Deposition efficiency of Aluminum
117 Dat(1,4)=DE_fe;  %Deposition efficiency of Iron
118 Dat(1,5)=s_al;   %Relative area of Aluminum
119 Dat(1,6)=s_fe;   %Relative area of Iron
120
121 %% N layer calculations
122
123 it=50;  %Maximum number of iterations still to be determined
124
125 for i=2:lay
```

```
126     RLA_al=zeros(it,1);           %Remaining layer area of Aluminum
127     RLA_fe=zeros(it,1);           %Remaining layer area of Iron
128
129     LA_alonal=zeros(it,1);        %Layer area of Aluminum on
            Aluminum
130     LA_alonfe=zeros(it,1);        %Layer area of Aluminum on Iron
131     LA_feonal=zeros(it,1);        %Layer area of Iron on Aluminum
132     LA_feonfe=zeros(it,1);        %Layer area of Iron on Iron
133     ILA_al=zeros(it,1);           %Ideal layer area of Aluminum
134     ILA_fe=zeros(it,1);           %Ideal layer area of Iron
135
136     %RLA's calculation first iterarion
137     x=randsrc(1,1,[1,2,3; pd10Al, pd50Al, pd90Al]);
138     y=randsrc(1,1,[1,2,3; pd10Fe, pd50Fe, pd90Fe]);
139     datos(x)=datos(x)+1;
140     datos2(y)=datos2(y)+1;
141
142     RLA_al(1)=Dat(i-1,5);
143     RLA_fe(1)=Dat(i-1,6);
144     %LA's calculation first iteration
145     LA_alonal(1)=c(1)*p(1)*RLA_al(1)*SA_alonal(x);
146     LA_alonfe(1)=c(1)*p(2)*RLA_fe(1)*SA_alonfe(x);
147     LA_feonal(1)=c(2)*p(4)*RLA_al(1)*SA_feonal(y);
148     LA_feonfe(1)=c(2)*p(5)*RLA_fe(1)*SA_feonfe(y);
149     %ILA's calculation first iterarion
150     ILA_al(1)=c(1)*(RLA_al(1)*SA_alonal(x)+RLA_fe(1)*SA_alonfe(x));
151     ILA_fe(1)=c(2)*(RLA_al(1)*SA_feonal(y)+RLA_fe(1)*SA_feonfe(y));
152
153     for j=2:it
154         x=randsrc(1,1,[1,2,3; pd10Al, pd50Al, pd90Al]);
155         y=randsrc(1,1,[1,2,3; pd10Fe, pd50Fe, pd90Fe]);
156         datos(x)=datos(x)+1;
157         datos2(y)=datos2(y)+1;
158         itera=j;
159
160         RLA_al(j)=RLA_al(1)- LA_alonal(j-1)-LA_feonal(j-1);
161         RLA_fe(j)=RLA_fe(1)- LA_alonfe(j-1)-LA_feonfe(j-1);
162
163     % **Break Condition: Exit loop if RLA values are too small**
```

```
164         if RLA_al(j) < 0 || RLA_fe(j) < 0
165          itera=j-1;
166          break;
167         end
168
169
170          LA_alonal(j)=
                LA_alonal(j-1)+c(1)*p(1)*RLA_al(j)*SA_alonal(x);
171          LA_alonfe(j)=LA_alonfe(j-1)+c(1)*p(2)*RLA_fe(j)*SA_alonfe(x);
172          LA_feonal(j)=LA_feonal(j-1)+c(2)*p(4)*RLA_al(j)*SA_feonal(y);
173          LA_feonfe(j)=LA_feonfe(j-1)+c(2)*p(5)*RLA_fe(j)*SA_feonfe(y);
174          ILA_al(j)=ILA_al(j-1)+(c(1)...
175          *(RLA_al(j)*SA_alonal(x)+RLA_fe(j)*SA_alonfe(x)));
176          ILA_fe(j)=ILA_fe(j-1)+(c(2)...
177          *(RLA_al(j)*SA_feonal(y)+RLA_fe(j)*SA_feonfe(y)));
178
179
180      end
181
182
183      itera;
184      Dat(i,1)=i;
185      Dat(i,2)=havg*(i-1);
186      Dat(i,3)=(LA_alonal(itera)+LA_alonfe(itera))/ILA_al(itera);
187      Dat(i,4)=(LA_feonal(itera)+LA_feonfe(itera))/ILA_fe(itera);
188      Dat(i,5)=LA_alonal(itera)+LA_alonfe(itera);
189      Dat(i,6)=LA_feonal(itera)+LA_feonfe(itera);
190
191  end
192
193  suma1=sum(datos);
194  suma2=sum(datos2);
195  datos=datos*100/suma1;
196  datos2=datos2*100/suma2;
197
198  %% Define experimental data for 25% Al and 75% Fe powder mixture
199  % Experimental data provided by the user
200  experimental_data = [
201      15, 30.65, 69.35;  % Height, %Fe, %Al for the first section
```

```
    45, 45.97, 54.03;
    75, 48.77, 51.23;
    120, 48.78, 51.22;
    200, 51.15, 48.85;
    375, 50.11, 49.89;
    625, 41.57, 58.43;
    875, 42.77, 57.23;

];

% Extract columns of experimental data
height_exp = experimental_data(:,1);  % Height
Fe_exp = experimental_data(:,2);      % %Fe composition
Al_exp = experimental_data(:,3);      % %Al composition
std_Al_exp = [6.91, 4.07, 2.79, 4.90, 2.49, 4.08, 4.05, 2.97];  % Standard deviation for Al
std_Fe_exp = [6.91, 4.07, 2.79, 4.90, 2.49, 4.08, 4.05, 2.97];  % Standard deviation for Fe

%% Include in the original code for simulation

% Input data, particle parameters, etc., as in the original code

% (Here go the calculations and functions from your original code)

% For the final plot:
coating_thickness = Dat(:,2);  % Use the thickness values from the Dat variable
Al_NDEP = Dat(:,5) * 100;      % Aluminum composition (simulated)
Fe_NDEP = Dat(:,6) * 100;      % Iron composition (simulated)

% Nominal composition
Al_nominal = f(1)*100;
Fe_nominal = f(2)*100;

% Create the plot
figure;
hold on;
```

```
237 plot(coating_thickness, Al_NDEP, '-', 'Color', [0.85 0.33 0.10],
    'LineWidth', 2);  % Aluminum (NDEP)
238 plot(coating_thickness, Fe_NDEP, '-', 'Color', [0.93 0.69 0.13],
    'LineWidth', 2);  % Iron (NDEP)
239
240 % Add nominal composition lines
241 plot([0 max(coating_thickness)], [Al_nominal Al_nominal], '--',
    'Color', [0.85 0.33 0.10], 'LineWidth', 1.5); % Aluminum
    nominal
242 plot([0 max(coating_thickness)], [Fe_nominal Fe_nominal], '--',
    'Color', [0.93 0.69 0.13], 'LineWidth', 1.5); % Iron nominal
243
244 % Add experimental data with error bars
245 errorbar(height_exp, Al_exp, std_Al_exp, 'o', 'Color', [0.85 0.23
    0.10], 'MarkerFaceColor', [0.85 0.23 0.10], 'LineWidth', 1.5);
     % Experimental Aluminum
246 errorbar(height_exp, Fe_exp, std_Fe_exp, 'o', 'Color', [0.93 0.59
    0.13], 'MarkerFaceColor', [0.93 0.59 0.13], 'LineWidth', 1.5);
     % Experimental Iron
247
248 % plot(height_exp, Al_exp, '-.', 'Color', [0.95 0.23 0.10],
    'LineWidth', 1);  % Aluminum (Experimental)
249 % plot(height_exp, Fe_exp, '-.', 'Color', [0.83 0.59 0.13],
    'LineWidth', 1);  % Fe (Experimental)
250 %
251
252 % Labels and legend
253 xlabel('Coating Thickness [ m ]', 'FontSize', 12);
254 ylabel('Coating composition [%]', 'FontSize', 12);
255 ylim([0 100]);
256 legend({'Aluminum (DE model)', 'Iron (DE model)', 'Aluminum
    (nominal)', 'Iron (nominal)', ...
257     'Aluminum (experimental)', 'Iron (experimental)'},
        'Location', 'SouthOutside');
258
259 grid on;
260 hold off;
```

A.2. MATLAB Code for calulating the adhesion probabilities

Listing A.2: MATLAB Code for Adhesion Probability for aluminum powders

```
clc;
clear all;
close all;

syms x

V=49.48*6 ;     %Flow rate [mm^3/s]
d=7.5;          %Nozzle diameter[mm]
A=pi()*d^2/4; %Nozzle cross section [mm^2]
r=d/2;          %Nozzle radius [mm]
vt=500;         %Transverse speed [mm/s]
vt2=250;        %Transverse speed [mm/s]
L1=40;          %Aluminum substrate length [mm]
L2=20;          %Iron substrate length [mm]
% Define the first function to integrate
expr1 = (V/A) * x * ( (r^2 * acos((r - vt*x)/r)) - (r * (r - vt*x) *
    cos(asin((r - vt*x)/r))) );

% Define the second function to integrate (modified version)
expr2 = (V/A) * x * ( (r^2 * acos((r - vt2*x)/r))  - (r * (r - vt2*x) *
    cos(asin((r - vt2*x)/r))) );

% Define the integration limits
a1 = 0;
b1 = d/(vt);
a2=0;
b2=d/(vt2);

% Compute the first definite integral symbolically
integral_result_sym1 = int(expr1, x, a1, b1);

% Compute the second definite integral symbolically
integral_result_sym2 = int(expr2, x, a2, b2);

% Evaluate the integrals numerically
integral_result1 = double(integral_result_sym1); % Convert to a
    numerical value
integral_result2 = double(integral_result_sym2); % Convert to a
    numerical value
```

```
36
37 % Volume and mass calculations for the first integral
38 v1 = ((L1 - d) / vt) * V; % Volume for the long section Al substrate
       [mm^3]
39 v12= ((L1 - d) / vt2) * V; % Volume for the long section Al substrate
       [mm^3] at 250 [mm/s]
40 v2 =  integral_result1;        % Volume while entering the substrate
       [mm^3]
41 v22= integral_result_sym2;      % Volume while entering the substrate
       [mm^3] at 250 [mm/s]
42 v3 = ((L2 - d) / vt) * V; % Volume for the long section Fe substrate
       [mm^3]
43 vtot1 = 2 * v2 + v1;              % Volume for a single stripe Al
       substrate [mm^3]
44 vtot12= 2*v22+v12;                % Volume for a single stripe Al
       substrate [mm^3] at 250 [mm/s]
45 vtot2 = 2 * v2 + v3;              % Volume for a single stripe Fe
       substrate [mm^3]
46 mtot1 = vtot1 * 6 * 0.0014;       % Total deposited mass for 6 stripes
       on Al substrate [g]
47 mtot3 = vtot2 * 6 * 0.0014;       % Total deposited mass for 6 stripes
       on Fe substrate [g]
48 mtot12=vtot12*100*0.0014;          % Total deposited mass for 50
       stripes on Al substrate [g]
49
50
51 % Adhesion probability calculations
52 p6 = 0.174/ mtot1 * 100;  %OK
53 p3 = 0.0849 / mtot1 * 100;  %OK
54 p4 = 0.01764 / mtot3 * 100;  %OK
55 p1 =0.0881/mtot1 * 100;      %OK
56
57 % Display results with proper formatting
58 %fprintf('Theoretical deposited mass for 6 passes  in g: %.6f\n',
       mtot1);
59 fprintf('Adhesion prob. of Al on Fe powder #6 : %.2f%%\n', p6);
60 fprintf('Adhesion prob. of Al on Al substrate #3 : %.2f%%\n', p3);
61 fprintf('Adhesion prob. of Al on Fe substrate #4: %.2f%%\n', p4);
62 fprintf('Adhesion prob. of Al on Al powder #1: %.2f%%\n', p1);
```

Acknowledgements

I would like to express my sincere gratitude to my thesis supervisor, Prof. Sara Bagherifard, and to my co-supervisor, Dr. Asghar Heydari Astaraee, for their invaluable guidance and expertise throughout this process. I would especially like to thank my co-supervisor, Kiran Tulasagiri Raddi, for his time, dedication, wisdom, and unwavering support from the beginning of this project. Without his collaboration, this thesis would not have been possible.

I would also like to thank Ing. Ludovica Rovatti for his continuous support and invaluable knowledge during the tests conducted in various laboratories.

I would also like to thank my friends, who have accompanied me through different stages of my life, offering their support and advice. In particular, I appreciate a colleague who accompanied me throughout much of this process.

Finally, I would like to express my deepest gratitude to my family, especially to my mother, Paula Zepeda, and my father, Francisco Abate. They have always believed in me, encouraging me to face challenges and to work diligently to overcome them. Their support, companionship, and advice throughout my life have been fundamental in achieving this goal.

This thesis work received funding from the European Research Council (ERC) under the European Union's Horizon 2021 research and innovation programme (ArcHIDep ERC-Co project, grant agreement n. 101044228).



Agradecimientos

Quisiera expresar mi más sincero agradecimiento a mi supervisora de tesis, la Prof. Sara Bagherifard, y a mi co-supervisor, el Dr. Asghar Heydari Astaraee, por su valiosa orientación y conocimientos durante todo este proceso. Agradezco especialmente a mi co-supervisor, Kiran Tulasagiri Raddi, por su tiempo, dedicación, sabiduría y apoyo incondicional desde el inicio de este proyecto. Sin su colaboración, esta tesis no habría sido posible.

También me gustaría agradecer a la Ing. Ludovica Rovatti por su constante apoyo y su invaluable conocimiento a lo largo de las pruebas realizadas en los diferentes laboratorios.

También me gustaría agradecer a mis amigos, quienes me han acompañado en las distintas etapas de mi vida, brindándome su apoyo y consejos. De manera particular, agradezco a una compañera que me acompañó durante gran parte de este proceso.

Finalmente, quiero expresar mi más profundo agradecimiento a mi familia, en especial a mi madre, Paula Zepeda, y a mi padre, Francisco Abate. Ellos siempre han creído en mí, impulsándome a enfrentar los desafíos trabajar duro para cumplirlos. Su apoyo, compañía y consejos a lo largo de toda mi vida han sido fundamentales para alcanzar este objetivo.